

# Towards A Generalizable Pathology Foundation Model via Unified Knowledge Distillation

Jiabo Ma<sup>1†</sup>, Zhengrui Guo<sup>1†</sup>, Fengtao Zhou<sup>1</sup>, Yihui Wang<sup>1</sup>, Yingxue Xu<sup>1</sup>,  
 Yu Cai<sup>2</sup>, Zhengjie Zhu<sup>3</sup>, Cheng Jin<sup>1</sup>, Yi Lin<sup>1</sup>, Xinrui Jiang<sup>1</sup>, Anjia Han<sup>4</sup>,  
 Li Liang<sup>5,6,7</sup>, Ronald Cheong Kin Chan<sup>8</sup>, Jiguang Wang<sup>9,10</sup>,  
 Kwang-Ting Cheng<sup>1,2</sup>, Hao Chen<sup>1,9,10\*</sup>

<sup>1</sup>Department of Computer Science and Engineering, The Hong Kong University of Science and Technology, Hong Kong SAR, China.

<sup>2</sup>Department of Electronic and Computer Engineering, The Hong Kong University of Science and Technology, Hong Kong SAR, China.

<sup>3</sup>Information Hub, The Hong Kong University of Science and Technology (Guangzhou), Guangzhou, China.

<sup>4</sup>Department of Pathology, The First Affiliated Hospital, Sun Yat-sen University, Guangzhou, China.

<sup>5</sup>Department of Pathology, Nanfang Hospital and School of Basic Medical Sciences, Southern Medical University, Guangzhou, China.

<sup>6</sup>Guangdong Provincial Key Laboratory of Molecular Tumor Pathology, Guangzhou, China.  
<sup>7</sup>Jinfeng Laboratory, Chongqing, China.

<sup>8</sup>Department of Anatomical and Cellular Pathology, The Chinese University of Hong Kong, Hong Kong SAR, China.

<sup>9</sup>Department of Chemical and Biological Engineering, The Hong Kong University of Science and Technology, Hong Kong SAR, China.

<sup>10</sup>Division of Life Science, The Hong Kong University of Science and Technology, Hong Kong SAR, China.

\*Corresponding author(s). E-mail(s): [jhc@cse.ust.hk](mailto:jhc@cse.ust.hk);

Contributing authors: [jmabq@connect.ust.hk](mailto:jmabq@connect.ust.hk); [zguobc@connect.ust.hk](mailto:zguobc@connect.ust.hk);  
[fzhouaf@connect.ust.hk](mailto:fzhouaf@connect.ust.hk); [ywangrm@connect.ust.hk](mailto:ywangrm@connect.ust.hk); [yxueb@connect.ust.hk](mailto:yxueb@connect.ust.hk);  
[yu.cai@connect.ust.hk](mailto:yu.cai@connect.ust.hk); [zzhuar@connect.ust.hk](mailto:zzhuar@connect.ust.hk); [cheng.jin@connect.ust.hk](mailto:cheng.jin@connect.ust.hk);  
[yi.lin@connect.ust.hk](mailto:yi.lin@connect.ust.hk); [csexrjiang@ust.hk](mailto:csexrjiang@ust.hk); [hananjia@mail.sysu.edu.cn](mailto:hananjia@mail.sysu.edu.cn); [lli@smu.edu.cn](mailto:lli@smu.edu.cn);  
[ronaldekchan@cuhk.edu.hk](mailto:ronaldekchan@cuhk.edu.hk); [jgwang@ust.hk](mailto:jgwang@ust.hk); [timcheng@ust.hk](mailto:timcheng@ust.hk);

†These authors contributed equally to this work.

## Abstract

Foundation models pretrained on large-scale datasets are revolutionizing the field of computational pathology (CPath). The generalization ability of foundation models is crucial for the success in various downstream clinical tasks. However, current foundation models have only been evaluated on a limited type and number of tasks, leaving their generalization ability and overall performance unclear. To address this gap, we established a most comprehensive benchmark to evaluate the performance of off-the-shelf foundation models across six distinct clinical task types, encompassing a total of 39 specific tasks. Our findings reveal that existing foundation models excel at certain task types but struggle to effectively handle the full breadth of clinical tasks. To improve the generalization of pathology foundation models, we propose a unified knowledge distillation framework consisting of both expert and self-knowledge distillation, where the former allows the model to learn from the knowledge of multiple expert models, while the latter leverages self-distillation to enable image representation learning via local-global alignment. Based on this framework, a Generalizable Pathology Foundation Model (GPFM) is pretrained on a large-scale dataset consisting of 190 million images from around 86,000 public H&E whole slides across 34 major tissue types. Evaluated on the established benchmark, GPFM achieves an impressive average rank of 1.36, with 29 tasks ranked 1st, while the second-best model, UNI, attains an average rank of 2.96, with only 4 tasks ranked 1st. The superior generalization of GPFM demonstrates its exceptional modeling capabilities across a wide range of clinical tasks, positioning it as a new cornerstone for feature representation in CPath.

**Keywords:** Computational Pathology, Foundation Model, Self-supervised Learning, Knowledge Distillation

## 1 Introduction

Pathology plays a crucial and evolving role in modern medicine, providing essential insights for the diagnosis, treatment, and prognosis of diseases [1–7]. In recent decades, the shift to digital pathology, particularly through whole slide imaging, has modernized the workflow of clinicians and improved access to slide data [8]. This has paved the way for CPath, an emerging field that leverages digital whole slide images (WSIs) and computational methods for clinical decision-making [9–11]. Specifically, CPath introduces advanced capabilities such as gene mutation prediction [12–14], direct prognosis [15–17], and treatment response assessment [18–20] directly from WSIs, demonstrating profound clinical significance. However, the diversity of clinical pathology tasks, combined with the limited data and annotations, poses significant challenges when training robust models for each individual task from scratch. This process is not only time-consuming but also impractical in real-world scenarios [11]. Consequently, the CPath community is actively seeking solutions that can effectively address this diverse range of tasks simultaneously [21–27].

In recent years, there has been a notable progress in the fields of computer vision and natural language processing driven by self-supervised

learning on large-scale datasets. These pretrained models, commonly referred to as foundation models, have garnered significant attention and have exhibited remarkable success across various tasks [28–30]. In the field of CPath, some efforts [31–37] have been dedicated to pretraining foundation models that can learn inherent representations of histopathology images, catering to the diverse array of tasks encountered in clinical pathology practice. However, the current foundation models have only been evaluated on a limited type of tasks as shown in **Figure 2.a**, leaving their overall performance unclear. To comprehensively evaluate these models, we built a most comprehensive benchmark spanning six major clinical task categories, comprising 39 specific tasks. Our findings revealed that the generalization ability of these models is still limited and no single model can effectively address all the tasks as shown in **Figure 1.c**. It can be seen that UNI [33] achieves the best performance in image retrieval and patch-level (ROI) tissue classification tasks, Phikon [32] performs best in survival analysis and report generation tasks, and CONCH [35] obtains highest performance in WSI classification and visual question answering (VQA) tasks. This can be attributed to the fact that each foundation model is trained using distinct datasets and

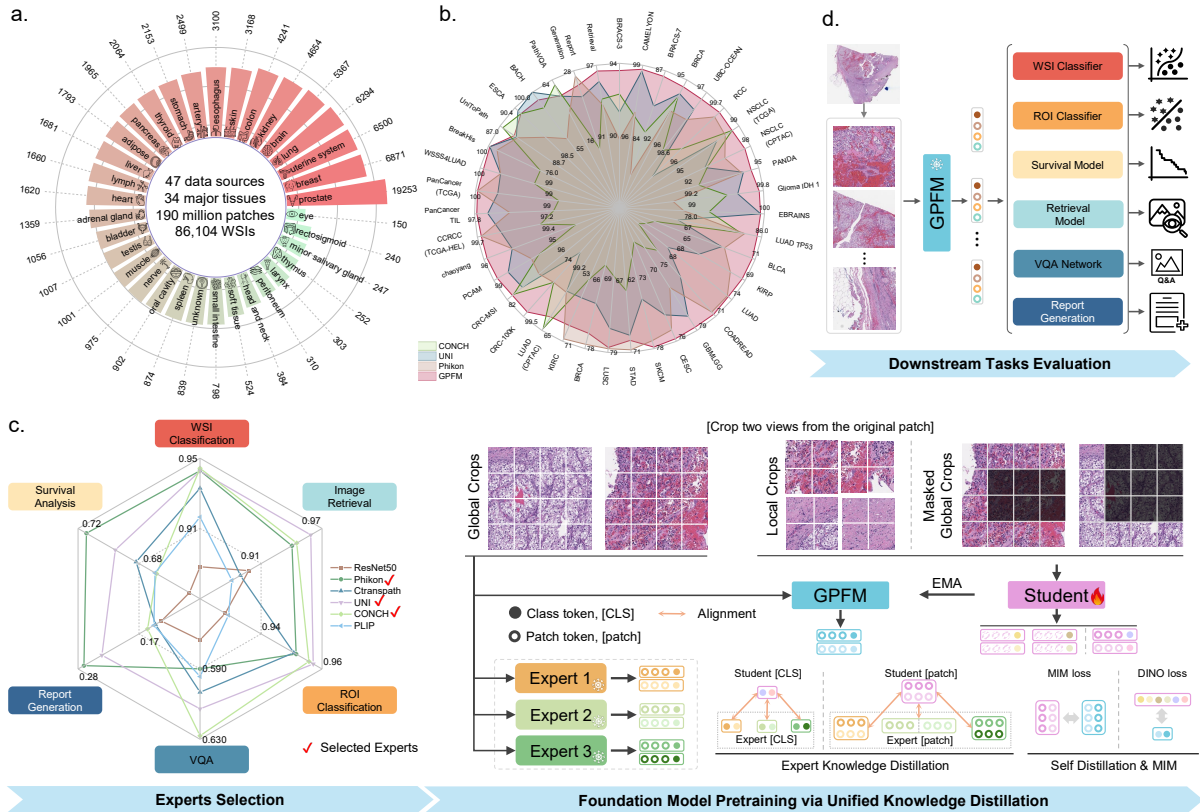


**Fig. 1 Overview of the GPFM.** GPFM is a state-of-the-art pretrained foundation model that demonstrates exceptional performance across 39 diverse clinical tasks. **a.** The GPFM dataset comprises a large-scale collection of 86,104 slides spanning 34 major tissue types, enabling comprehensive model training and evaluation. **b.** Overall performance of different foundation models across 39 tasks. GPFM outperforms other leading foundation models, achieving the best average rank of 1.36 (the first place in 29 out of the 39 tasks). **c.** The overview of unified knowledge distillation for GPFM. The experts used for Expert Knowledge Distillation will be selected based on their average performance on six different clinical tasks. The pretraining algorithm includes three key components: 1) Mask Image Modeling (MIM), 2) Self-Distillation, and 3) Expert Knowledge Distillation. The parameters of GPFM are updated through Exponential Moving Average (EMA). **d.** The versatility of GPFM is showcased through its application to a wide range of downstream clinical tasks, including whole-slide image classification, patch-level tissue classification, survival analysis, pathological tissue retrieval, visual question answering, and pathology report generation.

pretraining strategies, leading to specific advantages for each model within particular datasets. These findings highlight the need for further research to develop more generalizable foundation models that can consistently perform well across the diverse type of clinical tasks encountered in CPath. By addressing this challenge, we can unlock the full potential of the foundation model in CPath.

To improve the generalization of pathology foundation model and enhance the overall performance, an intuitive idea is to leverage the specific strengths of existing models by employing

knowledge distillation techniques [38, 39]. Accordingly, we proposed a novel self-supervised learning framework with expert and self knowledge distillation to develop a Generalizable Pathology Foundation Model (GPFM). Based on this pretraining method, we trained GPFM using a diverse dataset of approximately 190 million images from 86,104 public WSIs across 34 major tissue types. The overview of GPFM is presented in **Figure 1**. With the collected diverse tissues and the indirectly using of the images that used to pretrain expert models (e.g., UNI and CONCH), GPFM exhibits outstanding performance across the established benchmarks, achieving an average rank of 1.36 (29

out of 39 tasks), while the second-best performing model, UNI, achieving an average rank of 2.96 (4 out of 39 tasks). These results demonstrate the efficacy of GPFM as a generalizable foundation model in CPath, showcasing its potential to significantly advance the field. The ability of GPFM to consistently perform well across a diverse type of clinical tasks highlights the benefits of leveraging knowledge distillation to combine the strengths of expert models, ultimately leading to more robust and versatile foundation models for supporting clinicians and improving patient care.

## 2 Results

We evaluated various foundation models across 39 tasks, encompassing WSI classification (12 tasks), survival analysis (12 tasks), patch-level (ROI) tissue classification (12 tasks), pathological visual question answering, report generation, and pathological image retrieval. The overall results are presented in **Figure 2**. Since the tasks involved different types of evaluation metrics, we assessed the overall performance of the foundation models using an average ranking approach and reported the critical difference (CD) diagram [40–42]. The model with the best performance was ranked 1st, while the model with the lowest performance was ranked 7th. Across all tasks, the GPFM model achieved the top average rank score of 1.36 (best performance 29 out of 39), outperforming the second-best model, UNI, which had a ranking score of 2.96 (best performance 4 out of 39). Furthermore, we conducted the Nemenyi statistical test [40] to assess whether the ranking score of GPFM was significantly different from the other foundation models, as shown in **Figure 2.c**. The results indicate that GPFM had a statistically significant CD compared to the other six models, while UNI, Phikon, CONCH, and Ctranspath did not show a significant CD.

In addition, we also simply averaged the evaluation metrics across all 39 tasks, as shown in **Figure 2.b**. The GPFM model achieved an average score of 0.859, while the second-best performing model, Phikon, achieved an average score of 0.849. To further assess the significance of the performance difference, we conducted the Wilcoxon signed-rank test [40] between GPFM and the other foundation models. The results indicate that all  $p$ -values were less than 0.001, suggesting

that GPFM consistently and significantly outperformed the existing foundation models. It is worth noting that the second-best performing model is different depending on the evaluation perspective. From the ranking standpoint, as discussed earlier, the UNI model was the second-best performer with an average ranking score of 2.96. Considering both the ranking perspective and the average metric aspect, the results clearly indicate that GPFM achieves state-of-the-art performance and is much more generalizable compared to the other foundation models. The detailed results can be found in **Extended Data Table A1**.

### 2.1 WSI Classification

WSI classification is pivotal in accurate cancer diagnosis. It aids in categorizing the specific subtype of cancer, which can be significantly improved by utilizing foundation models. Therefore, it is important to evaluate the representation learning capabilities of different foundation models. In this study, we employed ABMIL [43] to assess the WSI classification performance as previous work [33]. We conducted experiments on a total of 12 tasks and the detailed experimental results are presented in **Extended Data Table A2-Table A14**.

Across 12 WSI classification tasks, GPFM achieved an average ranking score of 1.08, outperforming the second-best performing model, UNI, which achieved an average ranking score of 3.04. It’s worth noting that the ranking is based on the Area Under the Curve (AUC) metric, where a higher AUC indicates better performance. The detailed ranking scores of WSI classification tasks are presented in **Figure 2.d**. Furthermore, we evaluated the overall performance using average metrics, including AUC, balanced accuracy, and weighted F1 score. As shown in **Figure 3.a**, GPFM achieved the best average AUC of 0.956, representing a 1.4% improvement over the second-best performing model, CONCH, with statistical significance  $P < 0.001$  (+1.4%, CONCH,  $P < 0.001$ ). Similarly, as depicted in **Figure 3.b-c**, GPFM achieved the best balanced accuracy of 0.833 (+1.9%, UNI,  $P < 0.001$ ) and the best weighted F1 score of 0.834 (+1.9%, UNI,  $P < 0.001$ ). The detailed performance of the different foundation models is presented in **Figure 3.e-1** and **Extended Data Figure**

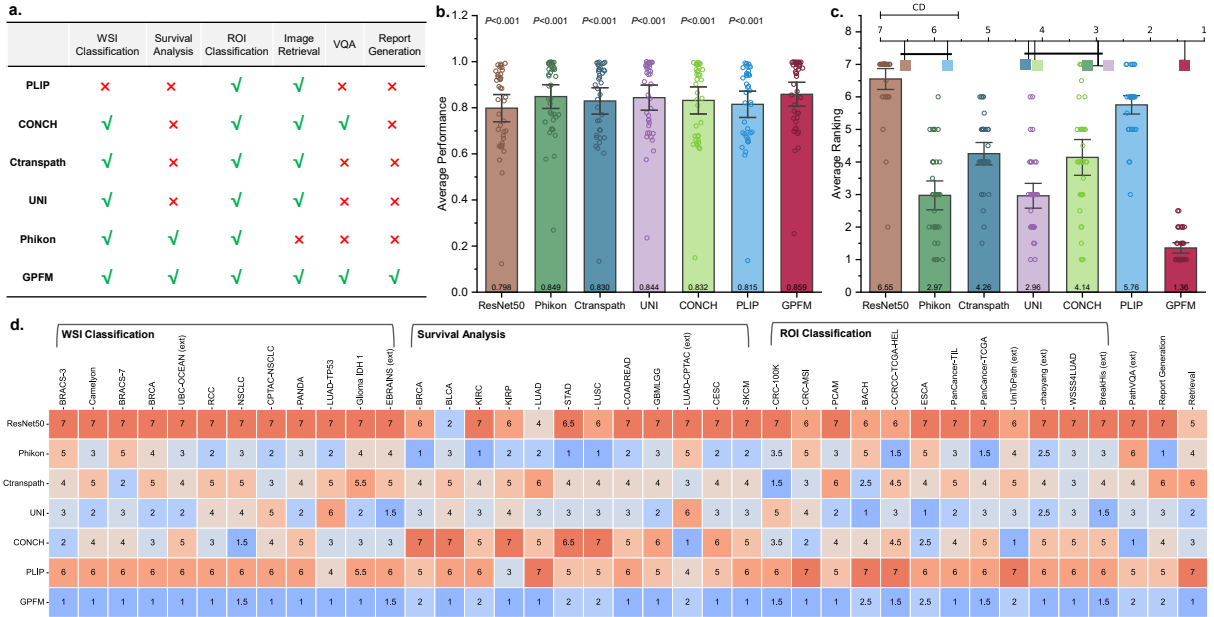


**Fig. 2 Comprehensive Comparison of Foundation Models across 39 Diverse Tasks.** **a.** Tasks evaluated by different foundation models. **b.** Average performance of foundation models across 39 tasks: WSI classification and tissue classification tasks are measured by AUC; survival analysis tasks are measured by C-index; the VQA task is measured by overall accuracy; the report generation task is measured by the average metric of BLUE, METEOR, and ROUGE-L; the image retrieval task is measured by average accuracy. The Wilcoxon signed-ranks test is employed to detect significant differences between off-the-shelf foundation models and the proposed GPFM. The figure demonstrates that GPFM achieved the highest average performance. **c.** Average rank of foundation models across 39 downstream tasks. The Nemenyi test is utilized to assess the critical differences (CD) in the ranking score of various foundation models. In the CD figure, there are no significant differences between the models covered by the black line. **d.** Overall ranking order of foundation models across 39 tasks. ext indicates external validation. If a model achieves the best performance, its rank value is set to 1. If two models have the same metric value, indicating a tie, the average rank value is assigned to all the tied models. For example, if two models tie for first place, their rank values would both be 1.5. This is calculated as the average of the ranks they would have received if there was no tie (1 for the first place model, and 2 for the second place model), resulting in an average of 1.5 for both models. The metrics employed for obtaining the ranking score are the same as in subfigure **b**.

**A1.a-d.** We also visualized the ROC curves of GPFM in **Extended Data Figure A2** for every classification task. These results across multiple performance metrics clearly illustrated the great potential and strong generalization ability of the GPFM model in the WSI classification tasks.

**GPFM improves cancer diagnosis.** Cancer diagnosis using WSIs is very common in CPath. Among 10 diagnosis tasks, GPFM achieved the best performance in 8 tasks including breast cancer (BRACS-3 [44], BRACS-7 [44], and BRCA [45], CAMELYON [46, 47]), lung cancer (CPTAC-NSCLC [45]), renal cell carcinoma (RCC [45]), prostate cancer (PANDA [48]), and ovarian cancer (UBC-OCEAN, an external dataset [49]). On the fine-grained brain tumor classification task (EBRAINS, an external dataset [50]), GPFM and

UNI tied for first place, while on the lung cancer subtyping based on NSCLC dataset [45], GPFM and CONCH tied for first place. The results illustrate that GPFM consistently performs best and is more robust than other foundation models in cancer diagnosis tasks.

**GPFM advances gene mutation prediction.** Following the same evaluation strategy as cancer diagnosis, we also investigated the potential of foundation models in 2 gene mutation prediction tasks. The GPFM achieved the best performance both in LUAD-TP53 (from TCGA) and Glioma IDH 1 (from TCGA GBMLGG) tasks, with AUCs of 0.855 and 0.998, respectively. Compared to the second-best model, Phikon, the GPFM showed a 1.2% improvement in AUC. These

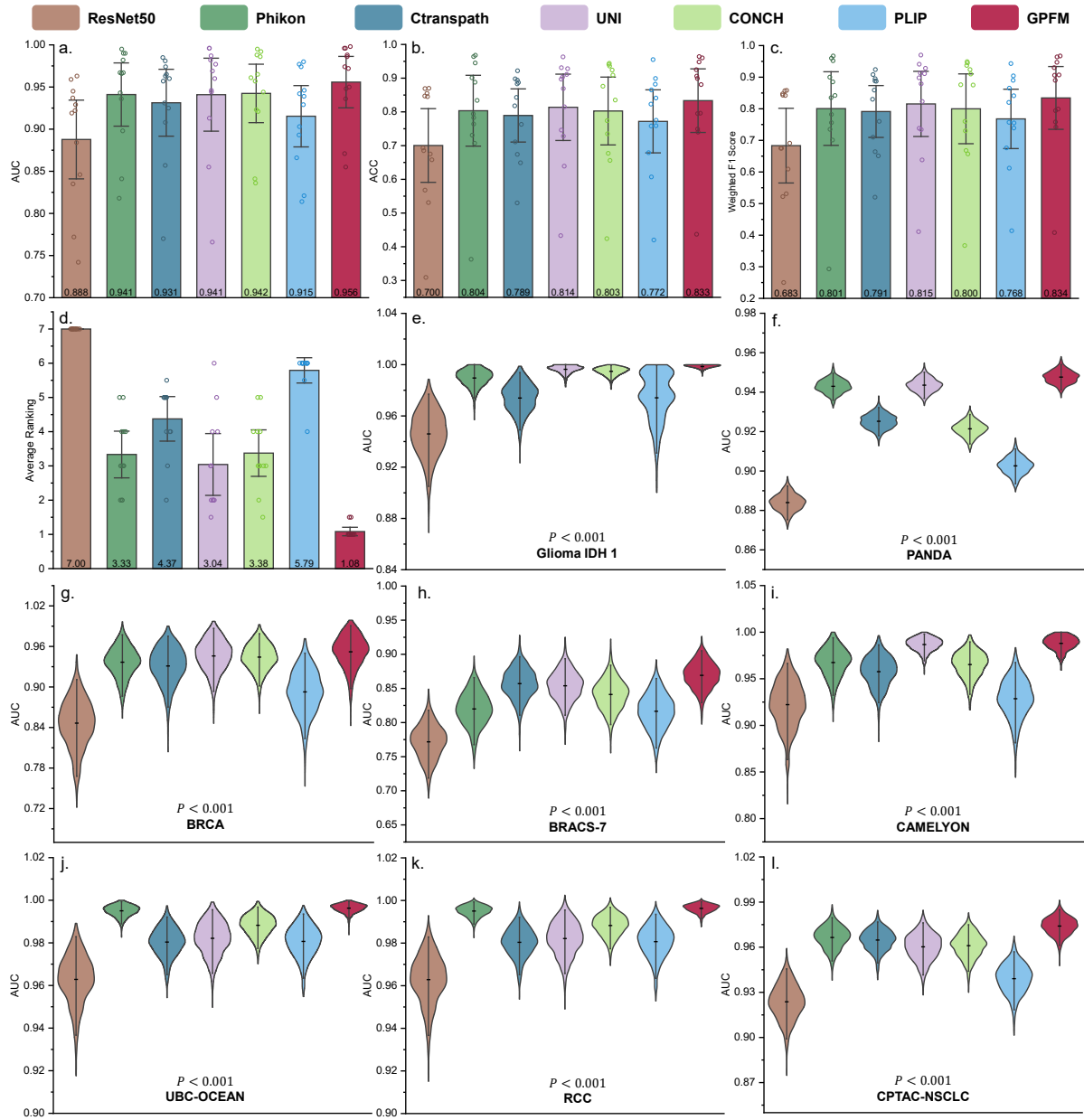


**Fig. 3 Performance of Foundation Models on WSI Classification Tasks.** a-c. Average AUC, balanced accuracy (ACC), and weighted F1 score of foundation models across 12 WSI classification tasks. d. Average ranking order of foundation models based on AUC across 12 WSI classification tasks. e-l. The AUC scores of foundation models on 8 WSI classification tasks. The violin plots depict the distribution of results based on 1,000 bootstrap replicates. The Wilcoxon signed-rank one-sided test was used to detect significant differences between the top-performing model (GPFM) and the model with the next-best performance, when applicable. Then horizontal black line in the violin plot is the mean AUC. The error bar indicates the 95% confidence interval. It is worth noting that the WSIs of BRCA and RCC are from TCGA. More results are represented in **Extended Data Figure A1**.

results illustrate that the GPFM is more generalizable than existing foundation models for gene mutation prediction tasks.

Overall, the results from both the cancer diagnosis and gene mutation prediction experiments demonstrate that the GPFM is more generalizable than existing foundation models. Compared to previous foundation models that did not utilize knowledge distillation, the GPFM was able to integrate knowledge from adopted expert models through a unified knowledge distillation mechanism. This mechanism likely allowed the GPFM to learn from a broader set of data and perspectives, which in turn boosted its performance. The ability of the GPFM to leverage knowledge distillation appears to be a key factor contributing to its superior generalizability compared to other foundation models.

## 2.2 Survival Analysis

In the context of clinical trials for oncology, survival analysis is commonly employed, with the time to an event, such as death or disease progression, serving as the primary outcome under investigation [51–54]. Accurate prediction of a patient’s survival risk can enable more targeted and effective treatment strategies. A robust foundation model is essential for improving the precision of survival risk prediction, ultimately leading to better patient outcomes. To evaluate the performance of various foundation models in survival analysis, we conducted experiments on 12 datasets. Following the methodologies of previous works [52, 54, 55], we adopted the Concordance Index (C-Index) as the evaluation metric to compare the performance of different foundation models. The overall comparison of various foundation models is presented in **Figure 4**, and the detailed experimental results are reported in **Extended Data Table A15** - **Table A19**. The survival curves of GPFM are provided in **Extended Data Figure A3** for exploring the detailed distribution of the results.

Across all 12 survival analysis tasks, the GPFM achieved an impressive average ranking score of 1.42, outperforming the competitors in 7 out of the 12 tasks. In comparison, the second-best performing model, Phikon, attained an average

ranking score of 2.08, achieving the best performance in 4 out of the 12 tasks. The detailed ranking scores of the various foundation models are presented in the **Figure 2.d**. Furthermore, when evaluated using the widely recognized C-Index metric, the GPFM once again emerged as the top performer, achieving an average C-Index of 0.726. This result represents a statistically significant improvement of 0.6% over the Phikon model ( $P < 0.001$ ), further solidifying the generalization capability of GPFM for survival analysis tasks. Among these 12 tasks, the 5-fold cross validation was adopted for 11 of them. For the CPTAC-LUAD dataset, it was evaluated directly using the ABMIL model trained on the TCGA-LUAD dataset. The experimental results showed that the C-Index of Phikon dropped from 0.738 to 0.577, a decrease of 0.161. In contrast, GPFM shows better generalization ability with its C-Index dropping from 0.739 to 0.626, a smaller decrease of 0.113. The detailed comparisons between GPFM and other foundation models are presented in **Figure 4**.

It is interesting to note that while UNI and CONCH are powerful in WSI classification tasks, they do not perform as well in survival analysis tasks. As shown in **Figure 2.d**, GPFM and Phikon almost achieved the top performance in all 12 tasks. The experimental results in both WSI classification and survival analysis clearly demonstrate the limited generalization capability of the existing foundation models. This limitation is likely due to the data distribution of their training sets and the pretraining methods they employed. While the existing foundation models lack generalization, they perform exceptionally well on specific type of tasks. By combining their strengths, it may be possible to build a more powerful and versatile model. That is exactly what we have done — by proposing the unified distillation framework in this paper to distill the capabilities of the tasks that the existing models excel at into the GPFM, thereby significantly improving its generalization ability.

## 2.3 ROI Classification

The performance of WSI classification is influenced by both the feature extractor (foundation model) and the MIL method. In the WSI classification tasks, we use the ABMIL to evaluate

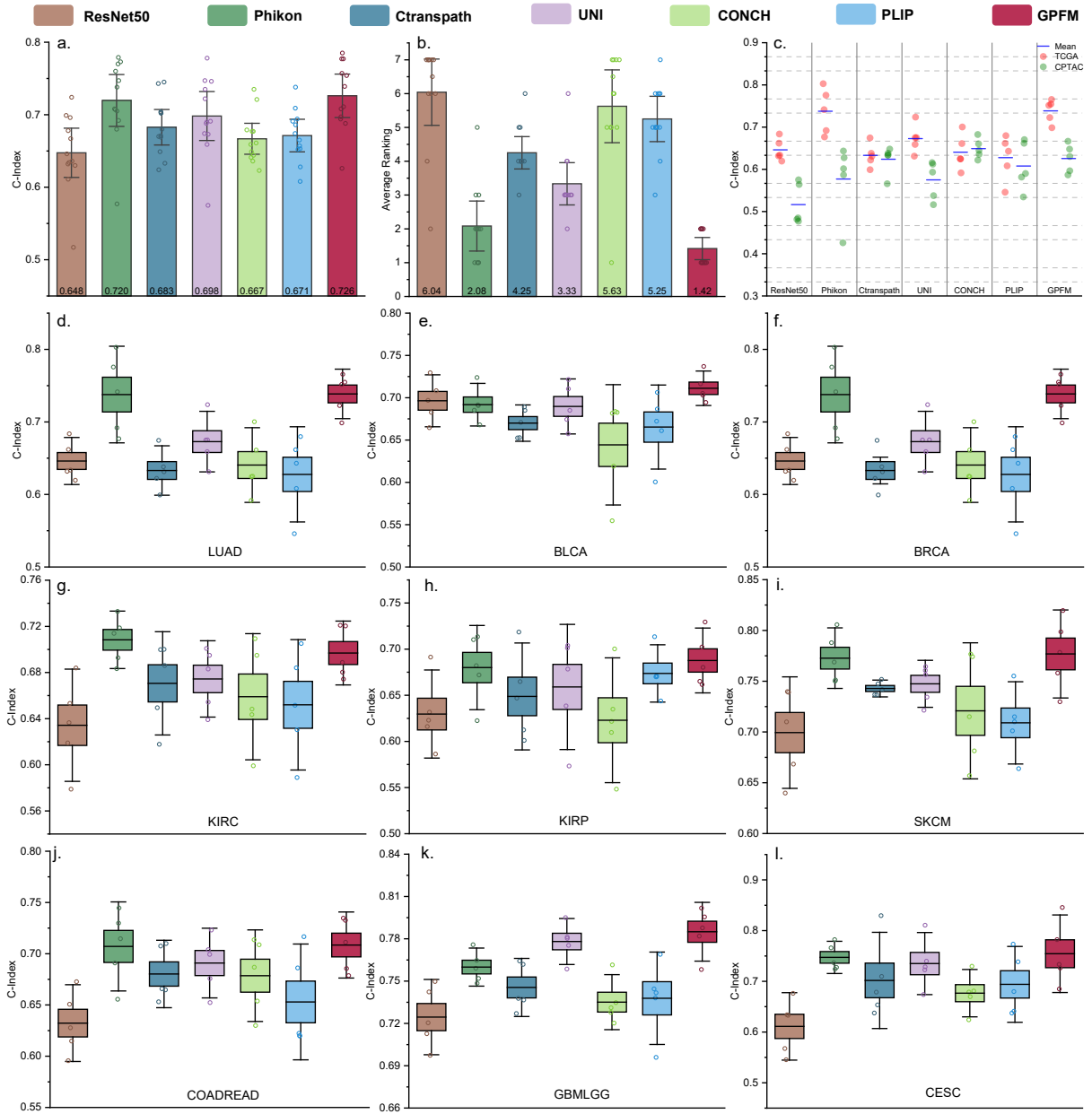


**Fig. 4 Performance of Foundation Models across 12 Survival Analysis Tasks.** **a-b.** Average C-Index and average ranking order of different foundation models across 12 survival prediction tasks. **c.** External evaluation using the LUAD-CPTAC cohort. The survival prediction model was trained on the LUAD (TCGA) cohort and subsequently tested on the LUAD-CPTAC cohort. **d-l.** C-Index of foundation models across 9 survival analysis tasks. The mean and 95% CI of 5-fold cross-validation are reported. The box represents the standard error. It is worth noting that the slides are from TCGA unless specified. More results are presented in **Extended Data Figure A1**.



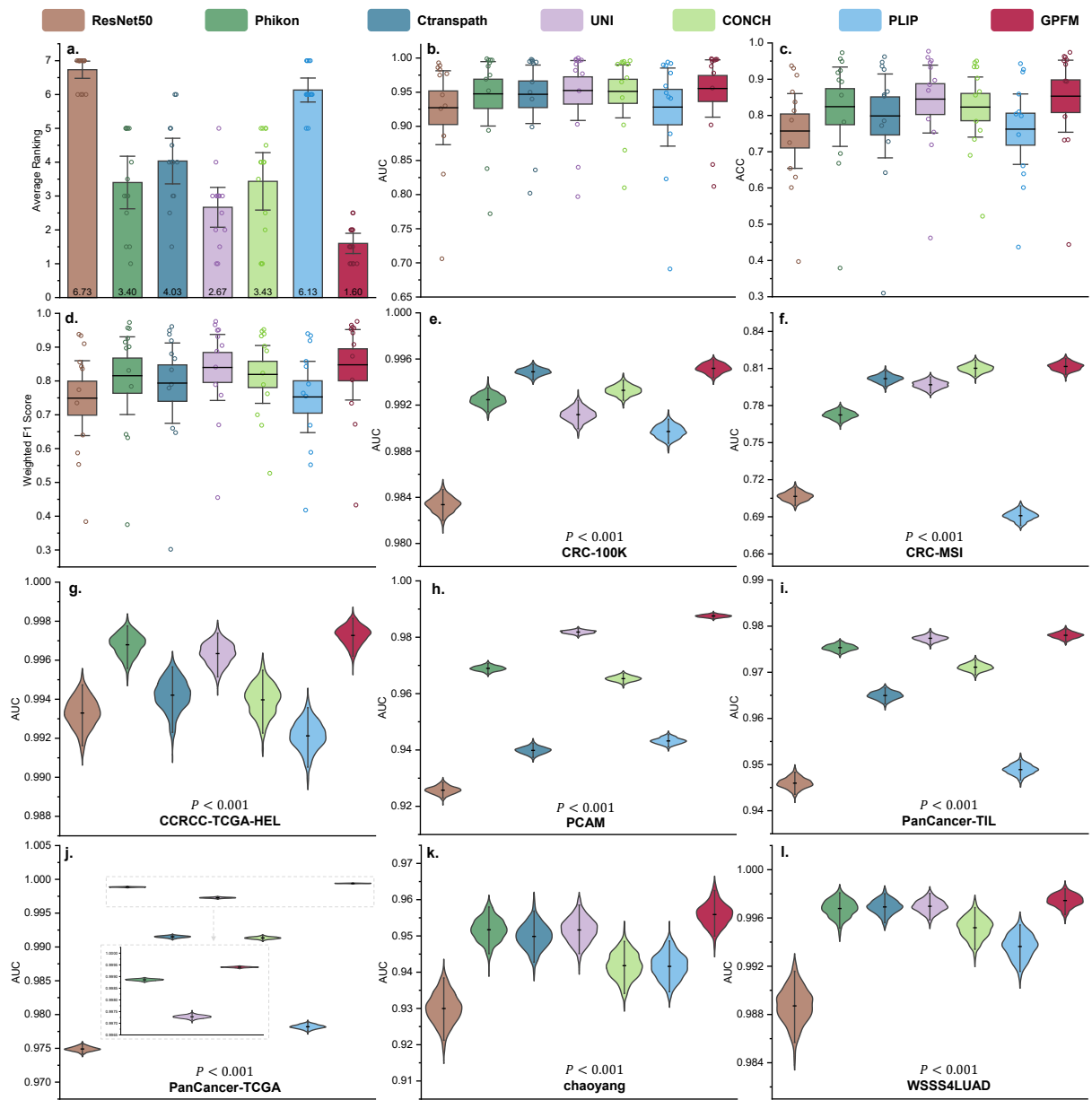


**Fig. 5 Performance of Foundation Models on Tissue Classification Tasks.** **a.** Average ranking order of foundation models based on AUC across 12 tasks. **b-d.** Average AUC of foundation models across 12 tasks. The Wilcoxon signed-ranks one-side test is employed to detect the significant difference between off-the-shelf foundation models and GPFM. **c-d.** Average weighted F1 score and balanced accuracy of foundation models across 12 tasks. **e-l.** AUC of foundation models across 8 tissue classification tasks. The Wilcoxon signed-ranks one-side test is adopted to detect significant difference between GPFM and the model with the second-best performance when GPFM achieved the highest performance. More results are presented in **Extended Data Figure A1**.

whether the features extracted by the foundation models are discriminative. In Region of Interest (ROI) classification tasks, we can directly evaluate the feature representation abilities of the foundation models without using any MIL method. Specifically, we evaluated the feature representation abilities of the foundation models by linear probe, similar to previous work [56]. The detailed experimental results can be found in the **Extended Data** Table A20 to Table A32.

Across all 12 ROI classification tasks, GPFM achieved the best ranking score of 1.60, while the second-best performing model, UNI, attained a ranking score of 2.67. The detailed ranking scores are presented in **Figure 2.d**. Furthermore, when considering the conventional metrics, GPFM attained the highest AUC of 0.955 (+0.2%, UNI,  $P<0.001$ ), the best weighted F1 score of 0.848 (+0.8%, UNI,  $P<0.001$ ), and the top balanced accuracy of 0.853 (+0.8%, UNI,  $P<0.001$ ) on average. The comparison of various foundation models is illustrated in **Figure 5**. Specifically, GPFM demonstrated the best performance in the CRC-MSI, PanCancer-TIL, PCAM, WSSS4LUAD datasets, with AUC values of 0.812 (+0.2%, CONCH,  $P<0.001$ ), 0.978 (+0.1%, UNI,  $P<0.001$ ), 0.988 (+0.6%, UNI,  $P<0.001$ ), 0.998 (+0.1%, Phikon,  $P<0.001$ ), respectively. Since ROI classification tasks are relatively easy, GPFM also jointly ranked first with other foundation models in the CRC-100K, CCRCC-TCGA-HEL, and PanCancer-TCGA datasets, achieving AUC values of 0.995 (Ctranspath), 0.997 (Phikon), 0.999 (Phikon), respectively. We also conducted external validation on Chaoyang, UniToPatho, and BreakHis datasets. Across the three external validation datasets, the GPFM achieved the best average rank of 1.5, while the second best performing model, UNI, obtained an average rank of 2.3, illustrating the generalization capability of GPFM.

Furthermore, to assess the robustness of GPFM in handling images with varying resolutions, we visualized the heatmap of attention scores between the [patch] tokens and [CLS] tokens of the ViT transformer. The visualization result is depicted in **Figure A1.1**. Across four different resolutions (224x224, 448x448, 896x896, and 1344x1344), we observed consistent attention patterns, which illustrates the robustness of GPFM in accommodating varying resolutions.

An examination of the average ranking score in **Figure 5.a** reveals that the performance of Phikon, CONCH, and UNI perform closely, with ranking score differences less than 1. This suggests that no single existing model dominates in ROI classification tasks. However, GPFM achieves an average ranking score of 1.60, more than one point ahead of the next best model, demonstrating its strength as a generalizable foundation model. The above results also verify the effectiveness of the proposed unified knowledge distillation approach. By leveraging the knowledge of all adopted expert models, the unified knowledge distillation method is able to outperform the individual expert model.

## 2.4 Pathological Image Retrieval

Image retrieval techniques could match the new patient pathology images to a curated database of previously diagnosed cases, providing pathologists with a novel tool to enhance diagnostic accuracy. Through visual inspection and comparison of similar historical cases, pathologists can leverage image search functionality to enhance their diagnostic decision-making. This approach allows pathologists to go beyond the capabilities of individual AI algorithms and instead harness the collective knowledge distilled from large repositories of validated pathology images and expert diagnoses [57–59]. In this study, we employ the CRC-100K dataset [60] for conducting pathological image retrieval tasks. This dataset comprises 100,000 non-overlapping  $224\times 224$  patches extracted from 86 human cancer tissue slides stained with H&E for training purposes. Additionally, it includes 7,180 images with  $224\times 224$  pixels extracted from 50 patients diagnosed with colorectal adenocarcinoma for testing. The dataset consists of multiple classes, including Adipose (ADI, 11,745 ROIs), Background (BACK, 11,413 ROIs), Debris (DEB, 11,851 ROIs), Lymphocytes (LYM, 12,191 ROIs), Mucus (MUC, 9,931 ROIs), Smooth muscle (MUS, 14,128 ROIs), Normal colon mucosa (NORM, 9,504 ROIs), Cancer-associated stroma (STR, 10,867 ROIs), and Colorectal adenocarcinoma epithelium (TUM, 15,550 ROIs). For training and evaluation, we utilize the official train-test split, with 100,000 samples for training and 7,180 samples for testing.

The experimental results for ROI retrieval are depicted in **Figure 6**, and the detailed results can

be found in **Extended Data Table A33**, showcasing the Top-1, Top-3, and Top-5 accuracy achieved by different foundation models. We observe that the GPFM model achieved the second-best Top-1 accuracy with a value of 0.906 (-0.5%, UNI). However, GPFM outperforms other models in terms of Top-3 and Top-5 accuracy, achieving values of 0.993 (+1.2%, UNI) and 0.995 (+1.2%, UNI) respectively. Furthermore, to gain insights into the clustering effect and the quality of feature representation, we employ t-SNE (t-Distributed Stochastic Neighbor Embedding) [61] to reduce the dimensionality of features extracted by various foundation models into 2D embedding. This visualization technique allows us to observe the clustering patterns of different classes within the dataset. As illustrated in **Extended Data Figure A4**, the features extracted by the GPFM model are clustered more tightly and the query image is also located within the candidate cluster, indicating a better clustering effect. This observation suggests that the GPFM model has superior feature representation capabilities in capturing the intrinsic patterns and structures present in the data.

## 2.5 Pathological Images VQA

Visual Question Answering (VQA) is an exciting field of artificial intelligence that aims to enable machines to answer questions about visual content. In the domain of pathology, VQA systems can be particularly powerful, allowing clinicians and researchers to quickly and accurately extract relevant information from medical images. To evaluate the effectiveness of foundation models in pathology VQA, we utilize the PathVQA dataset [62], which is the largest and most widely used dataset in the pathology domain for VQA tasks. The dataset consists of 32,799 image-question-answer triplets, divided into three subsets: a training set (50%) containing 16,400 triplets used for model training, a validation set (30%) comprising 9,840 triplets for hyperparameter tuning and overfitting prevention, and a test set (20%) including 6,560 triplets for final model performance evaluation. The performance of different foundation models on open-ended and close-ended VQA problems is presented in **Figure 6**, and detailed results can be found in **Extended Data Table A34**. Our

model achieved the second-best performance, performing only slightly lower than CONCH. It is worth noting that CONCH is a vision-language foundation model trained on million-scale image-text pairs, which naturally gives it an advantage in VQA tasks. The results demonstrate the significant potential of our approach for VQA tasks compared with other pure vision foundation models. Additionally, we have provided visualizations of the query image, questions, and answers generated by different foundation models in **Figure 6.c** and **e**. As shown in the figure, the GPFM and CONCH foundation models consistently produced more reliable answers compared to the other models evaluated.

Through unified knowledge distillation, the knowledge that CONCH acquired from the million image-text pairs can be distilled into GPFM without using any of the original image-text pair data. The performance of GPFM demonstrates the potential of leveraging textual knowledge without directly utilizing text data.

## 2.6 Pathology Report Generation

Pathology reports are essential components of the healthcare system, providing critical information to clinicians and patients about the diagnosis, prognosis, and treatment of various medical conditions. These reports summarize the findings from pathological examinations, such as biopsies, cytology samples, and surgical specimens, and play a vital role in guiding clinical decision-making. Traditionally, pathology reports are written manually by pathologists and their teams, a time-consuming and labor-intensive process. Recent advancements in natural language processing (NLP) and machine learning have enabled the development of automated pathology report generation systems, which can dramatically improve the efficiency and consistency of this critical task [63–65]. To evaluate the effectiveness of foundation models in pathology report generation, we utilize the TCGA WSI-report dataset curated by Guo et al. [63]. This dataset consists of 7,690 pairs of WSIs and their corresponding diagnosis reports, covering various diseases from different primary sites. In the task of WSI report generation, foundation models are employed to provide representations of WSIs as inputs to the report generation model. We use HistGen [63] as the

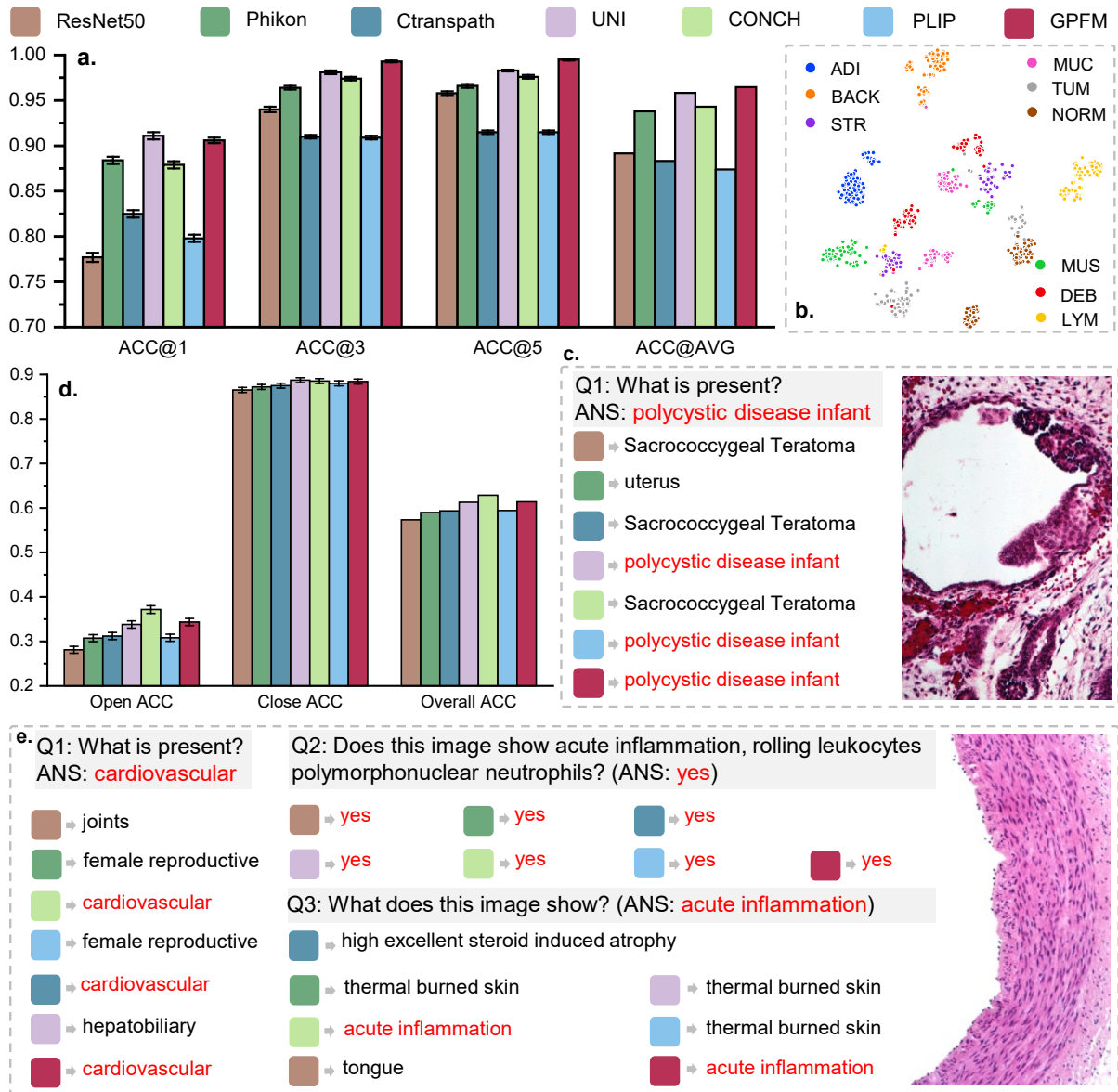


**Fig. 6 Overview of Pathology Tissue Retrieval and VQA.** **a.** The top-1, top-3, top-5, and average accuracy of different foundation models on pathology tissue retrieval tasks. **b.** The distribution of features extracted by GPFM. For each class, 100 samples from the test set were used, and a total of 900 samples were subjected to t-SNE dimensionality reduction to 2D. The different classes are distinctly colored in the 2D t-SNE plot. **c.** An open-ended question along with the answers generated by various foundation models. **d.** The performance of VQA, measured by open-ended accuracy, closed-ended accuracy, and overall accuracy, for different foundation models. **e.** Three questions and the answers generated by foundation models related to the query image.

baseline model, which takes the WSI features extracted by foundation models as input and generates the corresponding diagnosis report. For training and evaluation, we split the dataset into train-validation-test cohorts with a ratio of 7:1:2

(5,383: 769: 1,538 slides). The performance of each foundation model in report generation is presented in **Figure 7** and the detailed results are reported in **Extended Data Table A35**.

The experimental results demonstrate that Phikon achieved the best performance across all six metrics, while GPFM achieved comparable performance and ranked as the second-best model. This is quite surprising that vision foundation models (e.g., Phikon and GPFM) achieved much better performance in this task compared to vision-language foundation models such as CONCH and PLIP. A potential reason behind is that PLIP and CONCH were only trained with short descriptions or captions of pathological images, without access to the global contextual information. This may have made the text-image pairs less effective for this task compared to the VQA tasks they were originally designed for. It is worth noting that the Phikon model was pre-trained exclusively on data from TCGA. While this may enhance Phikon’s efficacy on tasks specifically utilizing data derived from the TCGA, it also limits Phikon’s generalization ability on tasks outside of the TCGA domain. To leverage the complementary strengths of existing models, the proposed unified knowledge distillation approach can distill the capabilities of Phikon in report generation into the GPFM. This synergistic integration allows us to combine the respective strengths of these foundation models, leading to the development of a more generalizable model.

## 2.7 The Effectiveness of Expert Knowledge Distillation

In the self-supervised learning framework proposed in this study, we introduced a unified knowledge distillation model to facilitate the transfer of knowledge from off-the-shelf foundation models to GPFM during the pretraining stage. To assess the effectiveness of this module, we conducted an experiment where we removed the Expert Knowledge Distillation module, resulting in a modified self-supervised learning framework known as DINOv2 [56]. We trained both DINOv2 and GPFM on the same dataset and evaluated their performance in tissue classification tasks. The experimental results are presented in **Figure 8**. More details can be found in **Extended Data Table A36**. The experimental results clearly demonstrate the positive impact of Expert Knowledge Distillation on the performance of the models across 12 tasks. Not only did

the individual task performances improve significantly, but the average performance also exhibited enhancement, with notable improvements in all three metrics. The AUC increased by 0.6%, the weighted F1 score improved by 1.8%, and the balanced accuracy showed an increase of 1.8%. These findings provide strong evidence for the effectiveness of transferring knowledge from off-the-shelf pathology foundation models through the proposed knowledge distillation learning framework.

## 3 Discussion

In this study, we construct the most comprehensive benchmark for CPath tasks to date, to the best of our knowledge. Additionally, we introduce GPFM, a generalizable foundation model designed for a broad spectrum of CPath tasks. To enhance the model’s versatility, we propose a unified knowledge distillation pretraining framework, which effectively consolidates expertise from a variety of existing models. This innovative approach ensures that GPFM can adapt and excel across different CPath tasks. To further maximize the diversity of data used for pretraining, we gathered 190 million images sourced from 47 sources, spanning 34 major tissue types. This rich dataset, combined with our advanced pretraining methodology, empowers GPFM to surpass current foundation models in performance across six major categories (WSI classification, survival analysis, ROI classification, image retrieval, VQA, and report generation) of CPath tasks, comprising a total of 39 specific tasks. Unlike other models that demonstrate proficiency in narrow domains—such as UNI [33], which specializes in ROI classification, and Phikon [32], which excels in survival analysis—GPFM showcases exceptional generalization, outperforming its counterparts across a wide array of CPath challenges by combining the strengths of expert models.

Recently, several vision-language [35, 36] and pure vision [32, 33, 37, 66] pathology foundation models have been developed. However, the overall performance of these existing foundation models is unclear due to the absence of a comprehensive benchmark. Our analysis reveals that no single existing model consistently exhibits the best performance. This is likely because each foundation model is trained using distinct datasets and

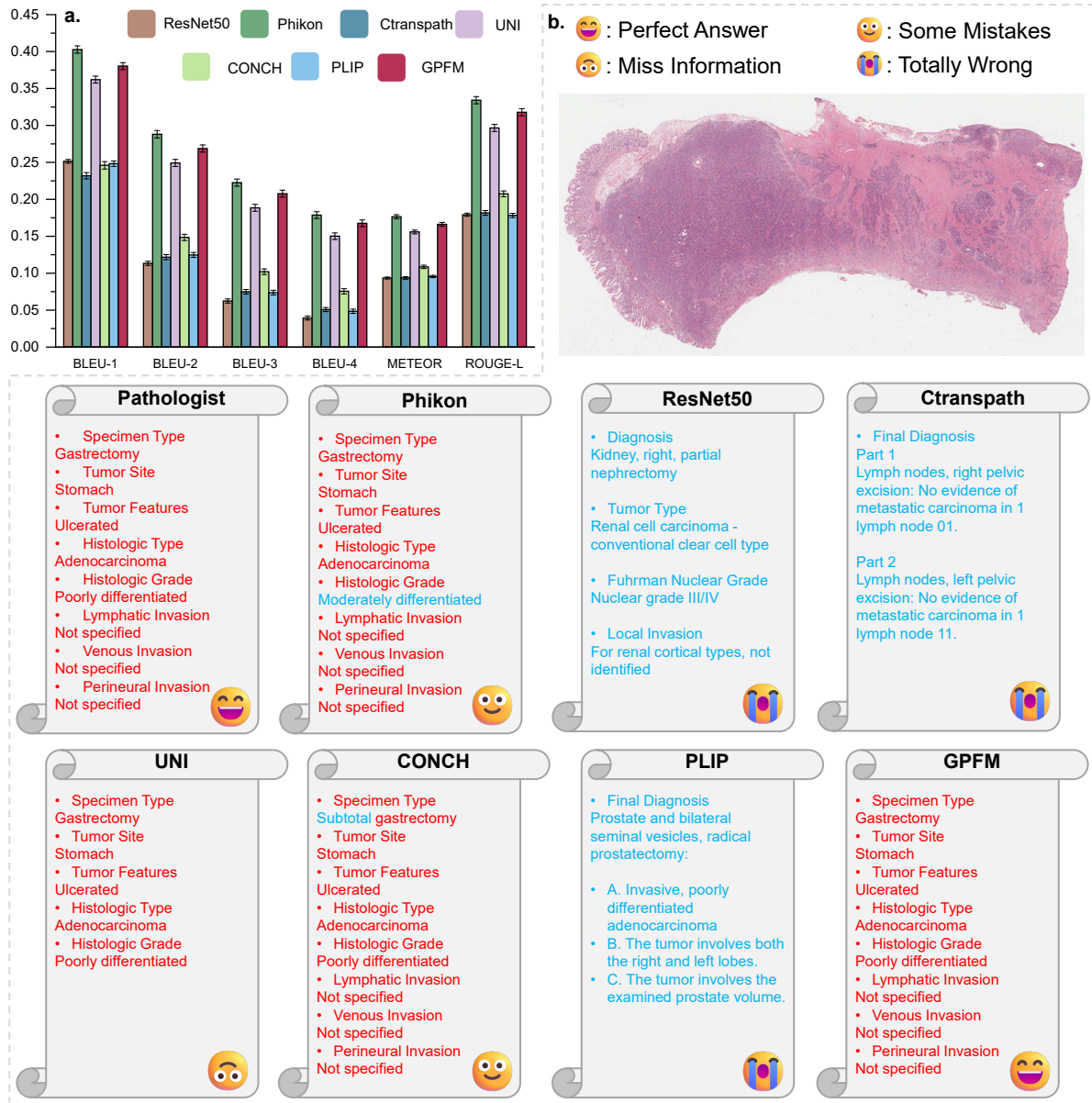


**Fig. 7 Performance of Report Generation.** **a.** The performance of report generation is measured by six different metrics. **b.** Examples of generated pathology reports. The ground truth reports provided by pathologists are shown for comparison. The text in red indicates correct predictions, and the text in blue represents incorrect predictions. The reports are formatted without changing the original content. More examples are represented in **Extended Data Figure A5** and **Figure A6**.

pretraining strategies, leading to model-specific advantages for particular domains and datasets. The root of a model’s generalization ability lies in the diversity of the training data. Unfortunately, gathering extremely large-scale diverse datasets,

especially for sensitive medical data, is very difficult due to security and privacy concerns. Therefore, it is almost impossible to access and utilize all the data used to develop the existing foundation model. Although accessing the original private training data is limited, the pretrained models

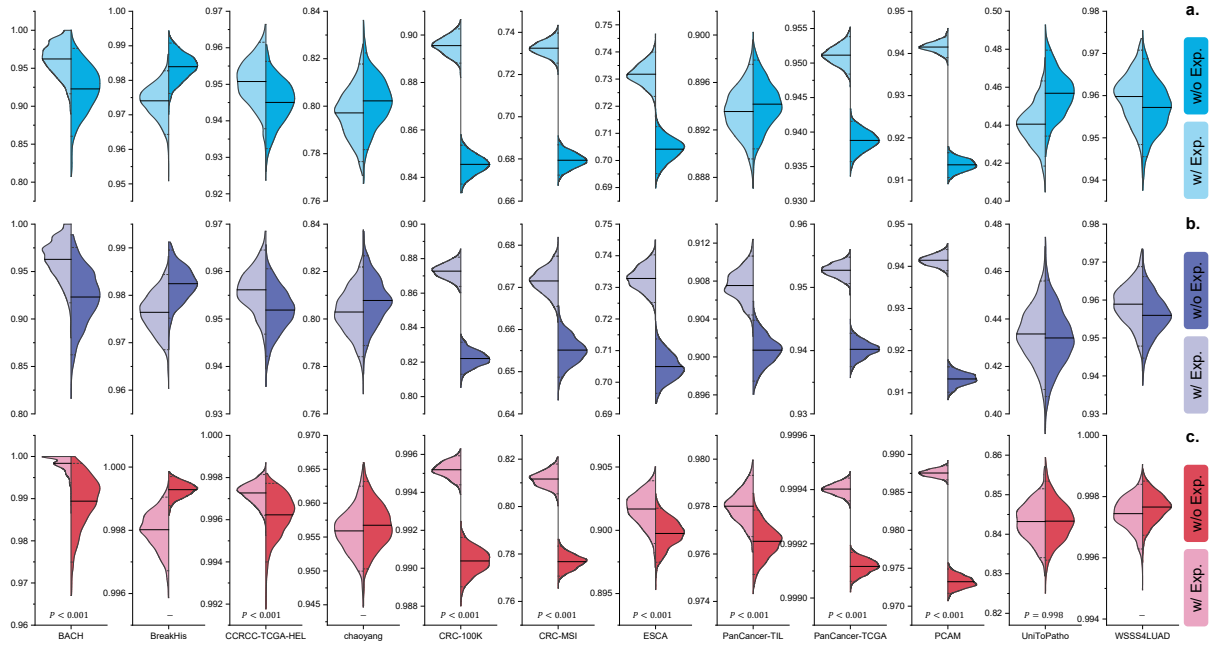


**Fig. 8 The Effectiveness of Expert Knowledge Distillation.** The figure presents the performance difference between GPFM (with Expert Knowledge Distillation) and DINOv2 (without Expert Knowledge Distillation). The horizontal black lines indicate the mean AUC. If GPFM outperforms DINOv2, the  $p$ -value is also reported. **a.** The balanced accuracy of the models with and without expert knowledge distillation. **b.** The weighted F1 score of the models with and without expert knowledge distillation. **c.** The AUC of the models with and without expert knowledge distillation. Significance testing was conducted using the Wilcoxon signed-rank one-sided test, demonstrating that expert knowledge distillation consistently improves performance across the majority of tasks, highlighting the effectiveness of this technique in enhancing the GPFM.

themselves are available. Since the knowledge of the pretrained models is derived from the training data, we can indirectly leverage this knowledge by using a unified knowledge distillation framework. It provides a feasible method to integrate knowledge from a large number of existing models under the premise of limited data and protecting data privacy, which has better feasibility and scalability in clinical practice. The significantly greater generalization ability of GPFM compared to existing foundation models, suggests that transferring knowledge from one existing model to another may be a more viable path to further advancing pathology foundation models in the future, especially given the challenges of assembling large-scale diverse medical datasets.

This study also has some limitations. While we established a most comprehensive benchmark covering 39 tasks and demonstrated that the GPFM was the most generalizable foundation model, the external validation was limited to only seven tasks. This set of external validation

tasks could be expanded in future work to further assess the generalizability of the models. It is worth highlighting that, across the seven external validation tasks, the GPFM achieved an average rank of 1.57, while the second-best performing model, UNI, achieved an average rank of 2.79. This result is consistent with the conclusions drawn from the experiments across the entire benchmark, highlighting the superior generalizability of GPFM compared to other models. Nevertheless, we also recognize that current off-the-shelf foundation models still exhibit potential in specific tasks, such as Phikon for report generation using TCGA data. This illustrates that the proposed unified knowledge distillation approach is not perfect and has room for improvement. Future research should concentrate on developing sophisticated methodologies to effectively distill and incorporate expert knowledge into one model, maximizing their potential across a broader spectrum of tasks. For example, further expanding the model’s parameter size to enhance its

adaptability, facilitating a more comprehensive assimilation of knowledge from diverse foundation models. Additionally, the current GPFM is an unimodal foundation model, which limits its ability to effectively handle cross-modal tasks such as VQA. Given the prevalence of multi-modal data in pathology, encompassing WSIs, reports, and genomic data, the development of a multi-modal pathology foundation model is more attractive. Such a model would be more adept at integrating heterogeneous information, offering a more holistic understanding of patient data and enhancing diagnostic accuracy. Last, the GPFM and existing foundation models function as ROI-level feature extractors. However, the majority of CPath tasks demand analysis at the whole-slide level. Recent advancements in long sequence modeling techniques [67, 68], exemplified by MambaMIL [69], have demonstrated success in WSI classification tasks. Developing whole slide-level foundation model could avoid the reliance on MIL frameworks, potentially leading to significant strides in CPath by providing more contextually rich interpretations of tissues.

## 4 Methods

### 4.1 Foundation Model Pretraining

CPath has emerged as a groundbreaking field that synergizes the power of AI with the expertise of pathologists, revolutionizing the practice of diagnosing and analyzing diseases. At the core of this transformative discipline lies the foundation model, which serves as the backbone for a wide range of applications in pathology. While there exist some readily available foundation models such as Ctranspath (pretrained on 32K TCGA slides) [37] and UNI [33] (pretrained on 100K private slides), the utilization of public data remains incomplete, and the evaluation of these models in CPath tasks is inadequate. The limited diversity of primary sites in the pretraining slides also restricts the adaptability of current foundation models for public CPath benchmarks. To facilitate the advancement of CPath, we meticulously curated a comprehensive dataset comprising 47 publicly available histopathology datasets, encompassing a wide spectrum of 34 distinct tissue types for pretraining and downstream task evaluation. The primary sites of tissues are

reported in **Extended Data Table A41**. Leveraging this large-scale dataset, we developed a self-supervised learning approach with unified knowledge distillation to construct a foundation model that surpasses existing models.

**Dataset Preparation.** To boost the performance of foundation models, diverse datasets with various tissues are necessary. We have collected over 33 datasets as depicted in **Extended Data Table A43** (from row 1 to row 33). To process WSIs, we employed the OpenSlide [70] and CLAM toolkit [71] to find all non-overlapping  $512 \times 512$  patches at level 0 that contain tissues. It is worth noting that we did not scale the patches to a uniform resolution, opting instead to use the original resolution of each WSI. This approach was implemented to increase the robustness of the foundation models to varying resolutions. For datasets that only contain ROI images, we extracted non-overlapping  $512 \times 512$  patches as well. Upon processing all 33 datasets, we obtained a comprehensive dataset, as presented in **Extended Data Table A40**. The dataset used for pretraining consists of 72,280 WSIs and a total of 190,212,668 patches.

**Pretraining with Self and Expert Knowledge Distillation.** In CPath, current foundation models typically rely on state-of-the-art self-supervised pretraining (SSL) methods, such as DINOv2 [56] and iBOT [72]. These methods are applied directly to either private or public datasets. For instance, Phikon [32] is constructed based on 6,093 TCGA slides using iBOT, while UNI is built upon approximately 100,000 private and public slides using DINOv2. Due to its larger training dataset and more powerful SSL methods, UNI outperforms Phikon in various tasks. However, UNI still lags behind other foundation models in tasks related to text analysis and survival analysis due to its pretraining strategy and limited coverage of primary sites. To address the limitations of current foundation models and further enhance their performance, we propose a novel pretraining strategy involving Unified Knowledge Distillation. The framework of our proposed pretraining method is illustrated in **Figure 1.c**. Similar to DINOv2, we employ teacher-student networks with masking



image modeling (MIM) loss [73] and DINO (self-distillation) [72, 74] loss to optimize the student network. Specifically, given an input image  $x$ , we obtain two augmented views,  $u$  and  $v$ . Random masking is then applied to both  $u$  and  $v$ , resulting in masked views,  $\hat{u}$  and  $\hat{v}$ . For the MIM objective, the student network takes  $\hat{u}$  and  $\hat{v}$  as inputs and aims to predict the masked tokens. With the DINO objective, we first crop  $n$  additional local views,  $w_i$ , and extract encoded class ([CLS]) tokens using the student network. Next, we obtain the [CLS] tokens of the global views ( $u$  and  $v$ ) using the teacher network. Finally, we compute the cross-entropy loss between the local views and global views’ [CLS] tokens. However, this strategy fails to leverage the knowledge from existing vision foundation models, such as UNI and vision-language foundation models like CONCH [35], which restricts their applicability to different tissue types. To transfer the knowledge from established pathology foundation models, we introduce an Expert Knowledge Distillation module to distill knowledge into the student network [38, 75]. Specifically, we adopt three foundation models that excel in classification tasks (UNI), survival analysis tasks (Phikon), and visual question answering tasks (CONCH). To achieve distillation, we use the student network to encode the global views  $u$  and  $v$  and extract the [CLS] and [PATCH] tokens. Additionally, we employ the off-the-shelf foundation models (UNI, Phikon, CONCH) to obtain their respective [CLS] and [PATCH] tokens. For aligning the class tokens, we utilize cosine similarity. As for the patch token alignment, we employ both cosine similarity and smooth L1 distance. The pseudocode for this process is outlined in Algorithm 1. The hyperparameters used in the pretraining phase are provided in **Extended Data Table A38**. Once the student network is updated, we adopt the Exponential Moving Average (EMA) to update the teacher network (GPFM).

**Baselines.** To evaluate the performance of our foundation model, GPFM, we conducted a comprehensive evaluation by comparing it with other vision foundation models, namely Ctranspath [37], Phikon [32], and UNI [33], as well as visual-language foundation models PLIP [36] and CONCH [35]. As a baseline, we also compared these foundation models with a ResNet50

[76] pretrained on the ImageNet dataset [77]. The model configurations and training details for all these models are presented in **Extended Data Table A37**. It is important to note that, for all images used in the downstream tasks, the feature extraction operations were performed on images resized to  $224 \times 224$ , unless specified otherwise.

## 4.2 WSI Classification

WSI classification holds significant importance in pathology diagnosis. It plays a crucial role in accurately analyzing and interpreting WSI, enabling pathologists to make informed diagnostic decisions. In CPath, WSI classification typically employs multiple instance learning (MIL) as the underlying methodology. The MIL approach involves the following steps: (1) Non-overlapping tissue patches are cropped from the original WSI, and features are extracted using a feature extractor. (2) A feature aggregator is applied to integrate the patch-level features into a slide-level feature, enabling classification. To preprocess the WSIs, we utilize the pipeline described in the CLAM toolkit [71]. Specifically, we employ the default segmentation configuration of CLAM to extract patches with  $512 \times 512$  pixels at level 0 for all slides. Slides with a limited number of patches are discarded. Once all patches are extracted, we resize them to  $224 \times 224$  pixels. We then utilize foundation models to extract features from the resized patches and save these features for subsequent MIL analysis. There are several MIL methods available, such as Attention-Based Multiple Instance Learning (ABMIL) [43] and TransMIL [78]. After evaluating the performance of different foundation models across various WSI classification tasks, we found that ABMIL consistently achieves the best results, which aligns with the findings from previous studies [33, 34]. Therefore, we adopt ABMIL to evaluate the performance of different foundation models in our experiments. The architecture and training details of ABMIL are presented in **Extended Data Table A39**.

To evaluate the performance of the MIL model, we assess the balanced accuracy, weighted F1 score, and AUC, which consider the class imbalance present in the dataset. Our experiments encompass 12 pathology WSI classification

tasks, including (1) breast cancer metastasis detection, (2) coarse-grained breast carcinoma subtyping, (3) fine-grained breast carcinoma subtyping, (4) lobular & ductal carcinoma subtyping, (5) ovarian cancer subtyping, (6) renal cell carcinoma (RCC) subtyping based on TCGA, (7) non-small cell lung cancer subtyping based on TCGA, (8) non-small cell lung cancer subtyping based on CPTAC, (9) prostate cancer grade assessment, (10) TP53 mutation prediction on LUAD (TCGA), (11) Brain tumor subtyping, and (12) glioma IDH1 mutation prediction. The results of our experiments are presented in **Extended Data Tables A3 to A14**. In Table A2, we showcase the average performance across all 12 WSI classification tasks, demonstrating that our method achieves the best performance.

**TCGA-NSCLC for NSCLC Subtyping (2 classes).** The TCGA-NSCLC dataset was adopted for the subtyping of NSCLC, specifically lung adenocarcinoma (LUAD) and lung squamous cell carcinoma (LUSC), obtained from the TCGA database [45]. The dataset consists of 541 LUAD slides and 512 LUSC slides. For training and evaluation, the TCGA-NSCLC cohort is label-stratified into train-validation-test sets in a ratio of 7:1:2, resulting in 738 slides for training, 105 slides for validation, and 210 slides for testing. The experimental results are presented in **Extended Data Table A3**.

**CPTAC-NSCLC for NSCLC Subtyping (2 classes).** This dataset was adopted for the subtyping of NSCLC using lung squamous cell carcinoma (LSCC) and LUAD WSIs sourced from the CPTAC data portal [79]. After preprocessing, four LSCC slides and one LUAD slide are excluded due to a limited number of tissues, resulting in a total of 1,077 LSCC slides and 1,136 LUAD slides available for further analysis. For training and evaluation, the train-validation-test cohort is label-stratified in a ratio of 7:1:2, resulting in 1549 slides for training, 222 slides for validation, and 442 slides for testing. The experimental results are reported in **Extended Data Table A4**.

**TCGA-RCC for RCC Subtyping (3**

**classes).** This task contains kidney renal papillary cell carcinoma (KIRP), kidney chromophobe (KICH) and kidney renal clear cell carcinoma (KIRC) WSIs from TCGA database [45]. After preprocessing, 3 KIRP slides without sufficient foreground are excluded, resulting in 297 KIRP slides, 121 KICH slides, and 519 KIRC slides for further analysis. For training and evaluation, we label-stratified the TCGA-RCC cohort into 7:1:2 train-validation-test (656:94:187 slides). The experimental results are reported in **Extended Data Table A5**.

**CAMELYON for Breast Metastasis Detection (2 classes).** This dataset consists of a total of 899 slides, sourced from the Cancer Metastases in Lymph Nodes Challenge 2016 (CAMELYON16, 399 slides) [46] and the CAMELYON17 (500 slides) [47]. These slides are divided into two classes: **normal** and **metastasis**, with a distribution of 557 slides classified as normal and 341 slides classified as metastasis. After image preprocessing, a corrupted normal slide is removed, resulting in a total of 898 WSIs. For training and evaluation, we employed a label-stratified train-validation-test split, with a ratio of 7:1:2. This resulted in 630 slides for training, 91 slides for validation, and 180 slides for testing. The experimental result is shown in **Extended Data Table A6**.

**TCGA-BRCA for Lobular and Ductal Carcinoma Subtyping (2 classes).** This dataset is derived from the TCGA-BRCA dataset [45], consisting of 787 invasive ductal carcinoma (IDC) slides and 198 invasive lobular carcinoma (ILC) slides. For training and evaluation, the dataset was label-stratified into train-validation-test folds in a ratio of 7:1:2, resulting in 689 slides for training, 99 slides for validation, and 197 slides for testing. The subtyping results are presented in **Extended Data Table A7**.

**BRACS for Breast Carcinoma Subtyping (3 classes & 7 classes).** This dataset involves 547 breast carcinoma H&E slides obtained from 187 patients [44]. To ensure the quality of the dataset, slides that do not meet the criteria for tumor proportion are excluded, resulting a total of 545 slides for analysis. The dataset is derived from the Breast Carcinoma Subtyping

(BRCA) task, which encompasses both coarse-grained (Benign Tumors, Atypical Tumors, and Malignant Tumors) and fine-grained (Normal, Pathological Benign, Usual Ductal hyperplasia, Flat Epithelial Atypia, Atypical Ductal Hyperplasia, Ductal Carcinoma In Situ, and Invasive Carcinoma) subtyping tasks. For training and evaluation, a label-stratified train-validation-test split is employed, maintaining a ratio of 7:1:2 based on the fine-grained classes. This partitioning results in 382 slides for training, 54 slides for validation, and 109 slides for testing. The coarse-grained and fine-grained classification results are presented in **Extended Data Table A8** and **Extended Data Table A9**, respectively.

**PANDA for Prostate Cancer Grade Assessment (6 classes)**. This dataset is designed for prostate cancer grade assessment and consists of a total of 10,616 core needle biopsies sourced from the **Prostate cANcer graDe Assessment (PANDA)** challenge [48]. After preprocessing, slides without sufficient foreground are excluded, resulting in 10,212 slides available for further analysis. The dataset includes the following subtypes: Background or Unknown (2,724 slides), Stroma (2,602 slides), Healthy Epithelium (1,321 slides), Cancerous Epithelium - Gleason 3 (1,205 slides), Cancerous Epithelium - Gleason 4 (1,187 slides), and Cancerous Epithelium - Gleason 5 (1,163 slides). For training and evaluation, the train-validation-test cohort is label-stratified in a ratio of 7:1:2, resulting in 7,143 slides for training, 1,019 slides for validation, and 2,040 slides for testing. The experimental results are reported in **Extended Data Table A10**.

**TCGA-LUAD for Lung Adenocarcinoma TP53 Gene Mutation Prediction (2 classes)**. The LUAD TP53 gene mutation prediction task consists of 469 FFPE H&E-stained WSIs of lung adenocarcinoma sourced from the TCGA database, along with their TP53 gene mutation annotations. The slides without reported TP53 mutation status are excluded from the dataset. WSIs used in this task is classified into 2 classes, namely TP53 Mutant (248 slides), and TP53 Wildtype (221 slides). For training and evaluation, we label-stratified the WSIs into a training-validation-test cohort with a ratio of 7:1:2, including 345 slides for training,

41 slides for validation, and 83 slides for testing. The experimental results for TCGA-LUAD TP53 gene mutation prediction could be found in **Extended Data Table A11**.

**TCGA-GBMLGG for Glioma IDH1 Mutation Prediction (2 classes)**. This dataset is specifically designed for glioma IDH1 mutation prediction. It comprises 804 FFPE H&E-stained WSIs sourced from the TCGA database, focusing on the subsets TCGA-GBM and TCGA-LGG [45]. Note that cases without reported IDH mutation status are excluded from the dataset. The slides in this task are classified into two classes: IDH-1 Wildtype (600 slides) and IDH-1 Mutant (204 slides). For training and evaluation, the train-validation-test cohort is label-stratified in a ratio of 7:1:2, resulting in 563 slides for training, 80 slides for validation, and 161 slides for testing. The experimental results for this task can be found in **Extended Data Table A12**.

**UBC-OCEAN for Ovarian Cancer Subtyping (5 classes)**. This dataset is a collection of 538 slides obtained from the **UBC Ovarian Cancer subtype Classification and outlier detection (UBC-OCEAN)** competition [49, 80]. The main objective of this competition is to accurately classify ovarian cancer subtypes into five distinct categories. After image preprocessing, the slides without sufficient foregrounds are excluded to reduce data noise, resulting in a total of 527 slides for further analysis. The subtypes of the dataset contains: Clear Cell (CC, 98 slides), Endometrioid (EC, 122 slides), High-Grade Serous Carcinoma (HGSC, 221 slides), Low-Grade Serous Carcinoma (LGSC, 43 slides), and Mucinous Carcinoma (MC, 43 slides). For training and evaluation, we label-stratified into train-validation-test folds into a ratio of 7:1:2 (369:52:104 slides). The experimental results are presented in **Extended Data Table A13**.

**EBRAINS for Brain Cancer Subtyping (12 classes)**. This brain tumor subtyping task contains 2,323 slides from EBRAINS Digital Tumor Atlas [50]. To ensure reliable subtyping results, we have focused on subtypes with a minimum of 26 slides. Additionally, we employed the OncoTree classification system [81] to merge subtypes and generate a final set of 12 classes. These

classes include Metastatic Tumor (46 slides), Diffuse Glioma (885 slides), Ependymoma Tumor (92 slides), Soft Tissue (66 slides), Embryonal Tumor (32 slides), Encapsulated Glioma (260 slides), Sellar Tumor (182 slides), Chordoma (28 slides), Meningothelial Tumor (476 slides), Miscellaneous Brain Tumor (146), Schwannoma (81 slides), Langerhans Cell Histiocytosis (29 slides). For training and evaluation, we label-stratified the train-validation-test cohort into 7:1:2 (1627:233:463 slides). The experimental results for this task are reported in **Extended Data Table A14**.

### 4.3 Survival Analysis

Survival analysis has traditionally been employed to analyze time-to-event data in cancer studies, focusing on events such as disease progression or patient survival. When applied to WSIs, survival analysis offers new opportunities for studying various aspects of tissue behavior and predicting patient outcomes [55, 82]. By integrating survival analysis with WSIs, researchers can investigate the correlation between specific morphological features and patient outcomes. In our study, we adopt ABMIL [43] for survival analysis with Negative Log-Likelihood (NLL) loss [83], following a similar model architecture and training configuration as WSI classification reported in **Extended Data Table A39**.

To evaluate the effectiveness of different foundation models in survival analysis, we employ a 5-fold cross-validation setting and utilize the C-index metric to assess performance. We conduct survival analysis on 11 TCGA datasets, including TCGA-BRCA, TCGA-BLCA, TCGA-KIRC, TCGA-KIRP, TCGA-LUAD, TCGA-STAD, TCGA-LUSC, TCGA-COADREAD, TCGA-GBMLGG, TCGA-SKCM, TCGA-CESC, and perform external validation on CPTAC-LUAD dataset. The experimental results are presented in **Extended Data Table A16** - **Table A19**. Additionally, **Table A15** demonstrates the average performance across all 12 survival analysis tasks, highlighting that our method achieves the highest performance in terms of the C-index metric.

**Breast Cancer Survival Prediction.** We leverage the TCGA-BRCA dataset for breast cancer survival prediction, which consists of

1,023 cases (1,089 WSIs). To ensure robust and consistent results, we maintain uniform censorship (survival status information) between the training and testing datasets. To address the challenge of imbalanced survival times, we employ a stratified approach. Specifically, we sort the cases based on survival time and divide them into four equally sized bins. We assign the label of the bin to all cases within it. As a result, for each fold of the 5-fold cross-validation, we label-stratify the train-test cohort into an 8:2 ratio, with 821 cases assigned to the training set and 202 cases allocated to the test set. The mean C-Index and standard deviation obtained from the 5-fold cross-validation results are presented in **Extended Data Table A16**.

**Bladder Cancer Survival Prediction.** For bladder cancer survival prediction, we utilize the TCGA-BLCA dataset, which includes 376 patients and a total of 446 slides. Following a similar approach used in the BRCA task, we employ 5-fold cross-validation to assess the performance of different foundation models. In each fold of the cross-validation, we stratify the train-test cohort using an 8:2 ratio, with 305 cases assigned to the training set and 71 cases allocated to the test set. This label-stratified approach guarantees a comprehensive assessment of the models, ensuring their performance is representative. The results obtained for bladder cancer survival prediction are presented in the BLCA column of **Extended Data Table A16**.

**Kidney Renal Clear Cell Carcinoma Survival Prediction.** In this task, we utilized the TCGA-KIRC dataset, which encompasses a cohort of 498 patients, accompanied by a total of 504 slides. By following a similar approach to the BRCA dataset processing, we employed a 5-fold cross-validation methodology to facilitate accurate survival prediction. To ensure the reliability and robustness of our analysis, we implemented a label-stratified train-test cohort division for each fold, maintaining an 8:2 ratio. Consequently, the training set comprised 401 cases, while the testing set consisted of 97 cases, enabling a comprehensive evaluation survival prediction. The experimental results are presented in **Extended Data Table A16**.

**Kidney Renal Papillary Cell Carcinoma Survival Prediction.** To enable accurate survival prediction for KIRP, we utilized a dataset consisting of 261 patients (285 slides) obtained from TCGA-KIRP. The slides are preprocessed similar to that employed for the BRCA survival analysis task. To ensure robustness in our survival prediction results, we employed a 5-fold cross-validation approach. For each fold, we carefully stratified the train-test cohort, ensuring a balanced representation with an 8:2 ratio. This resulted in a training set of 211 cases, while 50 cases were allocated for testing purposes. The experimental results are presented in the KIRP column of **Extended Data Table A17**.

**Stomach Adenocarcinoma Survival Prediction.** For accurate survival prediction in stomach adenocarcinoma, we utilized a dataset obtained from TCGA-STAD, which consisted of 363 patients along with 389 slides. Similar to the approach used in the BRCA analysis, we employed a 5-fold cross-validation methodology to evaluate the performance of different foundation models. For each fold, we meticulously stratified the train-test cohort, ensuring a balanced distribution with a ratio of 8:2 (293:70 cases). This resulted in a training set of 293 cases, while 70 cases were reserved for testing purposes. The detailed experimental results are presented in the STAD column of **Extended Data Table A17**.

**Cervical Squamous Cell Carcinoma and Endocervical Adenocarcinoma Survival Prediction.** To provide effective and accurate survival analysis results for patients with cervical squamous cell carcinoma and endocervical adenocarcinoma (CESC), we leveraged a dataset consisting of 250 cases (260 slides in total) obtained from TCGA-CESC. Utilizing the same experimental settings in the BRCA analysis, a 5-fold cross-validation methodology is applied to evaluate the performance of different foundation models. For each fold, we meticulously stratified the train-test cohort, resulting in a balanced distribution with a ratio of 8:2, including 203 cases for training and 47 cases for testing. The detailed experimental results are shown in the CESC column of **Extended Data Table A17**.

**Lung Adenocarcinoma Survival Prediction.**

To facilitate accurate survival prediction for lung adenocarcinoma, we utilized a dataset obtained from TCGA-LUAD, consisting of 455 cases (518 slides). Following a similar processing approach to that employed for BRCA analysis, we also employed a 5-fold cross-validation strategy for LUAD evaluation. During each fold, we meticulously label-stratified the train-test cohort with an 8:2 ratio, resulting in 366 cases for training and 89 cases for testing. The mean and standard deviation of the C-Index across the 5 folds are presented in the LUAD column of **Extended Data Table A18**.

Additionally, we conducted external validation by collecting an additional dataset of 102 lung adenocarcinoma cases (comprising 478 slides) from CPTAC. To perform the external validation, we utilized the model trained on TCGA-LUAD cohorts and directly conducted inference on the CPTAC-LUAD cases. We evaluated the results for all 5 folds and calculated the mean and standard deviation of the C-Index. The experimental results are presented in the LUAD-CPTAC column of **Extended Data Table A18**.

**Lung Squamous Cell Carcinoma Survival Prediction.** In this study, we utilized a dataset sourced from TCGA, comprising 452 cases (484 slides), for the purpose of survival prediction in lung squamous cell carcinoma (LUSC). Similar to the data processing methodology employed for BRCA survival prediction, we conducted a 5-fold cross-validation approach to assess the performance of various foundation models. During each fold, we meticulously label-stratified the train-test cohort with a ratio of 8:2, resulting in 365 cases for training and 87 cases for testing. The mean and standard deviation of the C-Index across the 5 folds are reported in the LUSC column of **Extended Data Table A18**.

**Colon & Rectum Adenocarcinoma Survival Prediction.** In this survival prediction task, we utilized a combined dataset comprising 426 cases (434 slides) from TCGA-COAD and 153 cases (154 slides) from TCGA-READ. By merging these two datasets, we obtained a larger dataset consisting of 579 cases (588 slides). Following a similar processing approach to that employed for BRCA, we conducted a 5-fold cross-validation to evaluate the performance of different foundation

models. During each fold, we label-stratified the train-test cohort with a ratio of 8:2, thereby resulting in 464 cases for training and 115 cases for testing. The mean and standard deviation of the C-Index across the 5 folds are reported in **Extended Data Table A19**.

**Glioma Survival Prediction.** In this glioma survival prediction task, we utilized a comprehensive dataset comprising 370 cases (823 slides) of glioblastoma multiforme (GBM) sourced from TCGA-GBM, and 460 cases (778 slides) of low-grade glioma (LGG) sourced from TCGA-LGG. By merging these two datasets, we created a larger dataset consisting of 830 cases (1,601 slides) for glioma survival prediction analysis. Following a data processing approach similar to that employed for BRCA, we performed a 5-fold cross-validation to evaluate the performance of the models. During each fold, we carefully label-stratified the train-test cohort with a ratio of 8:2, resulting in 667 cases for training and 163 cases for testing. The mean and standard deviation of the C-Index values across the 5 folds are reported in **Extended Data Table A19**.

**Skin Cutaneous Melanoma Survival Prediction.** In this task, we focus on predicting survival outcomes in skin cutaneous melanoma. The dataset used for this task consists of 415 cases, comprising 456 slides, sourced from the TCGA-SKCM. Similar to the data processing methodology employed in BRCA survival prediction, we employed a 5-fold cross-validation approach to evaluate the performance of different foundation models. During each fold of the cross-validation process, we meticulously stratified the train-test cohort, ensuring a ratio of 8:2 between the training and testing sets. This resulted in 337 cases being allocated for training purposes, while 78 cases were reserved for testing. The mean and standard deviation of the C-Index across the 5 folds are reported in the SKCM column of **Extended Data Table A19**.

#### 4.4 ROI Classification

For patch-level tissue classification tasks, we evaluate the transfer performance and representation ability of different foundation models using a linear probe, inspired by the approach employed in

DINOv2. [56, 84]. Initially, we extract features from the images using the pretrained foundation models. Subsequently, we employ a linear layer for performing classification. To optimize the model, we utilize AdamW [85] with an initial learning rate of  $5e-4$  and weight decay of  $1e-5$ . Additionally, we incorporate a cosine annealing scheduler to update the learning rate during training [86]. In order to obtain the best model, we set the maximum number of epochs to 3000 and implemented early stopping with patience of 100 epochs. For ensuring fair comparison, we maintain a consistent batch size of 256 across all methods.

To evaluate the performance of patch-level tissue classification, we consider the impact of class imbalance in the dataset and assess the metrics of balanced accuracy, weighted F1 score, and AUC. These metrics provide comprehensive insights into the classification performance, accounting for both accuracy and the ability to handle imbalanced class distributions. Specifically, we compare the foundation models across 12 tasks, including (1) Colorectal cancer (CRC) tissue classification, (2) Clear cell colorectal cancer (CCRCC) tissue classification, (3) Breast cancer tissue classification, (4) CRC polyp classification, (5) Microsatellite instability screening, (6) PanCancer tissue classification, (7) Tumor infiltrating lymphocyte classification, (8) Esophageal carcinoma subtyping, (9) Metastatic tissue classification, (10) Lung adenocarcinoma tissue classification, (11) Breast cancer image classification, and (12) Colon tissue classification. For all experiments in this section, we estimate the model performance using non-parametric bootstrapping with 1,000 bootstrap replicates. We employ Torchmetrics [87] for bootstrapping sampling and obtain the mean and standard deviation of the metrics. The experimental results are presented in **Extended Data Table A21** to **Extended Data Table A32**. Furthermore, we report the average performance of the patch-level tissue classification results across 12 tasks in Table A20, demonstrating the superior performance of GPFM.

**CRC-100K for Colorectal Cancer (CRC) Tissue Classification (9 classes).** This dataset consists of NCT-CRC-HE-100K and CRC-VAL-HE-7K [60]. The NCT-CRC-HE-100K comprises 100,000 non-overlapping  $224 \times 224$  patches obtained from 86 human cancer tissue slides stained with H&E. These tissue slides were

sourced from the NCT biobank (National Center for Tumor Diseases) and the UMM pathology archive (University Medical Center Mannheim). Concurrently, CRC-VAL-HE-7K consists of 7,180  $224 \times 224$  images extracted from 50 patients diagnosed with colorectal adenocarcinoma. The subtypes of this dataset contains: Adipose (ADI, 11,745 ROIs), Background (BACK, 11,413 ROIs), Debris (DEB, 11,851 ROIs), Lymphocytes (LYM, 12,191 ROIs), Mucus (MUC, 9,931 ROIs), Smooth muscle (MUS, 14,128 ROIs), Normal colon mucosa (NORM, 9,504 ROIs), Cancer-associated stroma (STR, 10,867 ROIs), Colorectal adenocarcinoma epithelium (TUM, 15,550 ROIs). For training and evaluation, we use the official train-test split(100,000: 7,180). The experimental results are reported in **Extended Data Table A21**.

**CCRCC-TCGA-HEL for CCRCC Tissue Classification (4 classes)**. This dataset [88] comprises a total of 52,713 regions of interest (ROI) images, each with dimensions of  $300 \times 300$  pixels. The dataset encompasses six distinct categories, namely: renal cancer (cancer, 13,057 ROIs), normal renal tissue (normal, 8,652 ROIs), stromal tissue (stroma, 5,460 ROIs), red blood cells (blood, 996 ROIs), empty background (empty, 16,026 ROIs), and other textures, including necrotic, torn, and adipose tissue (other, 8,522 ROIs). The image tiles were selected at random from two sources: the TCGA-KIRC WSIs and the Helsinki datasets. For training and evaluation, we focused on four specific categories: cancer, stroma, normal, and blood. This decision was made due to the potential ambiguities associated with the "other" category and the lack of meaningful information conveyed by the "empty" category. We randomly shuffle the samples and set the train-test split as a 22530:5635 ratio. The experimental results are shown in **Extended Data Table A22**.

**BACH for Breast Cancer Tissue Classification (4 classes)**. The dataset [89] is used for the breast cancer subtyping task and consists of 400 images with dimensions of  $2048 \times 1536$  pixels. The dataset is labeled into four classes: Normal (100 ROIs), Benign (100 ROIs), In situ carcinoma (100 ROIs), and Invasive carcinoma (100

ROIs). For training and evaluation, all ROIs are resized to  $224 \times 224$  pixels and we label-stratified the train-test with a ratio of 8:2 (320: 80 ROIs). The experimental results are summarized in **Extended Data Table A23**.

**UniToPatho for CRC Polyp Classification (6 classes)**. This dataset is a meticulously annotated dataset comprising 9,536 H&E stained patches extracted from 292 WSIs [90]. The primary objective of this dataset is to facilitate the training of deep neural networks for the classification of colorectal polyps and the grading of adenomas. The annotations include 6 classes: Normal tissue (950 ROIs), Hyperplastic Polyp (545 ROIs), Tubular Adenoma with High-Grade dysplasia (454 ROIs), Tubular Adenoma with Low-Grade dysplasia (3,618 ROIs), Tubulo-Villous Adenoma with High-Grade dysplasia (916 ROIs), and Tubulo-Villous Adenoma with Low-Grade dysplasia (2,186 ROIs). For training and evaluation, we use the official train-test split (6,270:2,399 ROIs). The experimental result is shown in **Extended Data Table A24**.

**CRC-MSI for MSI Screening (2 classes)**. This dataset consists of 51,918  $512 \times 512$  histological images of colorectal cancer obtained from the TCGA database [91]. In addition to the visual data, information regarding the Microsatellite Instability (MSI) status of each patient was obtained. Patients were classified into two categories: those with MSI-H (high MSI) and those with either MSI-L (low MSI) or MSS (Microsatellite Stable), collectively referred to as NonMSI-H. For training and evaluation, we use the official train-test split (19,557:32,361 ROIs). The experimental result is shown in **Extended Data Table A25**.

**PanCancer-TCGA for Tissue Classification (32 classes)**. This dataset comprises 271,170 images with dimensions of  $256 \times 256$  pixels [92]. The images were extracted from 8,736 histopathology WSIs obtained from the TCGA database. These images represent various cancer types and are annotated with following 32 classes: Head and Neck Squamous Cell Carcinoma (11,790 ROIs), Bladder Urothelial Carcinoma (9,990 ROIs), Uterine Carcinosarcoma (2,120 ROIs),

Colon Adenocarcinoma (8,150 ROIs), Lymphoid Neoplasm Diffuse Large B-cell Lymphoma (8,40 ROIs), Lung Squamous Cell Carcinoma (16,560 ROIs), Brain Lower Grade Glioma (23,530 ROIs), Esophageal Carcinoma (3,380 ROIs), Pheochromocytoma And Paraganglioma (1,350 ROIs), Sarcoma (13,480 ROIs), Glioblastoma Multiforme (23,740 ROIs), Adrenocortical Carcinoma (4,980 ROIs), Uterine Corpus Endometrial Carcinoma (12,480 ROIs), Prostate Adenocarcinoma (9,810 ROIs), Breast Invasive Carcinoma (23,690 ROIs), Stomach Adenocarcinoma (9,670 ROIs), Pancreatic Adenocarcinoma (4,090 ROIs), Skin Cutaneous Melanoma (10,060 ROIs), Ovarian Serous Cystadenocarcinoma (2,520 ROIs), Thymoma (3,600 ROIs), Lung Adenocarcinoma (16,460 ROIs), Kidney Renal Papillary Cell Carcinoma (6,790 ROIs), Testicular Germ Cell Tumors (6,010 ROIs), Kidney Renal Clear Cell Carcinoma (11,650 ROIs), Rectum Adenocarcinoma (1,880 ROIs), Cholangiocarcinoma (900 ROIs), Cervical Squamous Cell Carcinoma And Endocervical Adenocarcinoma (6,270 ROIs), Thyroid Carcinoma (11,360 ROIs), Mesothelioma (2,090 ROIs), Uveal Melanoma (1,640 ROIs), Liver Hepatocellular Carcinoma (8,370 ROIs), Kidney Chromophobe (2,460 ROIs). For training and evaluation, the train-test split is set to 21,736:54,342 ROIs. The experimental results are summarized in **Extended Data Table A26** indicating that GPFM outperforms other models across all three metrics.

**PanCancer-TIL for TIL classification (2 classes).** This dataset [93, 94] is collected for tumor infiltrating lymphocyte (TIL) classification including 304,097 images with a size of  $100 \times 100$  pixels at 0.5 micrometers per pixel. The images are labeled with the following two classes: TIL-positive (if there are at least two TILs present in the image, 54,910 ROIs) and TIL-negative (249,187 ROIs). For training and evaluation, we use the official train-val-test split (209,221:38,601:56,275 ROIs). To ensure consistency, we resize all images to  $256 \times 256$  pixels. We employ the validation set to select the best model and subsequently evaluate its performance on the test set. The experimental results are presented in **Extended Data Table A27**.

**ESCA for Esophageal Carcinoma Subtyping (11 classes).** This dataset [95] comprises 367,229 images with size of  $256 \times 256$  pixels. These patches were obtained from 320 H&E WSIs of esophageal adenocarcinoma and adenocarcinoma of the esophagogastric junction, specifically, 22 slides from University Hospital Cologne (UKK), 62 slides from Landeskrankenhaus Wiener Neustadt (WNS), 22 slides from TCGA, and 214 slides from the University Hospital Berlin Charite (CHA). These images were annotated and labeled with one of eleven classes: adventitia (71,131 ROIs), lamina propria mucosae (2,173 ROIs), muscularis mucosae (2,951 ROIs), muscularis propria (83,358 ROIs), regression tissue (56,490 ROIs), mucosa gastric (44,416 ROIs), mucosa oesophagus (18,561 ROIs), submucosa (22,117 ROIs), submucosal glands (1,516 ROIs), tumor (63,863 ROIs), and ulceration (753 ROIs). For training and evaluation, we adopted CHA dataset, containing 178,187 ROIs, as the training set, and we combined the UKK, WNS, and TCGA datasets as a single testing cohort consisting of 189,142 ROIs. In our experiment, all images were resized to  $224 \times 224$  pixels to ensure consistency, the experimental result is shown in **Extended Data Table A28**.

**PCAM for Metastatic Tissue Classification (2 classes).** This dataset consists of 327,680 color images ( $96 \times 96$  pixels) extracted from CAMELYON16 [46, 96]. Each image is annotated with a binary label indicating the presence of metastatic tissue. For training and evaluation, we adopt the official train-validation-test split (262,144: 32768:32768 ROIs) and resize all images to  $224 \times 224$  in our experiment. The experimental results are presented in **Extended Data Table A29**.

**WSSS4LUAD for Lung Adenocarcinoma Tissue Classification (3 classes).** This dataset [97, 98] was collected from Guangdong Provincial People’s Hospital (GDPH) and TCGA. It consists of 10,091 images with the following three common and meaningful tissue types: tumor epithelial tissue (6,579 ROIs), tumor-associated stroma tissue (1,680 ROIs), and normal tissue (1,832 ROIs). It is worth noting that, in WSSS4LUAD dataset, one image may belong to several categories. To avoid ambiguity, we only choose one label for



each image based on the order of diagnosability (i.e., from tumor epithelial tissue to normal tissue). For training and evaluation, all images were resized to  $224 \times 224$  pixels and we label-stratified the train-test with a ratio of 8:2 (8,072:2019 ROIs). The experimental results are presented in **Extended Data Table A30**.

**BreakHis for Breast Cancer Image Classification (2 classes)**. This dataset [99] is collected for breast cancer histopathological image classification containing two main groups: benign tumors (2,480 ROIs) and malignant tumors (5,429 ROIs). The ROIs in this dataset have 4 different magnifications ( $40\times$ ,  $100\times$ ,  $200\times$ , and  $400\times$ ). For training and evaluation, we resized all images to  $224 \times 224$  pixels to ensure consistency and label-stratified the train-test with a ratio of 8:2 (6,327:1,582 ROIs). The experimental results are presented in **Extended Data Table A31**.

**Chaoyang for Colon Tissue Classification (4 classes)**. This dataset [100] contains colon patches from Chaoyang hospital including 1,816 normal ROIs, 1,163 serrated ROIs, 2,244 adenocarcinoma ROIs, and 937 adenoma ROIs. For training and evaluation, we resize all patches to  $224 \times 224$  pixels and use official train-test split (4,021: 2,139 ROIs). The experimental results are presented in Table A32.

#### 4.5 Pathological Tissue Retrieval.

In the linear probe evaluation tasks, we extract semantically-rich features using different foundation models and then construct a task-specific classifier. These features are not only applicable for supervised learning but also prove to be valuable for image-to-image retrieval. The primary goal of this application is to retrieve images that share the same class label as a given query image, thereby facilitating efficient image retrieval. To initiate the pathological tissue image retrieval process, we begin by embedding all images using pretrained foundation models. Next, each image in the test set is treated as a query and compared against the images in the training set. To ensure that all features have a comparable impact on the computation of similarity, we independently normalize each feature component to the range  $[0, 1]$

[101]. This normalization process involves calculating the mean and variance of the training set features, which are then used to normalize both the training and testing features.

To evaluate the similarity between the query image and candidate images, we employ the L2 distance metric. A lower distance value indicates a higher degree of similarity between the images. The retrieved images are subsequently ranked based on their similarity scores, and the corresponding class labels are utilized to evaluate the success of the retrieval process. To assess the retrieval performance, we employ evaluation metrics such as Acc@K, where K represents the top K retrieved images (typically 1, 3, and 5). Similar to the patch-level classification evaluation, we estimate the model performance using non-parametric bootstrapping with 1,000 bootstrap replicates. Due to the limitation of the number of classes, we primarily focus on the CRC tissue retrieval tasks, and the experimental results are presented in Table A33.

#### 4.6 Pathology Visual Question Answering

The objective of this subsection is to evaluate the performance of our proposed pathology foundation model in the context of Visual Question Answering (VQA) tasks. To achieve this, we utilize the PathVQA dataset [62], a widely recognized and extensively used benchmark in the pathology domain, as the evaluation dataset for our experiments. This dataset provides a comprehensive assessment of the model’s ability to comprehend and reason about visual pathology information, enabling accurate answering of queries related to observed features. To ensure a rigorous and comparative analysis, we adopt the Multi-modal Unified Medical Captioning (MUMC) method [102], which currently represents the state-of-the-art approach on the PathVQA dataset. The MUMC method has exhibited superior performance in leveraging the synergies between visual and textual information for medical image understanding tasks.

The VQA model architecture consists of four main components: the image encoder, text encoder, multimodal encoder, and answering

decoder. The image encoder is responsible for capturing domain-specific visual features. We employ various pathology foundation models as the image encoder. During the fine-tuning process, the weights of the image encoder are kept frozen to preserve the integrity of the pre-trained visual representations and focus on learning task-specific multimodal interactions. The text encoder is designed to process textual inputs, specifically the questions related to the pathology images. We utilize a 6-layer transformer architecture for the text encoder. It is initialized with the first six layers of a pre-trained BERT model, which has a strong track record in language understanding tasks and has demonstrated excellent performance in several medical and clinical applications. The multimodal encoder is responsible for fusing visual and textual features. It consists of the last six layers of the pre-trained BERT model and incorporates cross-attention mechanisms at each layer. This integration enables the model to learn robust multimodal interactions, which are crucial for effectively answering questions based on the provided pathology images. The answering decoder, which comprises a 6-layer transformer, receives the multimodal embeddings generated by the previous components and generates text tokens corresponding to the answers. During the training stage, we fine-tuned the model for a total of 100 epochs using a batch size of 8. To optimize the model, we employed the AdamW optimizer with an initial learning rate of  $2 \times 1e-5$ . Throughout the training process, the learning rate was decayed to  $1e-8$  to ensure gradual convergence and stability. To evaluate the performance of the VQA models, we adopt accuracy as the metric, which is consistent with previous research studies [102, 103]. We treat VQA as a generative task by calculating similarities between the generated answers and the candidate list of answers, selecting the answer with the highest score as the final answer. The experimental result is reported in Table A34.

#### 4.7 Pathology Report Generation

The task of pathology report generation is inspired by existing works on Chest X-ray and other medical report generation [104–106]. In this

task, the report generation model takes a WSI as input and generates the corresponding pathology report. Specifically, the input WSI is first processed by foundation models to extract an initial representation. This representation is then fed into the encoder-decoder architecture of report generation models to produce the decoded pathology report. During this process, the visual encoder further processes the initial representations of WSIs through specific designs [63, 105, 106] to obtain the optimal WSI features for the report decoding stage. The text decoder of the model then utilizes these features for report generation. A good initial representation of WSI could significantly facilitate both the visual encoding and textual decoding stages. Consequently, the quality of the generated report is directly influenced by the representations provided by the foundation models. In this task, we adopt the HistGen model [63] for WSI report generation and set the learning rate to  $1e-4$ , and weight decay to 0.8 per epoch. The model is trained for 40 epochs with batch size 1 using features extracted from different foundation models.

To evaluate the report generation performance of foundation models, we utilize natural language generation metrics including BLEU [107], METEOR [108], and ROUGE-L [109], in which BLEU is further split into BLEU-1, BLEU-2, BLEU-3, and BLEU-4 for evaluation of different granularity. These metrics provide a robust framework for evaluating machine-generated text, each bringing unique strengths to assess different aspects of text quality. This task is conducted on the TCGA WSI-Report dataset proposed in [63], containing 7,690 WSIs and the paired diagnosis reports in total. A 7:1:2 train-validation-test split is employed and the experimental results are reported in **Extended Data Table A35**.

#### 4.8 Computing Software and Hardware

In this project, we utilized PyTorch [110] (version 2.1.2 with CUDA 12.1) for both pretraining and evaluating downstream tasks. To pretrain the GPFM model, we incorporated established foundation models, namely UNI, Phikon, and CONCH, as additional teachers. It is worth noting that access to UNI and CONCH requires a prior application submission. The GPFM model

was pretrained using the FullyShardedDataParallel (FSDP) technique on  $2 \times 8$  80GB NVIDIA H800 GPU nodes. All other data processing and evaluation for downstream tasks were carried out on a server equipped with  $8 \times$  NVIDIA RTX 3090 GPUs. To assess the model’s performance, we employed Torchmetrics [87] and Scikit-learn [111] for metric evaluation. For WSI processing, we relied on openslide-python (version 1.2.0) [70] and the CLAM [71] codebase. Pathology VQA evaluation was conducted using the MUMC [102] codebase. Furthermore, for histology report generation, we utilized the HistGen [63] codebase. Please refer to **Extended Data Table A42** for a comprehensive list of the aforementioned models and libraries utilized in this study.

## 5 Data availability

This study incorporates a total of 47 datasets. Out of these, 33 datasets are utilized for pretraining, and a subset of them is also employed for evaluation purposes. The remaining 14 datasets are specifically dedicated to downstream task evaluation. For detailed information about the data used in this project, please refer to **Extended Data Table A43**. The splits of the dataset can be found in our GitHub repository.

## 6 Code availability

The code and weights of the GPFM will be made available upon acceptance. The code and weights of the GPFM have been made available on GitHub (<https://github.com/birkhoffkiki/GPFM/>).

## 7 Ethics declarations

This project has been reviewed and approved by the Human and Artefacts Research Ethics Committee (HAREC). The protocol number is HREP-2024-0212.

## 8 Author contributions

J.M. conceived the study and designed the experiments. J.M., Z.G., and F.Z. collected the data for self-supervised learning and downstream task evaluation. J.M. performed foundation model pre-training and conducted patch-level tissue classification tasks. Y.L. and X.J. participated in

discussions regarding the design of the self-supervised learning framework and were responsible for reproducing the foundation models. J.M., F.Z., and Y.C. evaluated the weakly-supervised WSI classification task. Z.G. performed survival analysis and report generation tasks. Y.W. and Y.X. conducted pathological image retrieval and curated the data of WSI-report pairs. Z.Z. performed pathological image visual question answering. C.J. assisted in result analysis and the creation of visualized attention maps. J.M. and Z.G. prepared the manuscript with input from all co-authors. R.C.K.C, A.H., and L.L. provided medical guidance. J.W. offered insightful suggestions for the experimental design and thoughtfully directing the research trajectory. K.T.C reviewed and refined the draft. H.C. supervised the research.

## Acknowledgements

This work was supported by the National Natural Science Foundation of China (No. 62202403), Hong Kong Innovation and Technology Fund (No. PRP/034/22FX), Research Grants Council of the Hong Kong Special Administrative Region, China (No. R6003-22) and HKUST Frontier Technology Research for Joint Institutes with Industry (No. OKT24EG01). We also thank the support of HKUST SuperPod for providing the GPU platform for foundation model pretraining.

## References

- [1] Bejnordi, B.E., Veta, M., Van Diest, P.J., Van Ginneken, B., Karssemeijer, N., Litjens, G., Van Der Laak, J.A., Hermsen, M., Manson, Q.F., Balkenhol, M., *et al.*: Diagnostic assessment of deep learning algorithms for detection of lymph node metastases in women with breast cancer. *Jama* **318**(22), 2199–2210 (2017)
- [2] Bandi, P., Geessink, O., Manson, Q., Van Dijk, M., Balkenhol, M., Hermsen, M., Bejnordi, B.E., Lee, B., Paeng, K., Zhong, A., *et al.*: From detection of individual metastases to classification of lymph node status at the patient level: the camelyon17 challenge. *IEEE transactions on medical imaging* **38**(2), 550–560 (2018)

- [3] Tolkach, Y., Dohmgörge, T., Toma, M., Kristiansen, G.: High-accuracy prostate cancer pathology using deep learning. *Nature Machine Intelligence* **2**(7), 411–418 (2020)
- [4] Bulten, W., Pinckaers, H., Boven, H., Vink, R., Bel, T., Ginneken, B., Laak, J., Kaa, C., Litjens, G.: Automated deep-learning system for gleason grading of prostate cancer using biopsies: a diagnostic study. *The Lancet Oncology* **21**(2), 233–241 (2020)
- [5] Bera, K., Schalper, K.A., Rimm, D.L., Velcheti, V., Madabhushi, A.: Artificial intelligence in digital pathology—new tools for diagnosis and precision oncology. *Nature reviews Clinical oncology* **16**(11), 703–715 (2019)
- [6] Echle, A., Rindtorff, N.T., Brinker, T.J., Luedde, T., Pearson, A.T., Kather, J.N.: Deep learning in cancer pathology: a new generation of clinical biomarkers. *British journal of cancer* **124**(4), 686–696 (2021)
- [7] Hahn, W.C., Bader, J.S., Braun, T.P., Califano, A., Clemons, P.A., Druker, B.J., Ewald, A.J., Fu, H., Jagu, S., Kemp, C.J., *et al.*: An expanded universe of cancer targets. *Cell* **184**(5), 1142–1155 (2021)
- [8] Niazi, M.K.K., Parwani, A.V., Gurcan, M.N.: Digital pathology and artificial intelligence. *The lancet oncology* **20**(5), 253–261 (2019)
- [9] Deng, S., Zhang, X., Yan, W., Chang, E.I.-C., Fan, Y., Lai, M., Xu, Y.: Deep learning in digital pathology image analysis: a survey. *Frontiers of medicine* **14**, 470–487 (2020)
- [10] Srinidhi, C.L., Ciga, O., Martel, A.L.: Deep neural network models for computational histopathology: A survey. *Medical image analysis* **67**, 101813 (2021)
- [11] Song, A.H., Jaume, G., Williamson, D.F., Lu, M.Y., Vaidya, A., Miller, T.R., Mahmood, F.: Artificial intelligence for digital and computational pathology. *Nature Reviews Bioengineering* **1**(12), 930–949 (2023)
- [12] Coudray, N., Ocampo, P.S., Sakellaropoulos, T., Narula, N., Snuderl, M., Fenyö, D., Moreira, A.L., Razavian, N., Tsirigos, A.: Classification and mutation prediction from non-small cell lung cancer histopathology images using deep learning. *Nature medicine* **24**(10), 1559–1567 (2018)
- [13] Bilal, M., Raza, S.E.A., Azam, A., Graham, S., Ilyas, M., Cree, I.A., Snead, D., Minhas, F., Rajpoot, N.M.: Development and validation of a weakly supervised deep learning framework to predict the status of molecular pathways and key mutations in colorectal cancer from routine histology images: a retrospective study. *The Lancet Digital Health* **3**(12), 763–772 (2021)
- [14] Zamanitajeddin, N., Jahanifar, M., Bilal, M., Eastwood, M., Rajpoot, N.: Social network analysis of cell networks improves deep learning for prediction of molecular pathways and key mutations in colorectal cancer. *Medical Image Analysis* **93**, 103071 (2024)
- [15] Wulczyn, E., Steiner, D.F., Moran, M., Plass, M., Reihls, R., Tan, F., Flament-Auvigne, I., Brown, T., Regitnig, P., Chen, P.-H.C., *et al.*: Interpretable survival prediction for colorectal cancer using deep learning. *NPJ digital medicine* **4**(1), 71 (2021)
- [16] Mobadersany, P., Yousefi, S., Amgad, M., Gutman, D.A., Barnholtz-Sloan, J.S., Velázquez Vega, J.E., Brat, D.J., Cooper, L.A.: Predicting cancer outcomes from histology and genomics using convolutional networks. *Proceedings of the National Academy of Sciences* **115**(13), 2970–2979 (2018)
- [17] Courtiol, P., Maussion, C., Moarii, M., Pronier, E., Pilcer, S., Sefta, M., Manceron, P., Toldo, S., Zaslavskiy, M., Le Stang, N., *et al.*: Deep learning-based classification of mesothelioma improves prediction of patient outcome. *Nature medicine* **25**(10), 1519–1525 (2019)

- [18] Vanguri, R.S., Luo, J., Aukerman, A.T., Egger, J.V., Fong, C.J., Horvat, N., Pagano, A., Araujo-Filho, J.d.A.B., Geneslaw, L., Rizvi, H., *et al.*: Multimodal integration of radiology, pathology and genomics for prediction of response to pd-(l) 1 blockade in patients with non-small cell lung cancer. *Nature cancer* **3**(10), 1151–1164 (2022)
- [19] Zhang, Y., Yang, Z., Chen, R., Zhu, Y., Liu, L., Dong, J., Zhang, Z., Sun, X., Ying, J., Lin, D., *et al.*: Histopathology images-based deep learning prediction of prognosis and therapeutic response in small cell lung cancer. *NPJ digital medicine* **7**(1), 15 (2024)
- [20] Hu, J., Cui, C., Yang, W., Huang, L., Yu, R., Liu, S., Kong, Y.: Using deep learning to predict anti-pd-1 response in melanoma and lung cancer patients from histopathology images. *Translational oncology* **14**(1), 100921 (2021)
- [21] Kang, M., Song, H., Park, S., Yoo, D., Pereira, S.: Benchmarking self-supervised learning on diverse pathology datasets. In: *Proceedings of the IEEE/CVF Conference on Computer Vision and Pattern Recognition*, pp. 3344–3354 (2023)
- [22] Li, B., Li, Y., Eliceiri, K.W.: Dual-stream multiple instance learning network for whole slide image classification with self-supervised contrastive learning. In: *Proceedings of the IEEE/CVF Conference on Computer Vision and Pattern Recognition*, pp. 14318–14328 (2021)
- [23] Lazard, T., Lerousseau, M., Decencière, E., Walter, T.: Giga-ssl: Self-supervised learning for gigapixel images. In: *Proceedings of the IEEE/CVF Conference on Computer Vision and Pattern Recognition*, pp. 4304–4313 (2023)
- [24] Schirris, Y., Gavves, E., Nederlof, I., Horlings, H.M., Teuwen, J.: Deepsmile: Contrastive self-supervised pre-training benefits msi and hrd classification directly from h&e whole-slide images in colorectal and breast cancer. *Medical image analysis* **79**, 102464 (2022)
- [25] Vu, Q.D., Rajpoot, K., Raza, S.E.A., Rajpoot, N.: Handcrafted histological transformer (h2t): Unsupervised representation of whole slide images. *Medical image analysis* **85**, 102743 (2023)
- [26] Claudio Quiros, A., Coudray, N., Yeaton, A., Sunhem, W., Murray-Smith, R., Tsirigos, A., Yuan, K.: Adversarial learning of cancer tissue representations. In: *Medical Image Computing and Computer Assisted Intervention–MICCAI 2021: 24th International Conference, Strasbourg, France, September 27–October 1, 2021, Proceedings, Part VIII* 24, pp. 602–612 (2021)
- [27] Jiang, S., Hondelink, L., Suriawinata, A.A., Hassanpour, S.: Masked pre-training of transformers for histology image analysis. *Journal of Pathology Informatics*, 100386 (2024)
- [28] Bommasani, R., Hudson, D.A., Adeli, E., Altman, R., Arora, S., Arx, S., Bernstein, M.S., Bohg, J., Bosselut, A., Brunskill, E., *et al.*: On the opportunities and risks of foundation models. *arXiv preprint arXiv:2108.07258* (2021)
- [29] Zhou, C., Li, Q., Li, C., Yu, J., Liu, Y., Wang, G., Zhang, K., Ji, C., Yan, Q., He, L., *et al.*: A comprehensive survey on pretrained foundation models: A history from bert to chatgpt. *arXiv preprint arXiv:2302.09419* (2023)
- [30] Moor, M., Banerjee, O., Abad, Z.S.H., Krumholz, H.M., Leskovec, J., Topol, E.J., Rajpurkar, P.: Foundation models for generalist medical artificial intelligence. *Nature* **616**(7956), 259–265 (2023)
- [31] Wang, X., Yang, S., Zhang, J., Wang, M., Zhang, J., Yang, W., Huang, J., Han, X.: Transformer-based unsupervised contrastive learning for histopathological image classification. *Medical image analysis* **81**, 102559 (2022)
- [32] Filiot, A., Ghermi, R., Olivier, A., Jacob, P., Fidon, L., Mac Kain, A., Saillard, C., Schiratti, J.-B.: Scaling self-supervised learning

- for histopathology with masked image modeling. medRxiv, 2023–07 (2023)
- [33] Chen, R.J., Ding, T., Lu, M.Y., Williamson, D.F., Jaume, G., Song, A.H., Chen, B., Zhang, A., Shao, D., Shaban, M., *et al.*: Towards a general-purpose foundation model for computational pathology. *Nature Medicine* **30**(3), 850–862 (2024)
- [34] Vorontsov, E., Bozkurt, A., Casson, A., Shaikovski, G., Zelechowski, M., Liu, S., Mathieu, P., Eck, A., Lee, D., Viret, J., *et al.*: Virchow: A million-slide digital pathology foundation model. arXiv preprint arXiv:2309.07778 (2023)
- [35] Lu, M.Y., Chen, B., Williamson, D.F., Chen, R.J., Liang, I., Ding, T., Jaume, G., Odintsov, I., Le, L.P., Gerber, G., *et al.*: A visual-language foundation model for computational pathology. *Nature Medicine* **30**(3), 863–874 (2024)
- [36] Huang, Z., Bianchi, F., Yuksekgonul, M., Montine, T.J., Zou, J.: A visual-language foundation model for pathology image analysis using medical twitter. *Nature medicine* **29**(9), 2307–2316 (2023)
- [37] Wang, X., Yang, S., Zhang, J., Wang, M., Zhang, J., Yang, W., Huang, J., Han, X.: Transformer-based unsupervised contrastive learning for histopathological image classification. *Medical image analysis* **81**, 102559 (2022)
- [38] Hinton, G., Vinyals, O., Dean, J.: Distilling the knowledge in a neural network. arXiv preprint arXiv:1503.02531 (2015)
- [39] Gou, J., Yu, B., Maybank, S.J., Tao, D.: Knowledge distillation: A survey. *International Journal of Computer Vision* **129**(6), 1789–1819 (2021)
- [40] Demvsar, J.: Statistical comparisons of classifiers over multiple data sets. *The Journal of Machine learning research* **7**, 1–30 (2006)
- [41] Maier-Hein, L., Eisenmann, M., Reinke, A., Onogur, S., Stankovic, M., Scholz, P., Arbel, T., Bogunovic, H., Bradley, A.P., Carass, A., *et al.*: Why rankings of biomedical image analysis competitions should be interpreted with care. *Nature communications* **9**(1), 5217 (2018)
- [42] Antonelli, M., Reinke, A., Bakas, S., Farahani, K., Kopp-Schneider, A., Landman, B.A., Litjens, G., Menze, B., Ronneberger, O., Summers, R.M., *et al.*: The medical segmentation decathlon. *Nature communications* **13**(1), 4128 (2022)
- [43] Ilse, M., Tomczak, J., Welling, M.: Attention-based deep multiple instance learning. In: *International Conference on Machine Learning*, pp. 2127–2136 (2018). PMLR
- [44] Brancati, N., Anniciello, A.M., Pati, P., Riccio, D., Scognamiglio, G., Jaume, G., De Pietro, G., Di Bonito, M., Foncubierta, A., Botti, G., *et al.*: Bracs: A dataset for breast carcinoma subtyping in h&e histology images. *Database* **2022**, 093 (2022)
- [45] Weinstein, J.N., Collisson, E.A., Mills, G.B., Shaw, K.R., Ozenberger, B.A., Ellrott, K., Shmulevich, I., Sander, C., Stuart, J.M.: The cancer genome atlas pan-cancer analysis project. *Nature genetics* **45**(10), 1113–1120 (2013)
- [46] Bejnordi, B.E., Veta, M., Van Diest, P.J., Van Ginneken, B., Karssemeijer, N., Litjens, G., Van Der Laak, J.A., Hermsen, M., Manson, Q.F., Balkenhol, M., *et al.*: Diagnostic assessment of deep learning algorithms for detection of lymph node metastases in women with breast cancer. *Jama* **318**(22), 2199–2210 (2017)
- [47] Bandi, P., Geessink, O., Manson, Q., Van Dijk, M., Balkenhol, M., Hermsen, M., Bejnordi, B.E., Lee, B., Paeng, K., Zhong, A., *et al.*: From detection of individual metastases to classification of lymph node status at the patient level: the camelyon17 challenge. *IEEE transactions on medical imaging* **38**(2), 550–560 (2018)
- [48] Bulten, W., Kartasalo, K., Chen, P.-H.C.,

- Ström, P., Pinckaers, H., Nagpal, K., Cai, Y., Steiner, D.F., Van Boven, H., Vink, R., *et al.*: Artificial intelligence for diagnosis and gleason grading of prostate cancer: the panda challenge. *Nature medicine* **28**(1), 154–163 (2022)
- [49] Asadi-Aghbolaghi, M., Farahani, H., Zhang, A., Akbari, A., Kim, S., Chow, A., Dane, S., Consortium, O.C., Consortium, O., G Huntsman, D., *et al.*: Machine learning-driven histotype diagnosis of ovarian carcinoma: Insights from the ocean ai challenge. medRxiv, 2024–04 (2024)
- [50] Roetzer-Pejrimovsky, T., Moser, A.-C., Atli, B., Vogel, C.C., Mercea, P.A., Prihoda, R., Gelpi, E., Haberler, C., Höftberger, R., Hainfellner, J.A., *et al.*: The digital brain tumour atlas, an open histopathology resource. *Scientific Data* **9**(1), 55 (2022)
- [51] Wang, P., Li, Y., Reddy, C.K.: Machine learning for survival analysis: A survey. *ACM Computing Surveys (CSUR)* **51**(6), 1–36 (2019)
- [52] Xu, Y., Chen, H.: Multimodal optimal transport-based co-attention transformer with global structure consistency for survival prediction. In: *Proceedings of the IEEE/CVF International Conference on Computer Vision*, pp. 21241–21251 (2023)
- [53] Zhang, Y., Xu, Y., Chen, J., Xie, F., Chen, H.: Prototypical information bottlenecking and disentangling for multimodal cancer survival prediction. *International Conference on Learning Representations (ICLR)* (2024)
- [54] Zhou, F., Chen, H.: Cross-modal translation and alignment for survival analysis. In: *Proceedings of the IEEE/CVF International Conference on Computer Vision*, pp. 21485–21494 (2023)
- [55] Wiegrebe, S., Kopper, P., Sonabend, R., Bischl, B., Bender, A.: Deep learning for survival analysis: a review. *Artificial Intelligence Review* **57**(3), 65 (2024)
- [56] Oquab, M., Darcet, T., Moutakanni, T., Vo, H., Szafraniec, M., Khalidov, V., Fernandez, P., Haziza, D., Massa, F., El-Nouby, A., *et al.*: Dinov2: Learning robust visual features without supervision. *Transactions on Machine Learning Research (TMLR)* (2024)
- [57] Wang, X., Du, Y., Yang, S., Zhang, J., Wang, M., Zhang, J., Yang, W., Huang, J., Han, X.: Retecl: Clustering-guided contrastive learning for whole-slide image retrieval. *Medical image analysis* **83**, 102645 (2023)
- [58] Alizadeh, S.M., Helfroush, M.S., Müller, H.: A novel siamese deep hashing model for histopathology image retrieval. *Expert Systems with Applications* **225**, 120169 (2023)
- [59] Kalra, S., Tizhoosh, H.R., Shah, S., Choi, C., Damaskinos, S., Safarpour, A., Shafiei, S., Babaie, M., Diamandis, P., Campbell, C.J., *et al.*: Pan-cancer diagnostic consensus through searching archival histopathology images using artificial intelligence. *NPJ digital medicine* **3**(1), 31 (2020)
- [60] Kather, J.N., Krisam, J., Charoentong, P., Luedde, T., Herpel, E., Weis, C.-A., Gaiser, T., Marx, A., Valous, N.A., Ferber, D., *et al.*: Predicting survival from colorectal cancer histology slides using deep learning: A retrospective multicenter study. *PLoS medicine* **16**(1), 1002730 (2019)
- [61] Maaten, L., Hinton, G.: Visualizing data using t-sne. *Journal of machine learning research* **9**(11) (2008)
- [62] He, X., Zhang, Y., Mou, L., Xing, E., Xie, P.: Pathvqa: 30000+ questions for medical visual question answering. arXiv preprint arXiv:2003.10286 (2020)
- [63] Guo, Z., Ma, J., Xu, Y., Wang, Y., Wang, L., Chen, H.: Histgen: Histopathology report generation via local-global feature encoding and cross-modal context interaction. arXiv preprint arXiv:2403.05396 (2024)
- [64] Guevara, B.C., Marini, N., Marchesin, S.,

- Aswolinskiy, W., Schlimbach, R.-J., Podareanu, D., Ciompi, F.: Caption generation from histopathology whole-slide images using pre-trained transformers. In: Medical Imaging with Deep Learning, Short Paper Track (2023)
- [65] Chen, P., Li, H., Zhu, C., Zheng, S., Shui, Z., Yang, L.: Wscaption: Multiple instance generation of pathology reports for gigapixel whole-slide images. (2023)
- [66] Xu, H., Usuyama, N., Bagga, J., Zhang, S., Rao, R., Naumann, T., Wong, C., Gero, Z., González, J., Gu, Y., et al.: A whole-slide foundation model for digital pathology from real-world data. *Nature*, 1–8 (2024)
- [67] Ding, J., Ma, S., Dong, L., Zhang, X., Huang, S., Wang, W., Zheng, N., Wei, F.: Longnet: Scaling transformers to 1,000,000,000 tokens. *arXiv preprint arXiv:2307.02486* (2023)
- [68] Dao, T., Gu, A.: Transformers are SSMs: Generalized models and efficient algorithms through structured state space duality. In: International Conference on Machine Learning (ICML) (2024)
- [69] Yang, S., Wang, Y., Chen, H.: Mamamil: Enhancing long sequence modeling with sequence reordering in computational pathology. *arXiv preprint arXiv:2403.06800* (2024)
- [70] Goode, A., Gilbert, B., Harkes, J., Jukic, D., Satyanarayanan, M.: Openslide: A vendor-neutral software foundation for digital pathology. *Journal of pathology informatics* **4**(1), 27 (2013)
- [71] Lu, M.Y., Williamson, D.F., Chen, T.Y., Chen, R.J., Barbieri, M., Mahmood, F.: Data-efficient and weakly supervised computational pathology on whole-slide images. *Nature biomedical engineering* **5**(6), 555–570 (2021)
- [72] Zhou, J., Wei, C., Wang, H., Shen, W., Xie, C., Yuille, A., Kong, T.: ibot: Image bert pre-training with online tokenizer. International Conference on Learning Representations (ICLR) (2022)
- [73] He, K., Chen, X., Xie, S., Li, Y., Dollár, P., Girshick, R.: Masked autoencoders are scalable vision learners. In: Proceedings of the IEEE/CVF Conference on Computer Vision and Pattern Recognition, pp. 16000–16009 (2022)
- [74] Zhang, H., Li, F., Liu, S., Zhang, L., Su, H., Zhu, J., Ni, L.M., Shum, H.-Y.: DINO: DETR with Improved DeNoising Anchor Boxes for End-to-End Object Detection (2022)
- [75] Ranzinger, M., Heinrich, G., Kautz, J., Molchanov, P.: Am-radio: Agglomerative visual foundation model – reduce all domains into one. In: CVPR (2024)
- [76] He, K., Zhang, X., Ren, S., Sun, J.: Deep residual learning for image recognition. In: Proceedings of the IEEE Conference on Computer Vision and Pattern Recognition, pp. 770–778 (2016)
- [77] Deng, J., Dong, W., Socher, R., Li, L.-J., Li, K., Fei-Fei, L.: Imagenet: A large-scale hierarchical image database. In: 2009 IEEE Conference on Computer Vision and Pattern Recognition, pp. 248–255 (2009)
- [78] Shao, Z., Bian, H., Chen, Y., Wang, Y., Zhang, J., Ji, X., et al.: Transmil: Transformer based correlated multiple instance learning for whole slide image classification. *Advances in neural information processing systems* **34**, 2136–2147 (2021)
- [79] Edwards, N.J., Oberti, M., Thangudu, R.R., Cai, S., McGarvey, P.B., Jacob, S., Madhavan, S., Ketchum, K.A.: The cptac data portal: a resource for cancer proteomics research. *Journal of proteome research* **14**(6), 2707–2713 (2015)
- [80] Farahani, H., Boschman, J., Farnell, D., Darbandsari, A., Zhang, A., Ahmadvand, P., Jones, S.J., Huntsman, D., Köbel,



- M., Gilks, C.B., *et al.*: Deep learning-based histotype diagnosis of ovarian carcinoma whole-slide pathology images. *Modern Pathology* **35**(12), 1983–1990 (2022)
- [81] Kundra, R., Zhang, H., Sheridan, R., Sirintrapun, S.J., Wang, A., Ochoa, A., Wilson, M., Gross, B., Sun, Y., Madupuri, R., *et al.*: Oncotree: a cancer classification system for precision oncology. *JCO clinical cancer informatics* **5**, 221–230 (2021)
- [82] Chen, R.J., Lu, M.Y., Shaban, M., Chen, C., Chen, T.Y., Williamson, D.F., Mahmood, F.: Whole slide images are 2d point clouds: Context-aware survival prediction using patch-based graph convolutional networks. In: *Medical Image Computing and Computer Assisted Intervention–MICCAI 2021: 24th International Conference, Strasbourg, France, September 27–October 1, 2021, Proceedings, Part VIII 24*, pp. 339–349 (2021). Springer
- [83] Zadeh, S.G., Schmid, M.: Bias in cross-entropy-based training of deep survival networks. *IEEE transactions on pattern analysis and machine intelligence* **43**(9), 3126–3137 (2020)
- [84] Balestrieri, R., Ibrahim, M., Sobal, V., Morcos, A., Shekhar, S., Goldstein, T., Bordes, F., Bardes, A., Mialon, G., Tian, Y., *et al.*: A cookbook of self-supervised learning. *arXiv preprint arXiv:2304.12210* (2023)
- [85] Loshchilov, I., Hutter, F.: Decoupled weight decay regularization. *International Conference on Learning Representations (ICLR)* (2019)
- [86] Loshchilov, I., Hutter, F.: Sgdr: Stochastic gradient descent with warm restarts. *International Conference on Learning Representations (ICLR)* (2017)
- [87] Detlefsen, N.S., Borovec, J., Schock, J., Jha, A.H., Koker, T., Di Liello, L., Stancl, D., Quan, C., Grechkin, M., Falcon, W.: Torchmetrics-measuring reproducibility in pytorch. *Journal of Open Source Software* **7**(70), 4101 (2022)
- [88] Brummer, O., Pölönen, P., Mustjoki, S., Brück, O.: Computational textural mapping harmonises sampling variation and reveals multidimensional histopathological fingerprints. *British Journal of Cancer* **129**(4), 683–695 (2023)
- [89] Aresta, G., Araújo, T., Kwok, S., Chennamsetty, S.S., Safwan, M., Alex, V., Marami, B., Prastawa, M., Chan, M., Donovan, M., *et al.*: Bach: Grand challenge on breast cancer histology images. *Medical image analysis* **56**, 122–139 (2019)
- [90] Barbano, C.A., Perlo, D., Tartaglione, E., Fiandrotti, A., Bertero, L., Cassoni, P., Grangetto, M.: Unitopatho, a labeled histopathological dataset for colorectal polyps classification and adenoma dysplasia grading. In: *2021 IEEE International Conference on Image Processing (ICIP)*, pp. 76–80 (2021)
- [91] Kather, J.N., Pearson, A.T., Halama, N., Jäger, D., Krause, J., Loosen, S.H., Marx, A., Boor, P., Tacke, F., Neumann, U.P., *et al.*: Deep learning can predict microsatellite instability directly from histology in gastrointestinal cancer. *Nature medicine* **25**(7), 1054–1056 (2019)
- [92] Komura, D., Kawabe, A., Fukuta, K., Sano, K., Umezaki, T., Koda, H., Suzuki, R., Tominaga, K., Ochi, M., Konishi, H., *et al.*: Universal encoding of pan-cancer histology by deep texture representations. *Cell Reports* **38**(9) (2022)
- [93] Abousamra, S., Gupta, R., Hou, L., Batiste, R., Zhao, T., Shankar, A., Rao, A., Chen, C., Samaras, D., Kurc, T., *et al.*: Deep learning-based mapping of tumor infiltrating lymphocytes in whole slide images of 23 types of cancer. *Frontiers in oncology* **11**, 806603 (2022)
- [94] Saltz, J., Gupta, R., Hou, L., Kurc, T., Singh, P., Nguyen, V., Samaras, D., Shroyer, K.R., Zhao, T., Batiste, R., *et al.*: Spatial organization and molecular correlation of tumor-infiltrating lymphocytes using deep learning on pathology images. *Cell reports*

- 23**(1), 181–193 (2018)
- [95] Tolkach, Y., Wolgast, L.M., Damanakis, A., Pryalukhin, A., Schallenberg, S., Hulla, W., Eich, M.-L., Schroeder, W., Mukhopadhyay, A., Fuchs, M., *et al.*: Artificial intelligence for tumour tissue detection and histological regression grading in oesophageal adenocarcinomas: a retrospective algorithm development and validation study. *The Lancet Digital Health* **5**(5), 265–275 (2023)
- [96] Veeling, B.S., Linmans, J., Winkens, J., Cohen, T., Welling, M.: Rotation equivariant cnns for digital pathology. In: *Medical Image Computing and Computer Assisted Intervention—MICCAI 2018: 21st International Conference, Granada, Spain, September 16–20, 2018, Proceedings, Part II 11*, pp. 210–218 (2018)
- [97] Han, C., Pan, X., Yan, L., Lin, H., Li, B., Yao, S., Lv, S., Shi, Z., Mai, J., Lin, J., *et al.*: Wsss4luad: Grand challenge on weakly-supervised tissue semantic segmentation for lung adenocarcinoma. arXiv preprint arXiv:2204.06455 (2022)
- [98] Han, C., Lin, J., Mai, J., Wang, Y., Zhang, Q., Zhao, B., Chen, X., Pan, X., Shi, Z., Xu, Z., Yao, S., Yan, L., Lin, H., Huang, X., Liang, C., Han, G., Liu, Z.: Multi-layer pseudo-supervision for histopathology tissue semantic segmentation using patch-level classification labels. *Medical Image Analysis*, 102487 (2022)
- [99] Spanhol, F.A., Oliveira, L.S., Petitjean, C., Heutte, L.: A dataset for breast cancer histopathological image classification. *Ieee transactions on biomedical engineering* **63**(7), 1455–1462 (2015)
- [100] Zhu, C., Chen, W., Peng, T., Wang, Y., Jin, M.: Hard sample aware noise robust learning for histopathology image classification. *IEEE transactions on medical imaging* **41**(4), 881–894 (2021)
- [101] Aksoy, S., Haralick, R.M.: Probabilistic vs. geometric similarity measures for image retrieval. In: *Proceedings IEEE Conference on Computer Vision and Pattern Recognition. CVPR 2000*, vol. 2, pp. 357–362 (2000). IEEE
- [102] Li, P., Liu, G., He, J., Zhao, Z., Zhong, S.: Masked vision and language pre-training with unimodal and multimodal contrastive losses for medical visual question answering. In: *International Conference on Medical Image Computing and Computer-Assisted Intervention*, pp. 374–383 (2023). Springer
- [103] Gong, H., Chen, G., Mao, M., Li, Z., Li, G.: Vqamix: Conditional triplet mixup for medical visual question answering. *IEEE Transactions on Medical Imaging* **41**(11), 3332–3343 (2022)
- [104] Chen, Z., Shen, Y., Song, Y., Wan, X.: Cross-modal memory networks for radiology report generation. In: Zong, C., Xia, F., Li, W., Navigli, R. (eds.) *Proceedings of the 59th Annual Meeting of the Association for Computational Linguistics and the 11th International Joint Conference on Natural Language Processing (Volume 1: Long Papers)*, pp. 5904–5914. Association for Computational Linguistics, Online (2021)
- [105] Chen, Z., Song, Y., Chang, T.-H., Wan, X.: Generating radiology reports via memory-driven transformer. In: Webber, B., Cohn, T., He, Y., Liu, Y. (eds.) *Proceedings of the 2020 Conference on Empirical Methods in Natural Language Processing (EMNLP)*, pp. 1439–1449. Association for Computational Linguistics, Online (2020)
- [106] Li, M., Cai, W., Verspoor, K., Pan, S., Liang, X., Chang, X.: Cross-modal clinical graph transformer for ophthalmic report generation. In: *Proceedings of the IEEE/CVF Conference on Computer Vision and Pattern Recognition*, pp. 20656–20665 (2022)
- [107] Papineni, K., Roukos, S., Ward, T., Zhu, W.-J.: Bleu: a method for automatic evaluation of machine translation. In: *Proceedings of the 40th Annual Meeting of the Association for Computational Linguistics*, pp.

- 311–318 (2002)
- [108] Denkowski, M., Lavie, A.: Meteor 1.3: Automatic metric for reliable optimization and evaluation of machine translation systems. In: Proceedings of the Sixth Workshop on Statistical Machine Translation, pp. 85–91 (2011)
- [109] Lin, C.-Y.: Rouge: A package for automatic evaluation of summaries. In: Text Summarization Branches Out, pp. 74–81 (2004)
- [110] Paszke, A., Gross, S., Massa, F., Lerer, A., Bradbury, J., Chanan, G., Killeen, T., Lin, Z., Gimelshein, N., Antiga, L., et al.: Pytorch: An imperative style, high-performance deep learning library. *Advances in neural information processing systems* **32** (2019)
- [111] Pedregosa, F., Varoquaux, G., Gramfort, A., Michel, V., Thirion, B., Grisel, O., Blondel, M., Prettenhofer, P., Weiss, R., Dubourg, V., et al.: Scikit-learn: Machine learning in python. *the Journal of machine Learning research* **12**, 2825–2830 (2011)
- [112] Chen, X., Xie, S., He, K.: An empirical study of training self-supervised vision transformers. In: Proceedings of the IEEE/CVF International Conference on Computer Vision, pp. 9640–9649 (2021)
- [113] Radford, A., Kim, J.W., Hallacy, C., Ramesh, A., Goh, G., Agarwal, S., Sastry, G., Askell, A., Mishkin, P., Clark, J., et al.: Learning transferable visual models from natural language supervision. In: International Conference on Machine Learning, pp. 8748–8763 (2021)
- [114] Yu, J., Wang, Z., Vasudevan, V., Yeung, L., Seyedhosseini, M., Wu, Y.: Coca: Contrastive captioners are image-text foundation models. *Transactions on Machine Learning Research (TMLR)* (2023)
- [115] Wilkinson, S., Ye, H., Karzai, F., Harmon, S.A., Terrigino, N.T., VanderWeele, D.J., Bright, J.R., Atway, R., Trostel, S.Y., Carrabba, N.V., et al.: Nascent prostate cancer heterogeneity drives evolution and resistance to intense hormonal therapy. *European urology* **80**(6), 746–757 (2021)
- [116] Xu, F., Zhu, C., Tang, W., Wang, Y., Zhang, Y., Li, J., Jiang, H., Shi, Z., Liu, J., Jin, M.: Predicting axillary lymph node metastasis in early breast cancer using deep learning on primary tumor biopsy slides. *Frontiers in oncology* **11**, 759007 (2021)
- [117] Shephard, A., Jahanifar, M., Wang, R., Dawood, M., Graham, S., Sidlauskas, K., Khurram, S.A., Rajpoot, N., Raza, S.E.A.: Tiager: Tumor-infiltrating lymphocyte scoring in breast cancer for the tiger challenge. *arXiv preprint arXiv:2206.11943* (2022)
- [118] Aubreville, M., Stathonikos, N., Donovan, T.A., Klopffleisch, R., Ammeling, J., Ganz, J., Wilm, F., Veta, M., Jabari, S., Eckstein, M., et al.: Domain generalization across tumor types, laboratories, and species—insights from the 2022 edition of the mitosis domain generalization challenge. *Medical Image Analysis* **94**, 103155 (2024)
- [119] Huo, X., Ong, K.H., Lau, K.W., Gole, L., Young, D.M., Tan, C.L., Zhu, X., Zhang, C., Zhang, Y., Li, L., et al.: A comprehensive ai model development framework for consistent gleason grading. *Communications Medicine* **4**(1), 84 (2024)
- [120] Wang, C.-W., Chang, C.-C., Lee, Y.-C., Lin, Y.-J., Lo, S.-C., Hsu, P.-C., Liou, Y.-A., Wang, C.-H., Chao, T.-K.: Weakly supervised deep learning for prediction of treatment effectiveness on ovarian cancer from histopathology images. *Computerized Medical Imaging and Graphics* **99**, 102093 (2022)
- [121] Wang, C.-W., Chang, C.-C., Khalil, M.A., Lin, Y.-J., Liou, Y.-A., Hsu, P.-C., Lee, Y.-C., Wang, C.-H., Chao, T.-K.: Histopathological whole slide image dataset for classification of treatment effectiveness to ovarian cancer. *Scientific Data* **9**(1), 25 (2022)
- [122] Weitz, P., Valkonen, M., Solorzano, L., Carr, C., Kartasalo, K., Boissin, C., Koivukoski,

- S., Kuusela, A., Rasic, D., Feng, Y., *et al.*: A multi-stain breast cancer histological whole-slide-image data set from routine diagnostics. *Scientific Data* **10**(1), 562 (2023)
- [123] Matek, C., Schwarz, S., Marr, C., Spiekermann, K.: A single-cell morphological dataset of leukocytes from aml patients and non-malignant controls (aml-cytomorphology\_lmu). *The Cancer Imaging Archive (TCIA)*[Internet] (2019)
- [124] Gamper, J., Rajpoot, N.: Multiple instance captioning: Learning representations from histopathology textbooks and articles. In: *Proceedings of the IEEE/CVF Conference on Computer Vision and Pattern Recognition*, pp. 16549–16559 (2021)
- [125] Xu, G., Song, Z., Sun, Z., Ku, C., Yang, Z., Liu, C., Wang, S., Ma, J., Xu, W.: Camel: A weakly supervised learning framework for histopathology image segmentation. In: *Proceedings of the IEEE/CVF International Conference on Computer Vision*, pp. 10682–10691 (2019)
- [126] Koziarski, M., Cyganek, B., Niedziela, P., Olborski, B., Antosz, Z., Żydak, M., Kwolek, B., Wąsowicz, P., Bukala, A., Swadźba, J., *et al.*: Diagset: a dataset for prostate cancer histopathological image classification. *Scientific Reports* **14**(1), 6780 (2024)
- [127] Vrabac, D., Smit, A., Rojansky, R., Natkunam, Y., Advani, R.H., Ng, A.Y., Fernandez-Pol, S., Rajpurkar, P.: DLBCL-Morph: Morphological features computed using deep learning for an annotated digital DLBCL image set (2020)
- [128] Carithers, L.J., Ardlie, K., Barcus, M., Branton, P.A., Britton, A., Buia, S.A., Compton, C.C., DeLuca, D.S., Peter-Demchok, J., Gelfand, E.T., *et al.*: A novel approach to high-quality postmortem tissue procurement: the gtex project. *Biopreservation and biobanking* **13**(5), 311–319 (2015)
- [129] Pataki, B.Á., Olar, A., Ribli, D., Pesti, A., Kontsek, E., Gyöngyösi, B., Bilecz, Á., Kovács, T., Kovács, K.A., Kramer, Z., *et al.*: Huncrc: annotated pathological slides to enhance deep learning applications in colorectal cancer screening. *Scientific Data* **9**(1), 370 (2022)
- [130] Janowczyk, A., Madabhushi, A.: Deep learning for digital pathology image analysis: A comprehensive tutorial with selected use cases. *Journal of pathology informatics* **7**(1), 29 (2016)
- [131] Borkowski, A.A., Bui, M.M., Thomas, L.B., Wilson, C.P., DeLand, L.A., Mastorides, S.M.: Lung and colon cancer histopathological image dataset (lc25000). *arXiv preprint arXiv:1912.12142* (2019)
- [132] Ryu, J., Puche, A.V., Shin, J., Park, S., Brattoli, B., Lee, J., Jung, W., Cho, S.I., Paeng, K., Ock, C.-Y., *et al.*: Ocelot: Overlapped cell on tissue dataset for histopathology. In: *Proceedings of the IEEE/CVF Conference on Computer Vision and Pattern Recognition*, pp. 23902–23912 (2023)
- [133] Leavey, P., Sengupta, A., Rakheja, D., Daescu, O., Arunachalam, H., Mishra, R.: Osteosarcoma data from ut southwestern/ut dallas for viable and necrotic tumor assessment [data set]. *Cancer Imaging Arch* **14** (2019)
- [134] Kim, Y.J., Jang, H., Lee, K., Park, S., Min, S.-G., Hong, C., Park, J.H., Lee, K., Kim, J., Hong, W., *et al.*: Paip 2019: Liver cancer segmentation challenge. *Medical image analysis* **67**, 101854 (2021)
- [135] Kim, K., Lee, K., Cho, S., Kang, D.U., Park, S., Kang, Y., Kim, H., Choe, G., Moon, K.C., Lee, K.S., *et al.*: Paip 2020: Microsatellite instability prediction in colorectal cancer. *Medical Image Analysis* **89**, 102886 (2023)
- [136] Tafavvoghi, M., Bongo, L.A., Shvetsov, N., Busund, L.-T.R., Møllersen, K.: Publicly available datasets of breast histopathology h&e whole-slide images: A scoping review. *Journal of Pathology Informatics*, 100363

(2024)

- [137] Silva-Rodríguez, J., Colomer, A., Sales, M.A., Molina, R., Naranjo, V.: Going deeper through the gleason scoring scale: An automatic end-to-end system for histology prostate grading and cribriform pattern detection. *Computer methods and programs in biomedicine* **195**, 105637 (2020)
- [138] Kemaloglu, N., Aydoğan, T., Küçüksille, E.U.: 3 deep learning approaches in metastatic breast cancer detection. *Artificial Intelligence for Data-Driven Medical Diagnosis* **3**, 55 (3)
- [139] Petrick, N., Akbar, S., Cha, K.H., Nofech-Mozes, S., Sahiner, B., Gavrielides, M.A., Kalpathy-Cramer, J., Drukker, K., Martel, A.L., BreastPathQ Challenge Group, f.t.: Spie-aapm-nci breastpathq challenge: an image analysis challenge for quantitative tumor cellularity assessment in breast cancer histology images following neoadjuvant treatment. *Journal of Medical Imaging* **8**(3), 034501–034501 (2021)
- [140] Veta, M., Heng, Y.J., Stathonikos, N., Bejnordi, B.E., Beca, F., Wollmann, T., Rohr, K., Shah, M.A., Wang, D., Rousson, M., *et al.*: Predicting breast tumor proliferation from whole-slide images: the tupac16 challenge. *Medical image analysis* **54**, 111–121 (2019)
- [141] Zhu, M., Ren, B., Richards, R., Suriawinata, M., Tomita, N., Hassanpour, S.: Development and evaluation of a deep neural network for histologic classification of renal cell carcinoma on biopsy and surgical resection slides. *Scientific reports* **11**(1), 7080 (2021)

## Appendix A Extended Data

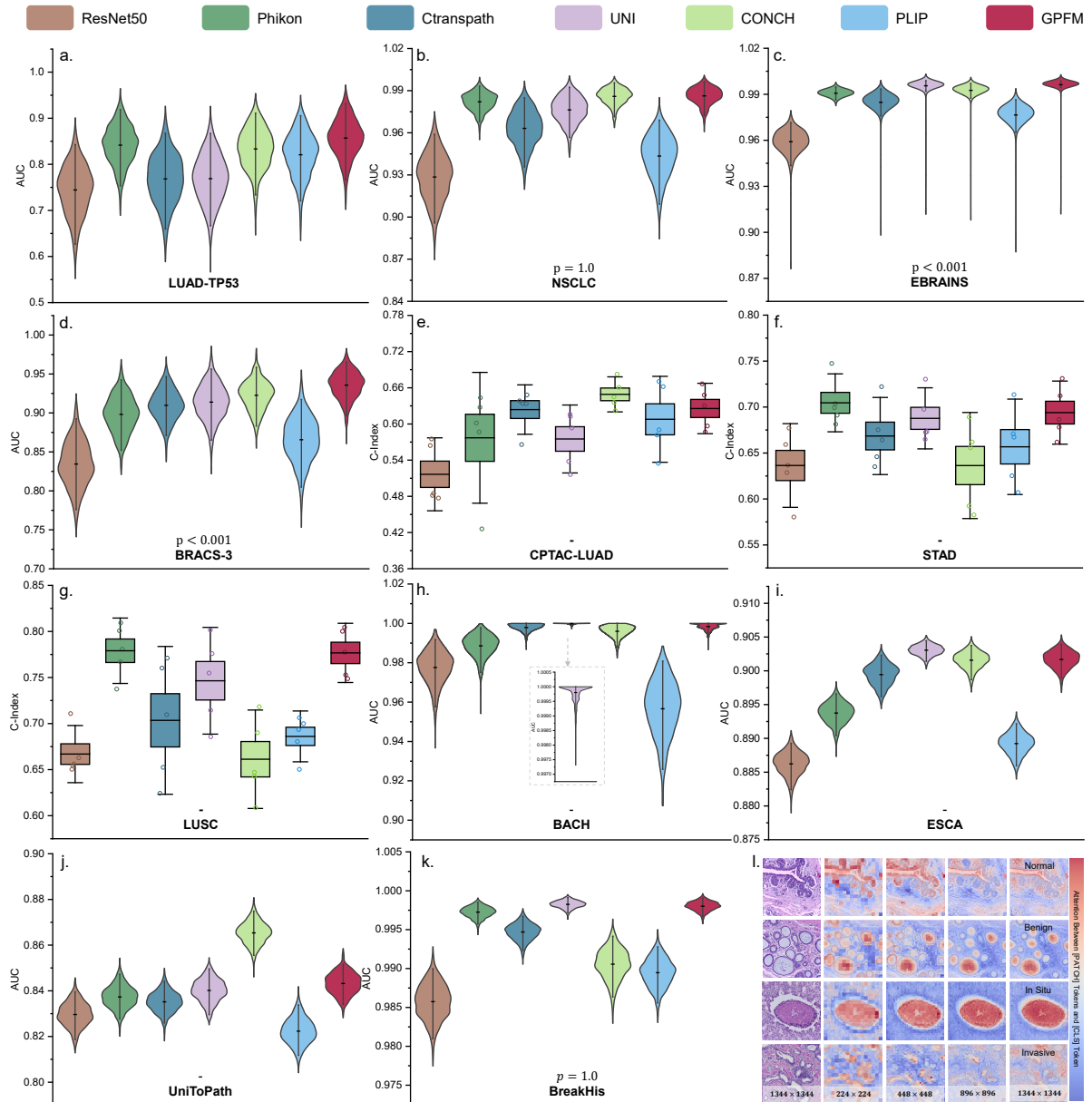


**Fig. A1 Overview of visualized results.** **a.** The 5 fold RCC classification results on DHMC dataset. **b-d.** The results of NSCLC subtyping, brain tumor classification, and coarse-grained breast cancer classification. **e-g.** The survival analysis results on CPTAC-LUAD, STAD (TCGA), and LUSC (TCGA) datasets. **h-k.** The results of tissue classification including breast cancer classification on BACH (4 classes) and breakHis (2 classes), esophageal carcinoma subtyping on ESCA, CRC polyp classification on UniToPath. **l.** Attention heatmap of GPFM across various image resolutions for BRCA subtyping in BACH dataset. The colored squares represent the 14x14 [PATCH] tokens encoded by the GPFM model. The heatmap values indicate the similarity between each [PATCH] token and the [CLS] token generated by the last layer of GPFM, measured using Euclidean distance. The consistent attention patterns observed across varying image resolutions and tissue types underscore the robust capabilities of the GPFM model.

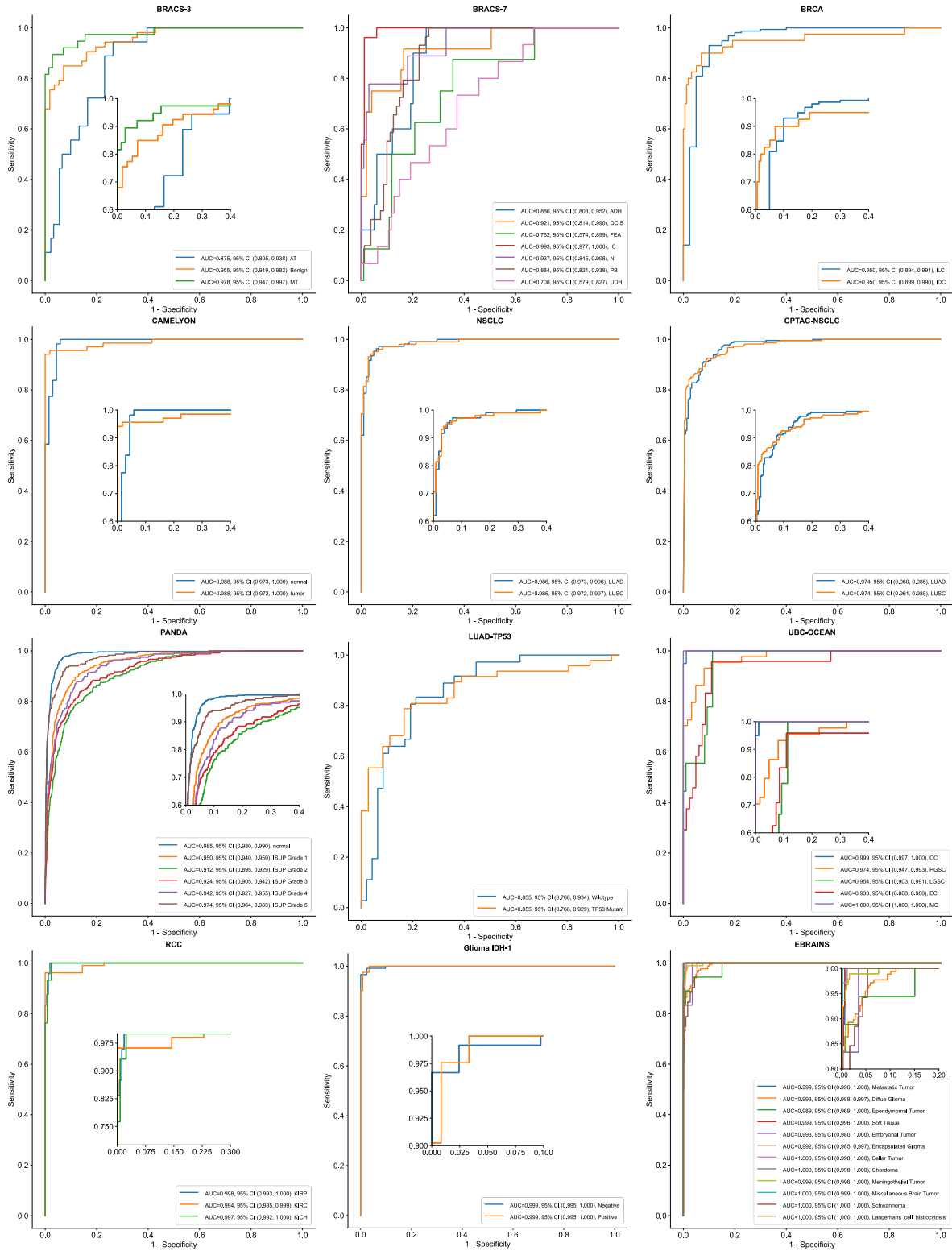


Fig. A2 ROC curves of GPFM across 12 WSI Classification Tasks.

**Table A1 The Overall Performance of Different Foundation models across 39 Tasks.** AUC is used to evaluate WSI classification and ROI classification. C-index is used to measure the performance of survival analysis tasks. Overall accuracy (Closed and Open accuracy) is used to evaluate the VQA task. The average accuracy (ACC@1, ACC@3, and ACC@5) is adopted to measure image-to-image retrieval task. The average value of six metrics (BELU-1, BELU-2, BELU-3, BELU-4, METEOR, and ROUGE-L) is adopted to measure the performance of report generation.

Dataset	ResNet50	Phikon	Ctran.	UNI	CONCH	PLIP	GPFM
BRACS-3	0.835	0.898	0.908	0.913	<u>0.923</u>	0.866	<b>0.936</b>
Camelyon	0.922	0.967	0.957	<u>0.987</u>	0.965	0.929	<b>0.988</b>
BRACS-7	0.772	0.818	<u>0.857</u>	0.855	0.841	0.814	<b>0.871</b>
BRCA	0.846	0.936	0.931	<u>0.946</u>	0.944	0.893	<b>0.950</b>
UBC-OCEAN	0.919	0.966	0.960	<u>0.969</u>	0.957	0.946	<b>0.972</b>
RCC	0.963	<u>0.995</u>	0.981	0.982	0.988	0.980	<b>0.996</b>
NSCLC	0.929	<u>0.982</u>	0.963	0.977	<b>0.986</b>	0.942	<b>0.986</b>
CPTAC-NSCLC	0.937	<u>0.967</u>	0.965	0.960	0.961	0.939	<b>0.974</b>
PANDA	0.884	0.943	0.925	<u>0.944</u>	0.921	0.903	<b>0.948</b>
LUAD TP53	0.742	<u>0.841</u>	0.770	0.766	0.836	0.821	<b>0.855</b>
Glioma IDH-1	0.945	0.990	0.974	<u>0.996</u>	0.995	0.974	<b>0.998</b>
EBRAINS	0.959	0.990	0.985	<b>0.996</b>	<u>0.992</u>	0.977	<b>0.996</b>
BRCA	0.678	<b>0.770</b>	0.704	0.722	0.677	0.691	<u>0.757</u>
BLCA	0.696	<u>0.692</u>	0.670	0.690	0.644	0.665	<b>0.711</b>
KIRC	0.634	<b>0.708</b>	0.671	0.674	0.659	0.652	<u>0.697</u>
KIRP	0.630	<u>0.680</u>	0.649	0.659	0.623	0.674	<b>0.688</b>
LUAD	0.646	<u>0.738</u>	0.633	0.673	0.641	0.628	<b>0.739</b>
STAD	0.636	<b>0.705</b>	0.669	0.688	0.636	0.657	<u>0.694</u>
LUSC	0.667	<b>0.779</b>	0.703	0.746	0.661	0.686	<u>0.777</u>
COADREAD		<u>0.707</u>	0.680	0.691	0.679	0.653	<b>0.708</b>
GBMLGG	0.724	0.760	0.745	<u>0.778</u>	0.735	0.738	<b>0.785</b>
LUAD-CPTAC	0.517	0.577	0.624	<u>0.575</u>	<b>0.649</b>	0.608	<u>0.626</u>
CESC	0.611	<u>0.747</u>	0.702	0.735	0.677	0.694	<b>0.754</b>
SKCM	0.699	<u>0.773</u>	0.743	0.747	0.721	0.709	<b>0.777</b>
CRC-100K	0.983	<u>0.993</u>	<b>0.995</b>	0.991	<u>0.993</u>	0.990	<b>0.995</b>
CRC-MSI	0.706	0.772	0.802	0.797	<u>0.810</u>	0.691	<b>0.812</b>
PCAM	0.926	0.969	0.940	<u>0.982</u>	0.965	0.943	<b>0.988</b>
BACH	0.977	0.988	0.998	<b>1.000</b>	0.996	0.959	<u>0.998</u>
CCRCC-TCGA-HEL	0.993	<b>0.997</b>	0.994	<u>0.996</u>	0.994	0.992	<b>0.997</b>
ESCA	0.886	0.894	0.899	<b>0.903</b>	<u>0.902</u>	0.889	<u>0.902</u>
PanCancer-TIL	0.946	0.975	0.965	<u>0.977</u>	0.971	0.949	<b>0.978</b>
PanCancer-TCGA	0.975	<b>0.999</b>	0.992	<u>0.997</u>	0.991	0.978	<b>0.999</b>
UniToPath	0.830	0.838	0.836	0.840	<b>0.865</b>	0.823	<u>0.844</u>
chaoyang	0.930	<u>0.952</u>	0.950	<u>0.952</u>	0.942	0.941	<b>0.956</b>
WSSS4LUAD	0.989	<u>0.997</u>	<u>0.997</u>	<u>0.997</u>	0.995	0.994	<b>0.998</b>
BreakHis	0.986	<u>0.997</u>	0.995	<b>0.998</b>	0.991	0.989	<b>0.998</b>
PathVQA	0.574	<u>0.560</u>	0.603	<u>0.613</u>	<b>0.628</b>	0.594	<u>0.613</u>
Report Generation	0.123	<b>0.269</b>	0.134	0.235	0.149	0.137	<u>0.254</u>
Image Retrieval	0.892	0.938	0.883	<u>0.958</u>	0.943	0.874	<b>0.967</b>
Average Metric	0.798	<u>0.849</u>	0.830	0.844	0.832	0.815	<b>0.859</b>
Average Ranking	6.55	2.97	4.26	<u>2.96</u>	4.14	5.76	<b>1.36</b>
p-value	3.6e-12	1.7e-4	1.4e-7	3.0e-7	8.2e-6	3.6e-12	-



**Table A2 Average WSI classification performance of foundation models across 12 datasets.** The features have been pre-extracted, and the subsequent downstream tasks are conducted using ABMIL. Best performing model for each metric is **bolded** and second-best performing model is underlined. The standard deviation is included.

	Balanced ACC	Weighted F1	AUC
ResNet50	0.700±0.165	0.683±0.178	0.888±0.070
Phikon	0.804±0.158	0.801±0.176	0.941±0.057
Ctranspath	0.789±0.119	0.791±0.124	0.931±0.060
UNI	0.814±0.148	0.815±0.155	0.941±0.065
CONCH	0.803±0.152	0.800±0.167	0.942±0.052
PLIP	0.772±0.141	0.768±0.142	0.915±0.055
GPFM	0.833±0.142	0.834±0.150	0.956±0.046

**Table A3 NSCLC subtyping performance of different foundation models on TCGA-NSCLC dataset.** Non-parametric bootstrapping with 1,000 bootstrap replicates is employed for statistical analysis. The 95% CI is included in parentheses. Best performing model for each metric is **bolded** and second-best performing model is underlined.

	Balanced ACC	Weighted F1	AUC
ResNet50	0.845 (0.800-0.893)	0.842 (0.791-0.893)	0.929 (0.896-0.959)
Phikon	0.888 (0.845-0.928)	0.885 (0.843-0.924)	0.982 (0.968-0.993)
Ctranspath	0.894 (0.850-0.934)	0.895 (0.851-0.933)	0.963 (0.936-0.985)
UNI	0.928 (0.891-0.961)	0.928 (0.890-0.962)	0.977 (0.957-0.992)
CONCH	0.924 (0.888-0.957)	0.924 (0.881-0.957)	<b>0.986 (0.971-0.996)</b>
PLIP	0.865 (0.821-0.908)	0.865 (0.812-0.909)	0.942 (0.910-0.969)
GPFM	<b>0.948 (0.915-0.976)</b>	<b>0.947 (0.918-0.976)</b>	<b>0.986 (0.973-0.996)</b>

**Table A4 NSCLC subtyping performance of different foundation models on CPTAC-NSCLC dataset.** Non-parametric bootstrapping with 1,000 bootstrap replicates is employed for statistical analysis. The 95% CI is included in parentheses. Best performing model for each metric is **bolded** and second-best performing model is underlined.

	Balanced ACC	Weighted F1	AUC
ResNet50	0.847 (0.803-0.871)	0.847 (0.803-0.871)	0.937 (0.899-0.945)
Phikon	0.901 (0.873-0.928)	0.900 (0.880-0.925)	0.967 (0.951-0.980)
Ctranspath	0.887 (0.858-0.916)	0.887 (0.856-0.914)	0.965 (0.950-0.977)
UNI	<b>0.911 (0.883-0.937)</b>	<b>0.911 (0.884-0.939)</b>	0.960 (0.942-0.976)
CONCH	0.876 (0.844-0.903)	0.876 (0.844-0.905)	0.961 (0.944-0.975)
PLIP	0.841 (0.805-0.876)	0.841 (0.808-0.873)	0.939 (0.918-0.957)
GPFM	0.906 (0.877-0.932)	0.906 (0.880-0.934)	<b>0.974 (0.961-0.985)</b>

**Table A5 RCC subtyping performance of different foundation models on TCGA-RCC dataset.** Non-parametric bootstrapping with 1,000 bootstrap replicates is employed for statistical analysis. The 95% CI is included in parentheses. Best performing model for each metric is **bolded** and second-best performing model is underlined.

	Balanced ACC	Weighted F1	AUC
ResNet50	0.870 (0.805-0.926)	0.858 (0.797-0.910)	0.963 (0.937-0.983)
Phikon	<b>0.964 (0.936-0.987)</b>	<b>0.960 (0.937-0.982)</b>	0.995 (0.989-0.999)
Ctranspath	0.883 (0.820-0.938)	0.888 (0.833-0.939)	0.981 (0.965-0.992)
UNI	0.903 (0.847-0.954)	0.913 (0.862-0.957)	0.982 (0.966-0.995)
CONCH	0.941 (0.891-0.979)	0.937 (0.896-0.974)	0.988 (0.977-0.997)
PLIP	0.899 (0.845-0.947)	0.904 (0.853-0.948)	0.980 (0.963-0.993)
GPFM	0.925 (0.874-0.967)	0.930 (0.885-0.966)	<b>0.996 (0.992-0.999)</b>

**Table A6 The breast metastasis detection performance of different foundation models on CAMELYON dataset.** Non-parametric bootstrapping with 1,000 bootstrap replicates is employed for statistical analysis. The 95% CI is included in parentheses. Best performing model for each metric is **bolded** and second-best performing model is underlined.

	Balanced ACC	Weighted F1	AUC
ResNet50	0.855 (0.797-0.909)	0.857 (0.800-0.910)	0.922 (0.864-0.966)
Phikon	0.945 (0.900-0.979)	0.952 (0.918-0.982)	0.967 (0.932-0.993)
Ctranspath	0.898 (0.852-0.941)	0.908 (0.860-0.951)	0.957 (0.924-0.986)
UNI	<u>0.963 (0.930-0.992)</u>	<b>0.970 (0.940-0.994)</b>	<u>0.987 (0.969-0.998)</u>
CONCH	<u>0.936 (0.896-0.974)</u>	0.945 (0.910-0.977)	<u>0.965 (0.934-0.989)</u>
PLIP	0.882 (0.826-0.930)	0.890 (0.840-0.936)	0.929 (0.882-0.967)
GPFM	<b>0.964 (0.931-0.991)</b>	0.964 (0.932-0.988)	<b>0.988 (0.971-1.000)</b>

**Table A7 Lobular and ductal carcinoma subtyping performance of different foundation models on TCGA-BRCA dataset.** Non-parametric bootstrapping with 1,000 bootstrap replicates is employed for statistical analysis. The 95% CI is included in parentheses. Best performing model for each metric is **bolded** and second-best performing model is underlined.

	Balanced ACC	Weighted F1	AUC
ResNet50	0.658 (0.585-0.735)	0.691 (0.596-0.783)	0.846 (0.768-0.911)
Phikon	0.794 (0.718-0.865)	0.835 (0.751-0.901)	0.936 (0.887-0.977)
Ctranspath	0.843 (0.767-0.914)	0.859 (0.790-0.917)	0.931 (0.870-0.975)
UNI	<u>0.869 (0.797-0.929)</u>	<u>0.879 (0.810-0.932)</u>	<u>0.946 (0.894-0.987)</u>
CONCH	<u>0.835 (0.750-0.905)</u>	<u>0.875 (0.807-0.934)</u>	<u>0.944 (0.902-0.979)</u>
PLIP	0.823 (0.747-0.897)	0.820 (0.750-0.888)	0.893 (0.824-0.950)
GPFM	<b>0.881 (0.813-0.947)</b>	<b>0.907 (0.850-0.956)</b>	<b>0.950 (0.898-0.990)</b>

**Table A8 Coarse-grained breast carcinoma subtyping performance of different foundation models on BRACS dataset.** Non-parametric bootstrapping with 1,000 bootstrap replicates is employed for statistical analysis. The 95% CI is included in parentheses. Best performing model for each metric is **bolded** and second-best performing model is underlined.

	Balanced ACC	Weighted F1	AUC
ResNet50	0.568 (0.515-0.615)	0.522 (0.463-0.571)	0.835 (0.776-0.892)
Phikon	0.707 (0.621-0.797)	0.701 (0.602-0.800)	0.898 (0.852-0.942)
Ctranspath	0.674 (0.592-0.757)	0.664 (0.559-0.754)	0.908 (0.871-0.946)
UNI	<u>0.746 (0.660-0.840)</u>	<u>0.738 (0.640-0.824)</u>	<u>0.913 (0.865-0.956)</u>
CONCH	<u>0.677 (0.606-0.752)</u>	<u>0.668 (0.575-0.771)</u>	<u>0.923 (0.883-0.958)</u>
PLIP	0.679 (0.596-0.773)	0.676 (0.579-0.782)	<u>0.866 (0.805-0.917)</u>
GPFM	<b>0.749 (0.660-0.834)</b>	<b>0.758 (0.658-0.841)</b>	<b>0.936 (0.896-0.965)</b>

**Table A9 Fine-grained breast carcinoma subtyping performance of different foundation models on BRACS dataset.** Non-parametric bootstrapping with 1,000 bootstrap replicates is employed for statistical analysis. The 95% CI is included in parentheses. Best performing model for each metric is **bolded** and second-best performing model is underlined.

	Balanced ACC	Weighted F1	AUC
ResNet50	0.309 (0.266-0.357)	0.250 (0.181-0.320)	0.772 (0.719-0.818)
Phikon	0.363 (0.322-0.406)	0.293 (0.251-0.332)	0.818 (0.768-0.866)
Ctranspath	<b>0.530 (0.450-0.626)</b>	<b>0.520 (0.407-0.615)</b>	<u>0.857 (0.811-0.896)</u>
UNI	0.433 (0.356-0.511)	0.411 (0.325-0.490)	<u>0.855 (0.811-0.893)</u>
CONCH	0.424 (0.352-0.505)	0.367 (0.287-0.439)	0.841 (0.797-0.884)
PLIP	0.420 (0.342-0.511)	<u>0.414 (0.324-0.493)</u>	0.814 (0.763-0.864)
GPFM	<u>0.437 (0.360-0.514)</u>	<u>0.408 (0.326-0.493)</u>	<b>0.871 (0.829-0.904)</b>

**Table A10 Prostate cancer grade assessment performance of different foundation models on PANDA dataset.** Non-parametric bootstrapping with 1,000 bootstrap replicates is employed for statistical analysis. The 95% CI is included in parentheses. Best performing model for each metric is **bolded** and second-best performing model is underlined.

	Balanced ACC	Weighted F1	AUC
ResNet50	0.531 (0.510-0.552)	0.531 (0.508-0.553)	0.884 (0.875-0.892)
Phikon	<u>0.731 (0.709-0.750)</u>	<u>0.735 (0.715-0.755)</u>	0.943 (0.936-0.949)
Ctranspath	<u>0.649 (0.627-0.670)</u>	<u>0.651 (0.629-0.671)</u>	0.925 (0.918-0.932)
UNI	0.728 (0.707-0.749)	0.734 (0.712-0.753)	<u>0.944 (0.937-0.950)</u>
CONCH	0.656 (0.635-0.678)	0.657 (0.637-0.679)	<u>0.921 (0.914-0.929)</u>
PLIP	0.607 (0.583-0.628)	0.612 (0.591-0.635)	0.903 (0.894-0.911)
GPFM	<b>0.740 (0.720-0.760)</b>	<b>0.742 (0.722-0.762)</b>	<b>0.948 (0.941-0.954)</b>

**Table A11 Lung adenocarcinoma TP53 gene mutation prediction performance of different foundation models on TCGA-LUAD dataset.** 5-fold cross validation is employed for statistical analysis. The 95% CI is included in parentheses. Best performing model for each metric is **bolded** and second-best performing model is underlined.

	Balanced ACC	Weighted F1	AUC
ResNet50	0.675 (0.549-0.708)	0.609 (0.493-0.714)	0.742 (0.629-0.842)
Phikon	<u>0.783 (0.704-0.874)</u>	<u>0.782 (0.687-0.867)</u>	0.841 (0.754-0.918)
Ctranspath	0.711 (0.621-0.810)	0.710 (0.601-0.806)	<u>0.770 (0.660-0.867)</u>
UNI	0.639 (0.553-0.749)	0.638 (0.530-0.746)	0.766 (0.667-0.867)
CONCH	0.735 (0.618-0.820)	0.730 (0.629-0.818)	0.836 (0.734-0.911)
PLIP	0.759 (0.643-0.818)	0.739 (0.629-0.832)	0.821 (0.721-0.905)
GPFM	<b>0.795 (0.707-0.878)</b>	<b>0.794 (0.694-0.878)</b>	<b>0.855 (0.767-0.931)</b>

**Table A12 WSI-level gene mutation prediction performance of different foundation models on TCGA-GBMLGG IDH1 dataset.** Non-parametric bootstrapping with 1,000 bootstrap replicates is employed for statistical analysis. The 95% CI is included in parentheses. Best performing model for each metric is **bolded** and second-best performing model is underlined.

	Balanced ACC	Weighted F1	AUC
ResNet50	0.869 (0.805-0.926)	0.843 (0.778-0.905)	0.945 (0.905-0.977)
Phikon	<b>0.968 (0.928-0.996)</b>	<b>0.967 (0.932-0.993)</b>	0.990 (0.974-1.000)
Ctranspath	0.922 (0.862-0.973)	0.924 (0.874-0.970)	0.974 (0.949-0.994)
UNI	0.931 (0.872-0.978)	0.941 (0.890-0.976)	<u>0.996 (0.989-1.000)</u>
CONCH	0.944 (0.891-0.984)	<u>0.949 (0.909-0.984)</u>	<u>0.995 (0.987-0.999)</u>
PLIP	0.955 (0.911-0.988)	<u>0.943 (0.900-0.982)</u>	0.974 (0.931-1.000)
GPFM	<u>0.960 (0.915-996)</u>	<b>0.967 (0.933-0.993)</b>	<b>0.998 (0.995-1.000)</b>

**Table A13 Ovarian cancer subtyping performance of different foundation models on UBC-OCEAN dataset.** Non-parametric bootstrapping with 1,000 bootstrap replicates is employed for statistical analysis. The 95% CI is included in parentheses. Best performing model for each metric is **bolded** and second-best performing model is underlined.

	Balanced ACC	Weighted F1	AUC
ResNet50	0.685 (0.577-0.783)	0.675 (0.577-0.771)	0.919 (0.875-0.954)
Phikon	0.764 (0.681-0.852)	0.756 (0.669-0.834)	0.966 (0.944-0.985)
Ctranspath	0.763 (0.670-0.848)	0.760 (0.663-0.854)	0.960 (0.936-0.979)
UNI	<b>0.815 (0.731-0.900)</b>	<b>0.823 (0.713-0.910)</b>	0.969 (0.943-0.990)
CONCH	0.774 (0.694-0.862)	0.760 (0.666-0.864)	<u>0.957 (0.930-0.979)</u>
PLIP	0.775 (0.690-0.861)	0.755 (0.646-0.849)	0.946 (0.915-0.973)
GPFM	<u>0.796 (0.712-0.876)</u>	<u>0.799 (0.708-0.881)</u>	<b>0.972 (0.952-0.988)</b>

**Table A14 Brain tumor subtyping of different foundation models on EBRAINS dataset.** Non-parametric bootstrapping with 1,000 bootstrap replicates is employed for statistical analysis. The 95% CI is included in parentheses. Best performing model for each metric is **bolded** and second-best performing model is underlined.

	Balanced ACC	Weighted F1	AUC
ResNet50	0.693 (0.618-0.772)	0.675 (0.602-0.748)	0.959 (0.944-0.971)
Phikon	0.834 (0.772-0.892)	0.842 (0.782-0.897)	0.990 (0.986-995)
Ctranspath	0.818 (0.749-0.884)	0.830 (0.763-0.882)	0.985 (0.976-0.993)
UNI	0.897 (0.842-0.946)	0.898 (0.843-0.937)	<b>0.996 (0.992-0.999)</b>
CONCH	<b>0.909 (0.854-0.951)</b>	<b>0.910 (0.860-0.947)</b>	0.992 (0.988-0.997)
PLIP	0.758 (0.680-0.828)	0.757 (0.686-0.823)	0.977 (0.965-0.986)
GPFM	0.899 (0.843-0.945)	0.890 (0.829-0.936)	<b>0.996 (0.994-0.999)</b>

**Table A15 Average C-Index of Foundation Models Across 12 Survival Analysis Tasks.** The 95% CI is included in parentheses. The best-performing and second-best-performing models are highlighted in **bold** and underlined, respectively.

Models	C-Index
ResNet50	0.648 (0.543-0.752)
Phikon	0.720 (0.609-0.830)
Ctranspath	0.683 (0.607-0.758)
UNI	0.698 (0.594-0.802)
CONCH	0.667 (0.601-0.733)
PLIP	0.671 (0.602-0.741)
GPFM	<b>0.726 (0.634-0.818)</b>

**Table A16 Performance of Survival Analysis on BRCA, BLCA, and KIRC Datasets.** 5-fold cross validation is adopted for training and evaluation. The 95% CI is included in parentheses. The best and second-best performed models are **bolded** and underlined.

	BRCA	BLCA	KIRC
ResNet50	0.678 (0.660-0.696)	0.696 (0.653-0.739)	0.634 (0.565-0.703)
Phikon	<b>0.770 (0.750-0.790)</b>	0.692 (0.657-0.727)	<b>0.708 (0.673-0.743)</b>
Ctranspath	0.704 (0.682-0.726)	0.670 (0.641-0.699)	0.671 (0.608-0.734)
UNI	0.722 (0.710-0.734)	0.690 (0.645-0.735)	0.674 (0.627-0.721)
CONCH	0.677 (0.636-0.718)	0.644 (0.544-0.744)	0.659 (0.583-0.735)
PLIP	0.691 (0.666-0.716)	0.665 (0.594-0.736)	0.652 (0.572-0.732)
GPFM	0.757 (0.737-0.777)	<b>0.711 (0.682-0.740)</b>	0.697 (0.658-0.736)

**Table A17 Performance of Survival Analysis on KIRP, STAD, and CESC Datasets.** 5-fold cross validation is adopted for training and evaluation. The 95% CI is included in parentheses. The best and second-best performed models are **bolded** and underlined.

	KIRP	STAD	CEC
ResNet50	0.630 (0.562-0.697)	0.636 (0.572-0.701)	0.611 (0.517-0.705)
Phikon	0.680 (0.615-0.745)	<b>0.705 (0.660-0.750)</b>	0.747 (0.702-0.792)
Ctranspath	0.649 (0.567-0.731)	0.669 (0.610-0.728)	0.702 (0.569-0.835)
UNI	0.659 (0.563-0.755)	0.688 (0.641-0.735)	0.735 (0.649-0.821)
CONCH	0.623 (0.527-0.719)	0.636 (0.554-0.718)	0.677 (0.610-0.744)
PLIP	0.674 (0.631-0.717)	0.657 (0.584-0.730)	0.694 (0.588-0.800)
GPFM	<b>0.688 (0.639-0.737)</b>	0.694 (0.645-0.743)	<b>0.754 (0.646-0.862)</b>

**Table A18 Performance of Survival Analysis on LUAD, LUAD-CPTAC, and LUSC datasets.** 5-fold cross validation is adopted for training and evaluation. The 95% CI is included in parentheses. The best and second-best performed model are **bolded** and underlined. Note that LUAD-CPTAC evaluation is conducted using the LUAD trained model without further fine-tuning.

	LUAD	CPTAC-LUAD	LUSC
ResNet50	0.646 (0.601-0.691)	0.517 (0.431-0.603)	0.667 (0.623-0.711)
Phikon	0.738 (0.644-0.832)	0.577 (0.424-0.730)	<b>0.779 (0.729-0.829)</b>
Ctranspath	0.633 (0.584-0.682)	0.624 (0.565-0.683)	0.703 (0.590-0.817)
UNI	0.673 (0.614-0.732)	0.575 (0.495-0.655)	0.746 (0.665-0.828)
CONCH	0.641 (0.568-0.714)	<b>0.649 (0.608-0.690)</b>	0.661 (0.586-0.737)
PLIP	0.628 (0.536-0.720)	0.608 (0.508-0.708)	0.686 (0.647-0.725)
GPFM	<b>0.739 (0.690-0.788)</b>	0.626 (0.567-0.685)	0.777 (0.731-0.822)

**Table A19 Performance of Survival Analysis on COADREAD, GBMLGG, and SKCM datasets.** 5-fold cross validation is adopted for training and evaluation. The 95% CI is included in parentheses. The best and second-best performed model are **bolded** and underlined.

	COADREAD	GBMLGG	SKCM
ResNet50	0.632 (0.579-0.685)	0.724 (0.687-0.761)	0.699 (0.621-0.777)
Phikon	0.707 (0.646-0.768)	0.760 (0.740-0.780)	0.773 (0.732-0.814)
Ctranspath	0.680 (0.633-0.727)	0.745 (0.716-0.774)	0.743 (0.710-0.776)
UNI	0.691 (0.644-0.738)	0.778 (0.754-0.802)	0.747 (0.714-0.780)
CONCH	0.679 (0.616-0.742)	0.735 (0.708-0.762)	0.721 (0.627-0.815)
PLIP	0.653 (0.573-0.733)	0.738 (0.691-0.785)	0.709 (0.652-0.766)
GPFM	<b>0.708 (0.663-0.753)</b>	<b>0.785 (0.756-0.814)</b>	<b>0.777 (0.716-0.838)</b>

**Table A20 Average Tissue Classification Performance of Foundation Models across 12 Patch-level Tissue Datasets.** The 95% CI is included in parentheses. The best-performing and second-best-performing models are highlighted in **bold** and underlined, respectively.

	Balanced ACC	Weighted F1	AUC
ResNet50	0.757 (0.451-1.000)	0.749 (0.422-1.000)	0.927 (0.766-1.000)
Phikon	0.824 (0.501-1.000)	0.816 (0.477-1.000)	0.948 (0.809-1.000)
Ctranspath	0.799 (0.458-1.000)	0.794 (0.443-1.000)	0.947 (0.822-1.000)
UNI	0.845 (0.569-1.000)	0.840 (0.552-1.000)	0.953 (0.824-1.000)
CONCH	0.823 (0.578-1.000)	0.819 (0.566-1.000)	0.951 (0.837-1.000)
PLIP	0.762 (0.476-1.000)	0.753 (0.441-1.000)	0.928 (0.759-1.000)
GPFM	<b>0.853 (0.559-1.000)</b>	<b>0.848 (0.540-1.000)</b>	<b>0.955 (0.832-1.000)</b>

**Table A21 CRC tissue classification performance of different foundation models on CRC-100K dataset.** Non-parametric bootstrapping with 1,000 bootstrap replicates is employed for statistical analysis. The 95% CI is included in parentheses. Best performing model for each metric is **bolded** and second-best performing model is underlined.

	Balanced ACC	Weighted F1	AUC
ResNet50	0.792 (0.782-0.802)	0.775 (0.765-0.785)	0.983 (0.982-0.985)
Phikon	0.867 (0.859-0.875)	0.842 (0.833-0.850)	0.992 (0.991-0.993)
Ctranspath	0.853 (0.844-0.861)	0.833 (0.825-0.843)	<b>0.995 (0.994-0.996)</b>
UNI	0.879 (0.872-0.886)	0.849 (0.841-0.858)	0.991 (0.990-0.992)
CONCH	0.855 (0.847-0.863)	0.824 (0.815-0.833)	0.993 (0.992-0.994)
PLIP	0.804 (0.796-0.813)	0.764 (0.755-0.772)	0.990 (0.989-0.992)
GPFM	<b>0.896 (0.888-0.902)</b>	<b>0.872 (0.865-0.881)</b>	<b>0.995 (0.994-0.996)</b>

**Table A22 CCRCC tissue classification performance of different foundation models on CCRCC-TCGA-HEL dataset.** Non-parametric bootstrapping with 1,000 bootstrap replicates is employed for statistical analysis. The 95% CI is included in parentheses. Best performing model for each metric is **bolded** and second-best performing model is underlined.

	Balanced ACC	Weighted F1	AUC
ResNet50	0.930 (0.919-0.942)	0.934 (0.925-0.944)	0.993 (0.991-0.995)
Phikon	<u>0.949 (0.936-0.960)</u>	<u>0.955 (0.946-0.963)</u>	<b>0.997 (0.996-0.998)</b>
Ctranspath	0.936 (0.923-0.948)	0.938 (0.926-0.946)	0.994 (0.992-0.996)
UNI	0.946 (0.932-0.956)	0.950 (0.941-0.959)	0.996 (0.995-0.997)
CONCH	0.934 (0.920-0.946)	0.939 (0.929-0.949)	0.994 (0.992-0.995)
PLIP	0.920 (0.905-0.932)	0.919 (0.909-0.929)	0.992 (0.991-0.994)
GPFM	<b>0.953 (0.939-0.962)</b>	<b>0.956 (0.947-0.964)</b>	<b>0.997 (0.994-0.998)</b>

**Table A23 Breast cancer tissue classification performance of different foundation models on BACH dataset.** Non-parametric bootstrapping with 1,000 bootstrap replicates is employed for statistical analysis. The 95% CI is included in parentheses. Best performing model for each metric is **bolded** and second-best performing model is underlined.

	Balanced ACC	Weighted F1	AUC
ResNet50	0.865 (0.788-0.932)	0.856 (0.776-0.928)	0.977 (0.958-0.992)
Phikon	0.918 (0.845-0.971)	0.915 (0.842-0.965)	0.988 (0.975-0.998)
Ctranspath	0.927 (0.865-0.975)	0.919 (0.861-0.965)	<u>0.998 (0.993-1.000)</u>
UNI	<u>0.960 (0.915-1.000)</u>	<b>0.966 (0.911-1.000)</b>	<b>1.000 (0.999-1.000)</b>
CONCH	0.934 (0.879-0.981)	0.933 (0.885-0.986)	0.996 (0.988-1.000)
PLIP	0.799 (0.714-0.871)	0.791 (0.698-0.880)	0.959 (0.926-0.981)
GPFM	<b>0.963 (0.919-1.000)</b>	0.965 (0.915-1.000)	0.998 (0.994-1.000)

**Table A24 CRC polyp classification performance of different foundation models on UniToPatho dataset.** Non-parametric bootstrapping with 1,000 bootstrap replicates is employed for statistical analysis. The 95% CI is included in parentheses. Best performing model for each metric is **bolded** and second-best performing model is underlined.

	Balanced ACC	Weighted F1	AUC
ResNet50	0.397 (0.376-0.417)	0.384 (0.359-0.406)	0.830 (0.819-0.840)
Phikon	0.379 (0.358-0.398)	0.375 (0.356-0.395)	0.838 (0.828-0.847)
Ctranspath	0.310 (0.289-0.331)	0.302 (0.285-0.324)	0.836 (0.828-0.844)
UNI	0.462 (0.443-0.486)	0.455 (0.433-0.474)	0.840 (0.830-0.850)
CONCH	<b>0.522 (0.499-0.550)</b>	<b>0.527 (0.501-0.550)</b>	<b>0.865 (0.855-0.875)</b>
PLIP	0.437 (0.413-0.458)	0.418 (0.395-0.441)	0.823 (0.812-0.834)
GPFM	0.444 (0.420-0.463)	0.433 (0.412-0.456)	<u>0.844 (0.834-0.851)</u>

**Table A25 MSI screening performance of different foundation models on CRC-MSI dataset.** Non-parametric bootstrapping with 1,000 bootstrap replicates is employed for statistical analysis. The 95% CI is included in parentheses. Best performing model for each metric is **bolded** and second-best performing model is underlined.

	Balanced ACC	Weighted F1	AUC
ResNet50	0.654 (0.646-0.661)	0.587 (0.581-0.592)	0.706 (0.699-0.714)
Phikon	0.695 (0.689-0.703)	0.632 (0.626-0.638)	0.772 (0.766-0.779)
Ctranspath	0.728 (0.721-0.734)	0.647 (0.641-0.652)	0.802 (0.796-0.808)
UNI	0.719 (0.713-0.727)	<u>0.670 (0.664-0.676)</u>	0.797 (0.790-0.803)
CONCH	<b>0.734 (0.727-0.741)</b>	0.669 (0.663-0.675)	<u>0.810 (0.804-0.817)</u>
PLIP	0.639 (0.633-0.647)	0.589 (0.583-0.595)	0.691 (0.683-0.698)
GPFM	0.733 (0.726-0.740)	<b>0.672 (0.666-0.678)</b>	<b>0.812 (0.805-0.818)</b>

**Table A26 Pan-cancer tissue classification performance of different foundation models on PanCancer-TCGA dataset.** Non-parametric bootstrapping with 1,000 bootstrap replicates is employed for statistical analysis. The 95% CI is included in parentheses. Best performing model for each metric is **bolded** and second-best performing model is underlined. As shown in **Figure 5.j**, the distribution of bootstrapped AUC values is highly centered. As a result, the CI for the AUC is very narrow.

	Balanced ACC	Weighted F1	AUC
ResNet50	0.630 (0.625-0.636)	0.640 (0.636-0.646)	0.975 (0.974-0.976)
Phikon	0.924 (0.921-0.928)	0.926 (0.923-0.928)	<b>0.999 (0.999-0.999)</b>
Ctranspath	0.785 (0.780-0.790)	0.790 (0.786-0.795)	0.992 (0.991-0.992)
UNI	0.885 (0.882-0.889)	0.888 (0.885-0.892)	0.997 (0.997-0.997)
CONCH	0.784 (0.779-0.788)	0.789 (0.785-0.794)	0.991 (0.991-0.992)
PLIP	0.661 (0.656-0.667)	0.669 (0.664-0.675)	0.978 (0.978-0.979)
GPFM	<b>0.951 (0.949-0.954)</b>	<b>0.953 (0.950-0.955)</b>	<b>0.999 (0.999-0.999)</b>

**Table A27 TIL classification performance of different foundation models on PanCancer-TIL dataset.** Non-parametric bootstrapping with 1,000 bootstrap replicates is employed for statistical analysis. The 95% CI is included in parentheses. Best performing model for each metric is **bolded** and second-best performing model is underlined.

	Balanced ACC	Weighted F1	AUC
ResNet50	0.813 (0.809-0.818)	0.843 (0.839-0.847)	0.946 (0.944-0.948)
Phikon	0.893 (0.889-0.896)	0.901 (0.897-0.904)	0.975 (0.974-0.977)
Ctranspath	0.857 (0.852-0.860)	0.880 (0.876-0.883)	0.965 (0.963-0.967)
UNI	<b>0.897 (0.893-0.900)</b>	0.905 (0.902-0.908)	0.977 (0.976-0.979)
CONCH	0.866 (0.862-0.870)	0.889 (0.885-0.892)	0.971 (0.969-0.973)
PLIP	0.810 (0.805-0.815)	0.843 (0.838-0.847)	0.949 (0.947-0.951)
GPFM	0.894 (0.890-0.897)	<b>0.908 (0.904-0.911)</b>	<b>0.978 (0.977-0.979)</b>

**Table A28 ESCA subtyping performance of different foundation models on ESCA dataset.** Non-parametric bootstrapping with 1,000 bootstrap replicates is employed for statistical analysis. The 95% CI is included in parentheses. Best performing model for each metric is **bolded** and second-best performing model is underlined.

	Balanced ACC	Weighted F1	AUC
ResNet50	0.601 (0.591-0.611)	0.553 (0.544-0.563)	0.886 (0.882-0.889)
Phikon	0.668 (0.662-0.676)	0.642 (0.635-0.651)	0.894 (0.890-0.897)
Ctranspath	0.642 (0.632-0.651)	0.660 (0.649-0.669)	0.899 (0.896-0.902)
UNI	<b>0.754 (0.744-0.761)</b>	<b>0.758 (0.749-0.765)</b>	<b>0.903 (0.901-0.904)</b>
CONCH	0.690 (0.682-0.698)	0.700 (0.691-0.707)	0.902 (0.899-0.904)
PLIP	0.601 (0.593-0.608)	0.552 (0.544-0.559)	0.889 (0.886-0.892)
GPFM	0.732 (0.724-0.740)	0.734 (0.725-0.740)	0.902 (0.899-0.904)

**Table A29 Metastatic tissue classification performance of different foundation models on PCAM dataset.** Non-parametric bootstrapping with 1,000 bootstrap replicates is employed for statistical analysis. The 95% CI is included in parentheses. Best performing model for each metric is **bolded** and second-best performing model is underlined.

	Balanced ACC	Weighted F1	AUC
ResNet50	0.837 (0.834-0.841)	0.836 (0.832-0.840)	0.926 (0.923-0.928)
Phikon	0.898 (0.894-0.901)	0.897 (0.894-0.900)	0.969 (0.967-0.971)
Ctranspath	0.866 (0.862-0.869)	0.866 (0.862-0.869)	0.940 (0.937-0.942)
UNI	0.932 (0.929-0.934)	0.931 (0.929-0.934)	0.982 (0.981-0.983)
CONCH	0.903 (0.900-0.906)	0.903 (0.900-0.906)	0.965 (0.963-0.967)
PLIP	0.859 (0.856-0.863)	0.858 (0.854-0.862)	0.943 (0.941-0.945)
GPFM	<b>0.941 (0.939-0.944)</b>	<b>0.942 (0.939-0.944)</b>	<b>0.988 (0.987-0.989)</b>

**Table A30 Lung adenocarcinoma tissue classification performance of different foundation models on WSSS4LUAD dataset.** Non-parametric bootstrapping with 1,000 bootstrap replicates is employed for statistical analysis. The 95% CI is included in parentheses. Best performing model for each metric is **bolded** and second-best performing model is underlined.

	Balanced ACC	Weighted F1	AUC
ResNet50	0.911 (0.894-0.926)	0.910 (0.897-0.926)	0.989 (0.986-0.992)
Phikon	<u>0.956 (0.944-0.967)</u>	<u>0.957 (0.944-0.966)</u>	<u>0.997 (0.995-0.998)</u>
Ctranspath	0.947 (0.935-0.960)	0.949 (0.937-0.960)	<u>0.997 (0.996-0.998)</u>
UNI	0.951 (0.938-0.962)	0.951 (0.940-0.962)	<u>0.997 (0.996-0.998)</u>
CONCH	0.946 (0.933-0.960)	0.947 (0.935-0.959)	<u>0.995 (0.993-0.997)</u>
PLIP	0.927 (0.915-0.945)	0.934 (0.920-0.947)	0.994 (0.992-0.995)
GPFM	<b>0.961 (0.949-0.971)</b>	<b>0.959 (0.948-0.969)</b>	<b>0.998 (0.996-0.998)</b>

**Table A31 Breast cancer image classification performance of different foundation models on BreakHis dataset.** Non-parametric bootstrapping with 1,000 bootstrap replicates is employed for statistical analysis. The 95% CI is included in parentheses. Best performing model for each metric is **bolded** and second-best performing model is underlined.

	Balanced ACC	Weighted F1	AUC
ResNet50	0.937 (0.923-0.950)	0.938 (0.925-0.951)	0.986 (0.981-0.990)
Phikon	0.973 (0.964-0.981)	0.973 (0.965-0.982)	0.997 (0.996-0.998)
Ctranspath	0.962 (0.952-0.972)	0.961 (0.951-0.971)	0.995 (0.992-0.997)
UNI	<b>0.977 (0.967-0.984)</b>	<b>0.976 (0.968-0.984)</b>	<b>0.998 (0.997-0.999)</b>
CONCH	0.950 (0.935-0.961)	0.952 (0.941-0.963)	0.991 (0.986-0.994)
PLIP	0.943 (0.929-0.954)	0.940 (0.927-0.951)	0.989 (0.986-0.993)
GPFM	<u>0.974 (0.965-0.984)</u>	<b>0.976 (0.968-0.984)</b>	<b>0.998 (0.997-0.999)</b>

**Table A32 Colon tissue classification performance of different foundation models on Chaoyang dataset.** Non-parametric bootstrapping with 1,000 bootstrap replicates is employed for statistical analysis. The 95% CI is included in parentheses. Best performing model for each metric is **bolded** and second-best performing model is underlined.

	Balanced ACC	Weighted F1	AUC
ResNet50	0.725 (0.704-0.746)	0.735 (0.715-0.757)	0.930 (0.921-0.938)
Phikon	0.782 (0.762-0.804)	0.784 (0.763-0.803)	<u>0.952 (0.945-0.958)</u>
Ctranspath	0.772 (0.752-0.793)	0.779 (0.757-0.798)	<u>0.950 (0.943-0.957)</u>
UNI	0.790 (0.770-0.809)	0.789 (0.770-0.809)	<u>0.952 (0.945-0.958)</u>
CONCH	0.759 (0.738-0.778)	0.762 (0.743-0.783)	<u>0.942 (0.934-0.948)</u>
PLIP	0.747 (0.724-0.768)	0.755 (0.735-0.775)	0.941 (0.935-0.949)
GPFM	<b>0.797 (0.776-0.817)</b>	<b>0.803 (0.784-0.821)</b>	<b>0.956 (0.950-0.963)</b>

**Table A33 CRC Tissue Retrieval Performance on CRC-100K Dataset.** The table reports the Top-1, Top-3, and Top-5 ACC of different foundation models on the CRC-100K dataset for CRC tissue retrieval. Non-parametric bootstrapping with 1,000 bootstrap replicates was used for statistical analysis. The 95% CI is included in parentheses. The best performing model for each metric is **bolded** and the second-best performing model is underlined.

	ACC@1	ACC@3	ACC@5
ResNet50	0.777 (0.767-0.787)	0.940 (0.934-0.946)	0.958 (0.954-0.962)
Phikon	0.884 (0.876-0.892)	0.964 (0.960-0.968)	0.966 (0.962-0.970)
Ctranspath	0.825 (0.817-0.833)	0.910 (0.906-0.914)	0.915 (0.911-0.919)
UNI	<b>0.911 (0.903-0.919)</b>	<u>0.981 (0.977-0.985)</u>	<u>0.983 (0.981-0.985)</u>
CONCH	0.879 (0.871-0.887)	<u>0.974 (0.970-0.978)</u>	<u>0.976 (0.972-0.980)</u>
PLIP	0.798 (0.790-0.806)	0.909 (0.905-0.913)	0.915 (0.911-0.919)
GPFM	<u>0.906 (0.900-0.912)</u>	<b>0.993 (0.991-0.995)</b>	<b>0.995 (0.993-0.997)</b>



---

**Algorithm 1** The PyTorch-like pseudocode of the Expert Knowledge Distillation module.

---

**Require:**  $T_a, T_b,$  and  $T_c$  # off-the-shelf foundation models, we used phikon, uni, and conch in this study.

**Require:**  $S$  # student model

**Require:**  $v$  # global views

1:  $sc, sp = S(v)$  # [CLS] token and [patch] token encoded by student

2:  $ac, ap = T_a(v)$  # [CLS] token and [patch] token encoded by  $T_a$

3:  $bc, bp = T_b(v)$

4:  $cc, cp = T_c(v)$

5:  $d_{ac} = 1 - \cos(sc, ac)$

6:  $d_{bc} = 1 - \cos(sc, bc)$

7:  $d_{cc} = 1 - \cos(sc, cc)$

8:  $d_c = \alpha d_{ac} + \beta d_{bc} + \gamma d_{cc}$

9:  $d_{ap} = \eta * (1 - \cos(sp, ap)) + \theta * \text{SmoothL1}(sp, ap)$

10:  $d_{bp} = \eta * (1 - \cos(sp, bp)) + \theta * \text{SmoothL1}(sp, bp)$

11:  $d_{cp} = \eta * (1 - \cos(sp, cp)) + \theta * \text{SmoothL1}(sp, cp)$

12:  $d_p = \mu d_{ap} + \lambda d_{bp} + \phi d_{cp}$

13:  $d = d_c + d_p$

---

**Table A34 VQA performance of different foundation models on PathVQA dataset.** The open-ended, closed-ended and overall ACC are reported. The best performing model for each metric is **bolded** and the second-best performing model is underlined.

	Open ACC	Closed ACC	Overall ACC
ResNet50	28.17%(26.63%-29.70%)	86.52%(85.43%-87.61%)	57.35%
Phikon	30.78%(29.28%-32.29%)	87.20%(86.13%-88.27%)	58.99%
Ctranspath	31.11%(29.58%-32.65%)	87.51%(86.44%-88.58%)	60.32%
UNI	33.85%(32.28%-35.42%)	<b>88.69%(87.64%-89.74%)</b>	61.27%
CONCH	<b>37.08%(35.40%-38.77%)</b>	88.51%(87.49%-89.53%)	<b>62.80%</b>
PLIP	30.83%(29.29%-32.37%)	88.02%(86.94%-89.09%)	59.43%
GPFM	<u>34.26%(32.67%-35.84%)</u>	88.41%(87.32%-89.49%)	<u>61.33%</u>

**Table A35 Performance of foundation models in WSI report generation on TCGA WSI-Report dataset.** The best performing model for each metric is **bolded** and the second-best performing model is underlined.

	BLEU-1	BLEU-2	BLEU-3	BLEU-4	METEOR	ROUGE-L
ResNet50	0.252±0.003	0.113±0.003	0.062±0.003	0.039±0.003	0.093±0.001	0.179±0.002
Phikon	<b>0.404±0.005</b>	<b>0.290±0.005</b>	<b>0.225±0.005</b>	<b>0.181±0.005</b>	<b>0.178±0.003</b>	<b>0.336±0.005</b>
Ctranspath	0.254±0.004	0.131±0.003	0.079±0.003	0.052±0.003	0.097±0.002	0.189±0.003
UNI	0.363±0.005	0.250±0.005	0.189±0.005	0.151±0.004	0.156±0.003	0.298±0.005
CONCH	0.246±0.005	0.149±0.004	0.104±0.004	0.077±0.003	0.110±0.002	0.208±0.004
PLIP	0.265±0.004	0.135±0.003	0.080±0.003	0.053±0.003	0.102±0.002	0.188±0.003
GPFM	<u>0.384±0.005</u>	<u>0.271±0.005</u>	<u>0.210±0.005</u>	<u>0.169±0.005</u>	<u>0.168±0.003</u>	<u>0.320±0.005</u>

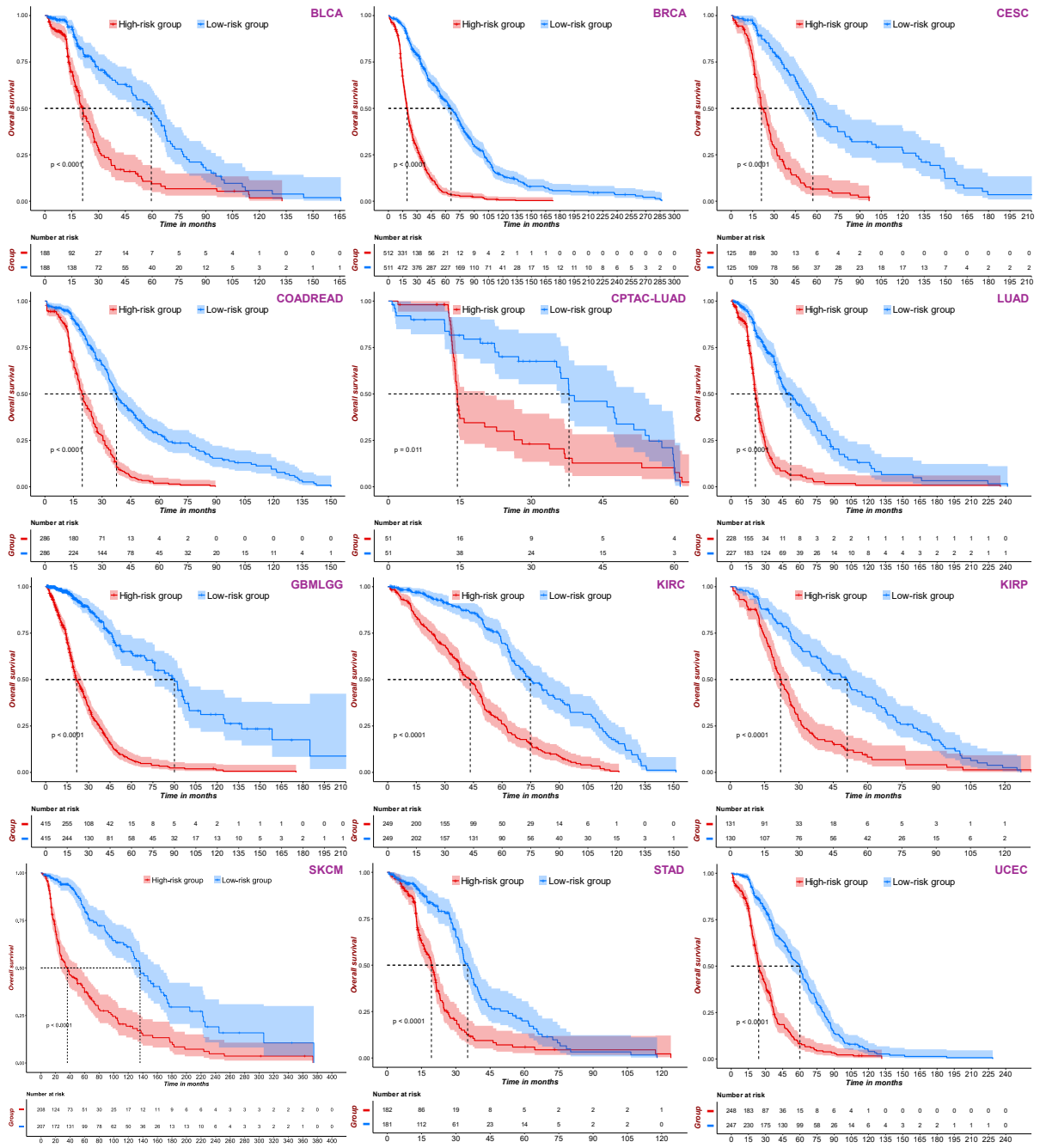


**Fig. A3 Survival Curve of the GPFM across 12 Tasks.** Note that the CPTAC-LUAD dataset is the external validation, which is evaluated by the model trained on LUAD (TCGA) dataset.

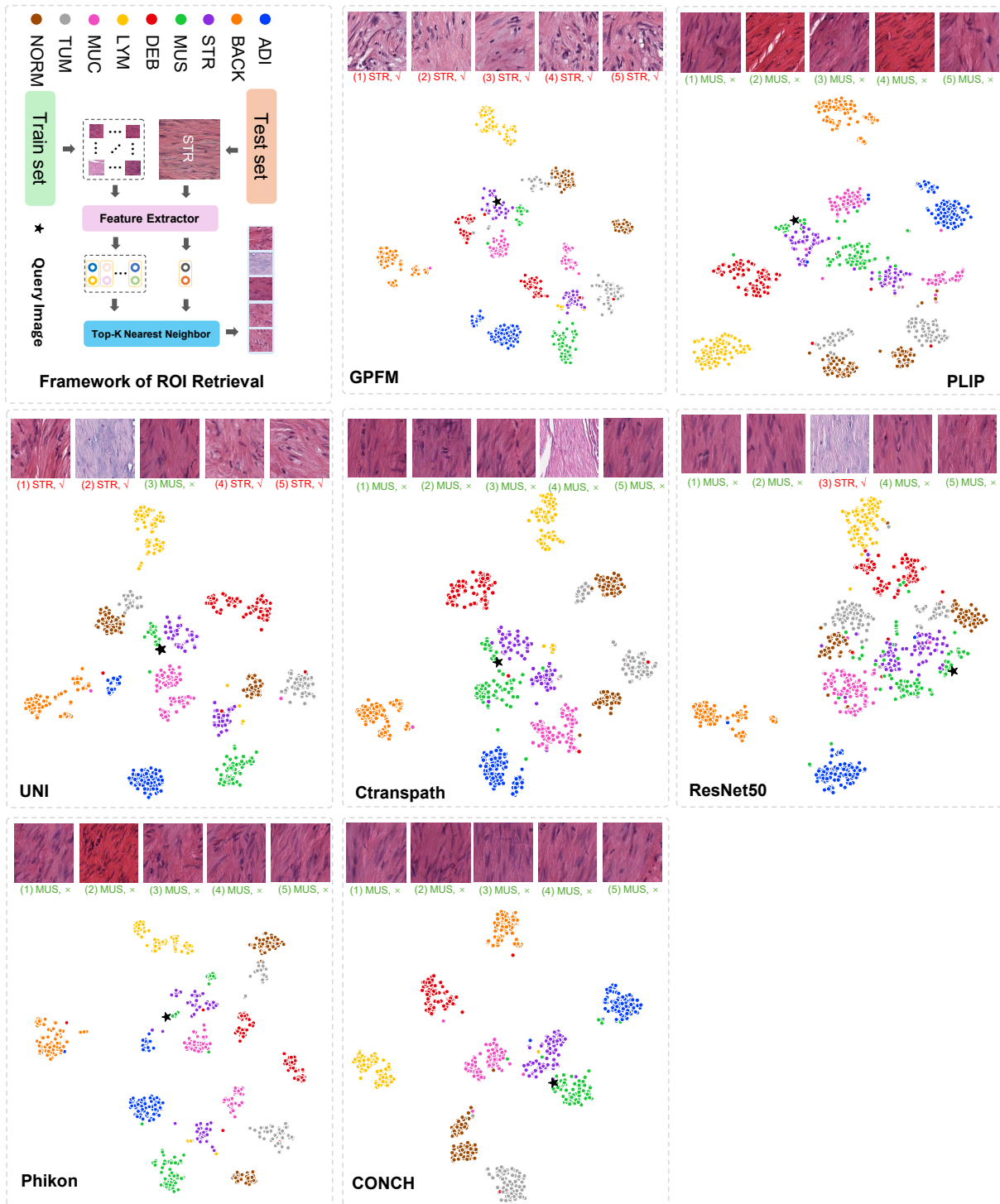


**Fig. A4 Overview of Pathology ROI Tissue Retrieval.** The central figure illustrates the framework for pathology tissue ROI retrieval. The surrounding figures visualize the distribution of features extracted by different models using t-SNE dimensionality reduction to 2D. For each class, 100 samples from the test set were used, and together with the query image, a total of 901 samples were subjected to the t-SNE analysis. The different classes are distinctly colored in the 2D t-SNE plot. The retrieved top-5 images for the query are also shown, demonstrating the GPFM's performance on this pathology tissue retrieval task.

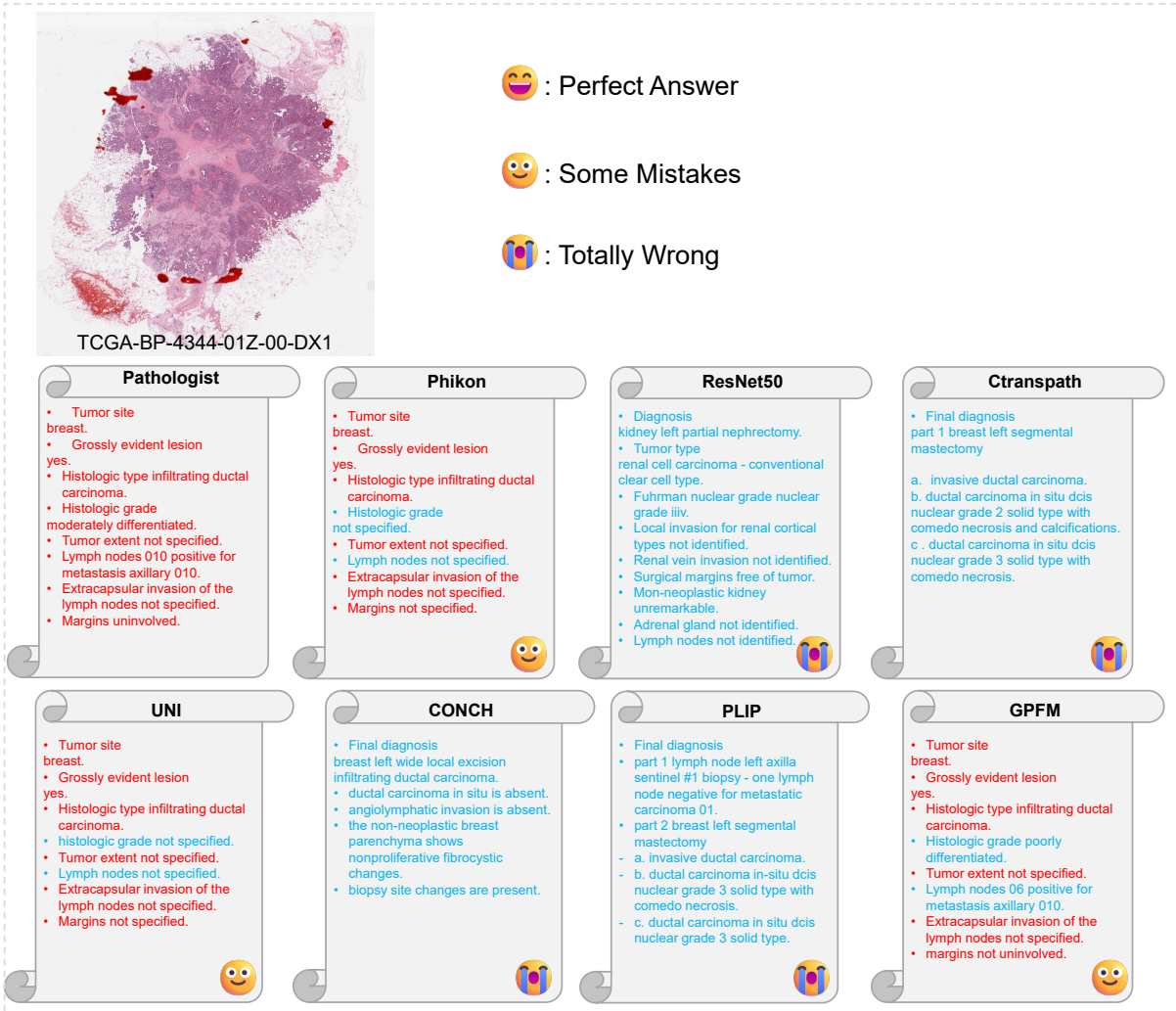
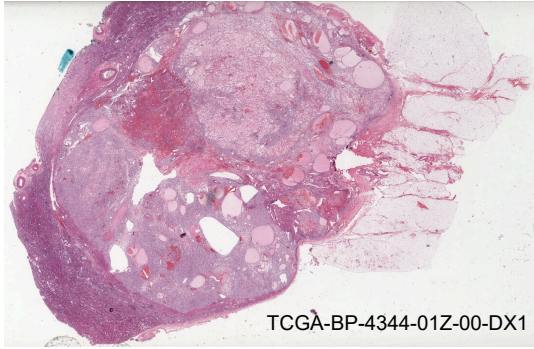


**Fig. A5 Generated Example Reports** The ground truth report is provided by pathologist. The text in red indicates correct predictions, the text in blue represents incorrect predictions.



😊 : Perfect Answer

😬 : Some Mistakes

😬 : Information not mentioned in the Pathologist's report

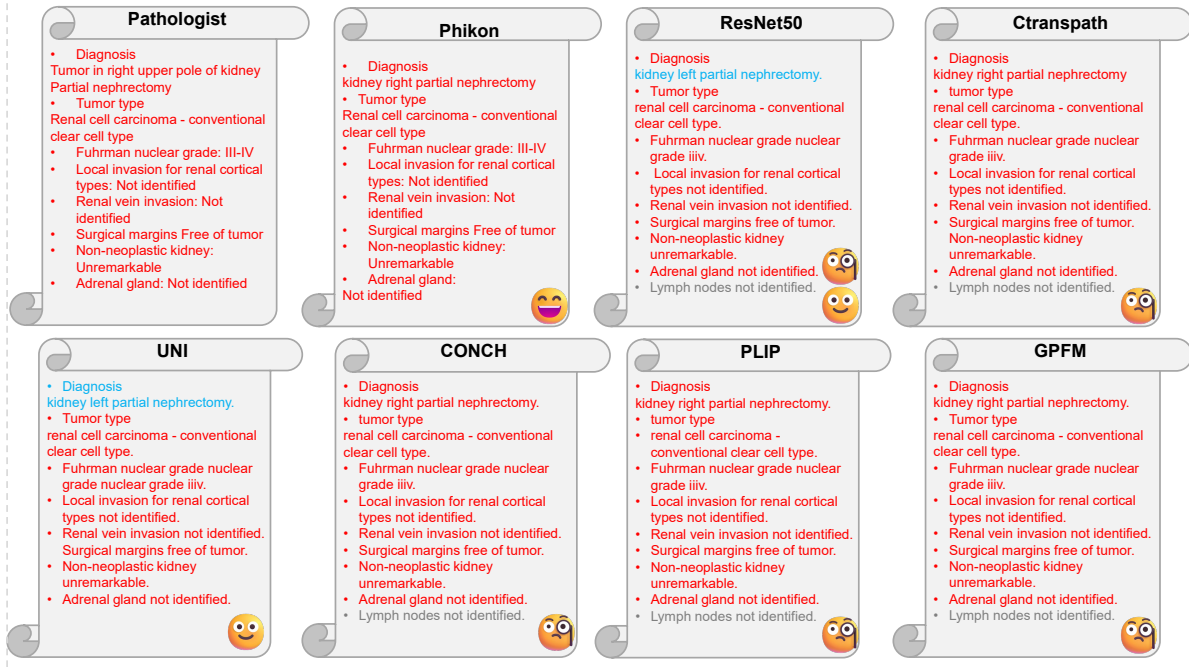


**Fig. A6 Generated Example Reports** The ground truth report is provided by pathologist. The text in red indicates correct predictions, the text in blue represents incorrect predictions, and the text in gray is the predicted text not mentioned in the pathologist's report.

**Table A36 Performance Comparison of DINOv2 and GPFM Pretraining Methods Across 12 Tasks.** DINOv2 represents the pretrained foundation model without using Expert Knowledge Distillation compared with GPFM. Overall, the Expert Knowledge Distillation module shows an average improvement across balanced ACC, weighted F1 score, and AUC.

	Method	Balanced ACC	Weighted F1	AUC
CRC-100K	DINOv2	0.845	0.822	0.990
	GPFM	0.896(+0.051)	0.872(+0.050)	0.995(+0.005)
WSSS4LUAD	DINOv2	0.957	0.956	0.998
	GPFM	0.961(+0.004)	0.959(+0.003)	0.998(+0.000)
PCAM	DINOv2	0.925	0.925	0.976
	GPFM	0.941(+0.016)	0.942(+0.017)	0.988(+0.012)
PanCancer-TCGA	DINOv2	0.939	0.940	0.999
	GPFM	0.951(+0.012)	0.953(+0.013)	0.999(+0.000)
PanCancer-TIL	DINOv2	0.857	0.864	0.963
	GPFM	0.894(+0.037)	0.908(+0.044)	0.978(+0.015)
chaoyang	DINOv2	0.802	0.808	0.957
	GPFM	0.797(-0.005)	0.803(-0.005)	0.956(-0.001)
CCRCC-TCGA-HEL	DINOv2	0.945	0.951	0.996
	GPFM	0.953(+0.008)	0.956(+0.005)	0.997(+0.001)
BreakHis	DINOv2	0.984	0.982	0.999
	GPFM	0.974(-0.008)	0.976(-0.006)	0.998(-0.001)
BACH	DINOv2	0.922	0.920	0.990
	GPFM	0.963(+0.041)	0.965(+0.045)	0.998(+0.008)
UniToPatho	DINOv2	0.457	0.431	0.844
	GPFM	0.444(-0.013)	0.433(+0.002)	0.844(+0.000)
CRC-MSI	DINOv2	0.679	0.655	0.777
	GPFM	0.733(+0.054)	0.672(+0.023)	0.812(+0.035)
ESCA	DINOv2	0.705	0.705	0.900
	GPFM	0.732(+0.027)	0.734(+0.029)	0.902(+0.002)
<b>Average</b>	DINOv2	0.835	0.830	0.949
	GPFM	0.853(+0.018)	0.848(+0.018)	0.955(+0.006)

**Table A37 The configuration of different foundation models used for comparison.** The details of the datasets used in GPFM are shown in **Extended Data** Table A40. UDK represents Unified Knowledge Distillation

Model	Data Source	WSIs	Patches	Model arch.	Model size	Pretraining
ResNet50 [76]	ImageNet	NA	NA	ResNet50	25M	Supervised
Ctranspath [37]	TCGA+PAIP	32K	4.2M	SwinTrans.	28M	MoCoV3 [112]
Phikon [32]	TCGA	6K	43M	ViT-B	86M	iBOT [72]
UNI [33]	Private+GTEx	100K	100M	ViT-L	307M	DINOv2 [56]
PLIP [36]	OpenPath	NA	200K	ViT-B	86M	CLIP[113]
CONCH [35]	PMC-Path +EDU	NA	1.2M	ViT-B	86M	CoCa [114]
GPFM (our)	33 Pubic datasets	72K	190M	ViT-L	307M	UDK

**Table A38** The hyper parameters for pretraining the proposed foundation model. The pretraining is conducted on 2 DGX nodes with 16×80GB H800 GPUs.

	Hyperparameters	Value
model	Layer number	24
	Feature dim	1024
	Patch size	14
	Heads number	16
	FFN layer	mlp
	Drop path ratio	0.4
	Layer scale	1e-5
optimization	Teacher momentum	0.992
	Total batch size	1,536
	Base learning rate	4e-4
	Minimum learning rate	1e-6
	Global crops scale	0.32, 1.0
	Global crops size	224
	Local crops scale	0.05, 0.32
	Local crops number	8
	Local crops size	98
	Gradient clip	3.0
	Warmup iterations	50,000
	Total iterations	500,000
loss weights	DINO	1.0
	iBOT	1.0
	CLS UNI	1.0
	Patch UNI	0.25
	CLS Phikon	0.5
	Patch Phikon	0.125
	CLS CONCH	1.0
Patch CONCH	0.0	

**Table A39** The architecture of ABMIL model and training details for WSI classification and survival analysis.

Architecture	Two-layer ABMIL
Embedding Dimension	512
Hidden Dimensions	128
Dropout Rates	0.25
Optimizer	AdamW
Learning Rate	2e-4
WSI Classification Loss	Cross-entropy
Survival Analysis Loss	NLL loss
Maximum Epochs	100
Early Stopping	Yes

**Table A40** The number of slides and processed patches of 33 datasets used for pretraining foundation models. "-" represents the dataset only providing ROIs.

Dataset Name	Number of Slides	Total Patches
TCGA	26,285	120,496,200
GTEXPportal	24,467	31,892,017
CPTAC	7,164	11,768,225
CAMELYON17	841	4,612,382
HunCRC	200	3,369,925
BRACS	381	2,992,229
DiagSet	825	2,500,385
AGGC2022	286	2,130,584
CAMELYON16	288	1,706,890
DLBCL	203	1,524,388
PAIP2020	118	1,362,725
O.B.R	283	1,159,516
PAIP2021	220	1,048,840
NADT-Prostate	1,303	919,847
PANDA	7,114	905,206
PAIP2019	96	505,356
TIGER2021	174	312,835
BCNB	1,036	263,734
Post-NAT-BRCA	96	241,547
SLN-Breast	129	139,166
BACH	30	108,256
ACROBAT2023	153	76,128
MIDOG2022	395	43,342
ARCH	-	25,919
MIDOG2021	193	24,025
LC25000	-	19,678
SICAPv2	-	18,783
AML-C-LMU	-	18,365
CAMEL	-	16,744
OCELOT	-	3,201
SPIE2019	-	2,579
Janowczyk	-	2,260
Oste. Tumor	-	1,391
Total	72,280	190,212,668



**Table A41** The primary site of tissues used for pretraining foundation models and downstream tasks evaluation.

Primary Site	The Number of Slides
prostate	19,253
breast	6,871
female reproductive system	6,500
lung	6,294
brain	5,367
kidney	4,654
colon	4,241
skin	3,168
esophagus	3,100
artery	2,499
stomach	2,153
thyroid	2,064
pancreas	1,965
adipose	1,793
liver	1,681
lymph	1,660
heart	1,620
adrenal gland	1,359
bladder	1,056
testis	1,007
muscle	1,001
nerve	975
tongue, tonsil and mouth	902
spleen	874
unknown	839
small intestine	798
soft tissue	524
head and neck	384
peritoneum	310
larynx	303
thymus	252
minor salivary gland	247
rectosigmoid	240
eye	150
Total	86,104

**Table A42 The public codes used in this study.** Please note that the pretrained weights of UNI and CONCH need to be permitted before downloading.

code	source
UNI	<a href="https://huggingface.co/MahmoodLab/UNI">https://huggingface.co/MahmoodLab/UNI</a>
Phikon	<a href="https://huggingface.co/owkin/phikon">https://huggingface.co/owkin/phikon</a>
CONCH	<a href="https://huggingface.co/MahmoodLab/CONCH">https://huggingface.co/MahmoodLab/CONCH</a>
CLAM	<a href="https://github.com/mahmoodlab/CLAM">https://github.com/mahmoodlab/CLAM</a>
CTranspath	<a href="https://github.com/Xiyue-Wang/TransPath">https://github.com/Xiyue-Wang/TransPath</a>
PLIP	<a href="https://github.com/PathologyFoundation/plip">https://github.com/PathologyFoundation/plip</a>
MUMC	<a href="https://github.com/pengfeiliHEU/MUMC">https://github.com/pengfeiliHEU/MUMC</a>
HistGen	<a href="https://github.com/dddavid4real/HistGen">https://github.com/dddavid4real/HistGen</a>
Torchmetrics	<a href="https://github.com/Lightning-AI/torchmetrics">https://github.com/Lightning-AI/torchmetrics</a>
Scikit-learn	<a href="https://scikit-learn.org/stable/">https://scikit-learn.org/stable/</a>

**Table A43 The dataset used in this study.** Please note that some datasets may need permission before downloading.

Dataset	Link
1. TCGA [45]	<a href="https://portal.gdc.cancer.gov/">https://portal.gdc.cancer.gov/</a>
2. CPTAC [79]	<a href="https://proteomic.datacommons.cancer.gov/pdc/">https://proteomic.datacommons.cancer.gov/pdc/</a>
3. PANDA [48]	<a href="https://www.kaggle.com/c/prostate-cancer-grade-assessment/data">https://www.kaggle.com/c/prostate-cancer-grade-assessment/data</a>
4. NADT-Prostate [115]	<a href="https://www.cancerimagingarchive.net/collection/nadt-prostate/">https://www.cancerimagingarchive.net/collection/nadt-prostate/</a>
5. BCNB [116]	<a href="https://bcnb.grand-challenge.org/">https://bcnb.grand-challenge.org/</a>
6. CAMELYON16 [46]	<a href="https://camelyon16.grand-challenge.org/Data/">https://camelyon16.grand-challenge.org/Data/</a>
7. CAMELYON17 [47]	<a href="https://camelyon17.grand-challenge.org/Data/">https://camelyon17.grand-challenge.org/Data/</a>
8. BRACS [44]	<a href="https://www.bracs.icar.cnr.it/download/">https://www.bracs.icar.cnr.it/download/</a>
9. TIGER2021 [117]	<a href="https://tiger.grand-challenge.org/">https://tiger.grand-challenge.org/</a>
10. MIDOG2022 [118]	<a href="https://midog.deepmicroscopy.org/download-dataset/">https://midog.deepmicroscopy.org/download-dataset/</a>
11. AGGC2022 [119]	<a href="https://aggc22.grand-challenge.org/">https://aggc22.grand-challenge.org/</a>
12. O.B.R. [120, 121]	<a href="https://www.cancerimagingarchive.net/collection/ovarian-bevacizumab-response/">https://www.cancerimagingarchive.net/collection/ovarian-bevacizumab-response/</a>
13. ACROBAT2023 [122]	<a href="https://acrobot.grand-challenge.org/">https://acrobot.grand-challenge.org/</a>
14. AML-C-LMU [123]	<a href="https://www.cancerimagingarchive.net/collection/aml-cytomorphology_lmu/">https://www.cancerimagingarchive.net/collection/aml-cytomorphology_lmu/</a>
15. ARCH [124]	<a href="https://warwick.ac.uk/fac/cross_fac/tia/data/arch">https://warwick.ac.uk/fac/cross_fac/tia/data/arch</a>
16. BACH [89]	<a href="https://zenodo.org/records/3632035">https://zenodo.org/records/3632035</a>
17. CAMEL [125]	<a href="https://drive.google.com/open?id=1brr8CnU6ddzAYT157wkdXjbSzoIDF9y">https://drive.google.com/open?id=1brr8CnU6ddzAYT157wkdXjbSzoIDF9y</a>
18. DiagSet [126]	<a href="https://ai-econsilio.diag.pl/">https://ai-econsilio.diag.pl/</a>
19. DLBCL [127]	<a href="https://github.com/stanfordmlgroup/DLBCL-Morph">https://github.com/stanfordmlgroup/DLBCL-Morph</a>
20. GTE <sub>x</sub> [128]	<a href="https://gtexportal.org/home/histologyPage">https://gtexportal.org/home/histologyPage</a>
21. HunCRC [129]	<a href="https://www.cancerimagingarchive.net/collection/hungarian-colorectal-screening/">https://www.cancerimagingarchive.net/collection/hungarian-colorectal-screening/</a>
22. Janowczyk [130]	<a href="https://andrewjanowczyk.com/use-case-1-nuclei-segmentation/">https://andrewjanowczyk.com/use-case-1-nuclei-segmentation/</a>
23. LC25000 [131]	<a href="https://academicjournals.com/details/7a638ed187a6180fd6e464b3666a6ea0499af4af">https://academicjournals.com/details/7a638ed187a6180fd6e464b3666a6ea0499af4af</a>
24. MIDOG2021 [118]	<a href="https://imig.science/midog2021/download-dataset/">https://imig.science/midog2021/download-dataset/</a>
25. OCELOT [132]	<a href="https://zenodo.org/record/7844149">https://zenodo.org/record/7844149</a>
26. Oste. Tumor [133]	<a href="https://www.cancerimagingarchive.net/collection/osteosarcoma-tumor-assessment/">https://www.cancerimagingarchive.net/collection/osteosarcoma-tumor-assessment/</a>
27. PAIP2019 [134]	<a href="https://paip2019.grand-challenge.org/">https://paip2019.grand-challenge.org/</a>
28. PAIP2020 [135]	<a href="https://paip2020.grand-challenge.org/">https://paip2020.grand-challenge.org/</a>
29. PAIP2021	<a href="https://paip2021.grand-challenge.org/">https://paip2021.grand-challenge.org/</a>
30. Post-NAT-BRCA [136]	<a href="https://www.cancerimagingarchive.net/collection/post-nat-brca/">https://www.cancerimagingarchive.net/collection/post-nat-brca/</a>
31. SICAPv2 [137]	<a href="https://data.mendeley.com/datasets/9xxm58dvs3/1">https://data.mendeley.com/datasets/9xxm58dvs3/1</a>
32. SLN-Breast [138]	<a href="https://www.cancerimagingarchive.net/collection/sln-breast/">https://www.cancerimagingarchive.net/collection/sln-breast/</a>
33. SPIE2019 [139]	<a href="https://breastpathq.grand-challenge.org/">https://breastpathq.grand-challenge.org/</a>
34. TUPAC [140]	<a href="https://tupac.grand-challenge.org/">https://tupac.grand-challenge.org/</a>
35. UBC-OCEAN [49]	<a href="https://www.kaggle.com/competitions/UBC-OCEAN/data">https://www.kaggle.com/competitions/UBC-OCEAN/data</a>
36. RCC-DHMC [141]	<a href="https://bmirids.github.io/KidneyCancer/">https://bmirids.github.io/KidneyCancer/</a>
37. CRC-100K [60]	<a href="https://zenodo.org/records/1214456">https://zenodo.org/records/1214456</a>
38. CRC-MSI [91]	<a href="https://zenodo.org/records/3832231">https://zenodo.org/records/3832231</a>
39. CCRCC-TCGA-HEL [88]	<a href="https://zenodo.org/records/7898308">https://zenodo.org/records/7898308</a>
40. PanCancer-TCGA [92]	<a href="https://zenodo.org/records/5889558">https://zenodo.org/records/5889558</a>
41. PanCancer-TIL [93]	<a href="https://zenodo.org/records/6604094">https://zenodo.org/records/6604094</a>
42. ESCA [95]	<a href="https://zenodo.org/records/7548828">https://zenodo.org/records/7548828</a>
43. PCAM [96]	<a href="https://github.com/basveeling/pcam">https://github.com/basveeling/pcam</a>
44. BreakHis [99]	<a href="https://www.kaggle.com/datasets/ambarish/breakhis">https://www.kaggle.com/datasets/ambarish/breakhis</a>
45. Chaoyang [100]	<a href="https://github.com/bupt-ai-cz/HSA-NRL">https://github.com/bupt-ai-cz/HSA-NRL</a>
46. PathVQA [62]	<a href="https://github.com/UCSD-AI4H/PathVQA">https://github.com/UCSD-AI4H/PathVQA</a>
47. HistGen [63]	<a href="https://github.com/dddavid4real/HistGen">https://github.com/dddavid4real/HistGen</a>